Suspended Sand Transport in Surf Zones on Equilibrium Beaches

by

Haoyu Zhao and Nobuhisa Kobayashi

RESEARCH REPORT NO. CACR-05-01
January, 2005

Center for Applied Coastal Research
Ocean Engineering Laboratory
University of Delaware
Newark, DE 19716

TABLE OF CONTENTS

LIST OF FIGURES

LIST OF TABLES

ABSTRACT

A test with the spectral peak period of 2.6 s was conducted in a wave flume to measure velocities and sediment concentrations under irregular waves on an equilibrium fine sand beach. Combined with the two previous tests with the spectral peak periods of 4.8 and 1.6 s performed in the same wave flume, velocities and concentrations were measured in the vicinity of bottom at 94 elevations along 17 cross-shore lines. The relations among the three turbulent velocity variances are found to be similar to those for the boundary layer flow. The vertical variation of the mean concentration $\overline{C}$ can be fitted by the exponential and power-form distributions equally well. The equation for the concentration standard deviation σ_C is derived to show that the ratio $\sigma_C/\overline{C}$ varies little vertically. The correlation coefficient γ_{UC} between the horizontal velocity and concentration is of the order of 0.1 and decreases upward linearly. The onshore and offshore transport rates of suspended sediment are estimated and expressed in terms of the suspended sediment volume $\overline{V}$ per unit area. A time-averaged numerical model is developed to predict $\overline{V}$ as well as the mean and standard deviation of the free surface elevation and horizontal velocity. The bottom slope effect on the wave energy dissipation rate D_B due to wave breaking is included in the model. The computation can be made well above the still water shoreline with no numerical difficulty. Reflected waves from the shoreline are estimated from the wave energy flux remaining at the shoreline. The numerical model is in agreement with the statistical data except that the undertow current is difficult to predict accurately. The measured turbulent velocities are found to be more related to the turbulent velocity estimated from the energy dissipation rate D_f due to bottom

friction. The suspended sediment volume $\overline{V}$ expressed in terms of D_B and D_f can be predicted only within a factor of about 2. The roller effect represented by the roller volume flux is added to the numerical model. The computed results with and without the roller effect are compared for the three tests. The roller effect does not necessarily improve the agreement for the three tests.

Chapter 1

INTRODUCTION

Cross-shore sediment transport on beaches has been investigated extensively. For the beach at Duck, North Carolina alone, a large number of studies have been performed. Trowbridge and Young [1989] used a sheet flow model based on the time-averaged onshore bottom shear stress to explain the onshore movement of a bar on the beach observed during low-energy wave conditions. Thornton et al. [1996] and Gallagher et al. [1998] used the energetics-based total load model of Bailard [1981] to explain the offshore movement of the bar observed during storms. The energetics model could not predict the slow onshore migration observed during low-energy wave conditions. Hoefel and Elgar [2003] included the skewed accelerations in the energetics-based sediment transport model to successfully simulate both onshore and offshore bar migration. On the other hand, Henderson et al. [2004] developed a wave-resolving, eddy-diffusion model of water and suspended sediment motion in the bottom boundary layer. This model also predicted the onshore and offshore bar migration events successfully. However, no model could predict a third event for the offshore bar migration. In these studies, it was not possible to assess the accuracy of the sediment transport models because no measurement was made of suspended sediment and bed load. This is normally the case with other numerical studies for beach profile changes [e.g., Roelvink and Stive 1989; Karambas and Koutitas, 2002].

Suspended sediment transport under breaking waves is examined here in detail in order to improve our capability in predicting the cross-shore sediment

transport on beaches. A test with the spectral peak period of 2.6 s was conducted in a wave flume on an equilibrium beach consisting of fine sand under irregular breaking waves. Combined with the other two tests performed by Giovannozzi and Kobayashi [2002] and Tega and Kobayashi, et. al. [2004] in the same wave flume with the spectral peak periods of 4.8 and 1.6 s, velocities and sand concentrations at 94 elevations along 17 vertical lines were measured. The bed load transport rates were estimated using the condition of no net sediment transport on the equilibrium beach. The velocity measurements are used to obtain the three turbulent velocity variances in the vicinity of the bottom in the surf zone. The synchronous measurements of the horizontal velocity and concentration allowed us to estimate the onshore-suspended sediment transport rate due to their positive correlation. A time-averaged numerical model is developed and compared with the three tests. This model is an extension of existing models with and without the effect of a roller. The bottom slope effect on the rate of wave energy dissipation due to wave breaking is included in the model. This extension allows one to continue the landward-marching computation well above the still water shoreline with no numerical difficulty and estimate the degree of wave reflection from the shoreline.

Chapter 2 describes the equilibrium profile experiment including the laboratory setup, experimental procedures, instrument calibrations, and measurements of the free surface elevation, velocities, sand concentration and beach profile. In chapter 3, the analyses of the velocitiy and concentration data are presented for the three tests and the estimated onshore and offshore suspended sediment transport rates are given. Chapter 4 presents the extended time-averaged numerical model with and without the roller volume flux. Furthermore, the numerical model is compared with the data and the importance and uncertainty of bottom friction are discussed in relation to the turbulent velocities and sand suspension. Chapter 5 gives the summary of the findings in this study. The summary of this study is presented by Kobayashi,

Zhao and Tega [2005].

Chapter 2

EXPERIMENTAL PROCEDURES

The experimental procedures for test 2.6 conducted here are the same as tests 4.8 and 1.6 conducted by Giovannozzi and Kobayashi [2003] and Tega et al. [2004] where the value of the spectral peak period T_p is used to identify each of the three tests. In Chapter 3 and 4, the three tests are discussed together so as to allow the comparisons of the three tests.

2.1 Experimental Setup

The experiments were conducted in a wave tank that was 30 m long, 2.4 m wide and 1.5 m high with a dividing wall constructed along the centerline of the tank to reduce the volume of fine sand required for the experiment as presented by Kobayashi and Lawrence [2004] for their solitary wave experiment. A rear wall was added to support the upper berm area of the beach. The water depth in the flume was 0.9 m. Repeatable irregular waves, based on the TMA spectrum with the spectral peak period, $T_p = 2.6$ s, were generated with a piston-type wave paddle. For tests 4.8 and 1.6, $T_p = 4.8$ and 1.6 s. The wave heights generated in these tests were the approximately largest waves that could be generated with no wave breaking at the wave paddle. A rock slope was located at the other end of the tank to absorb waves.

On the basis of the equilibrium profiles for tests 4.8 and 1.6, an equilibrium profile was estimated and constructed manually as an initial profile. The initial profile was then exposed to the specified incident irregular waves generated in a

burst of 400 s. The sand beach became quasi-equilibrium with the bottom change less than 1 cm/hr after the exposure to the wave action for more than 16 hours. The use of the guessed equilibrium profile reduced the time required for the establishment of the equilibrium profile. The burst durations for test 4.8 and 1.6 were 900 and 300 s, respectively.

Beach profiles were measured along three cross-shore transects using a vernier pointer in the swash zone and two ultrasonic depth gauges in deeper water. The measured profiles were essentially uniform alongshore and the averaged profile is used in the following. The measured beach profiles are depicted in Figure 2.1. The slopes of

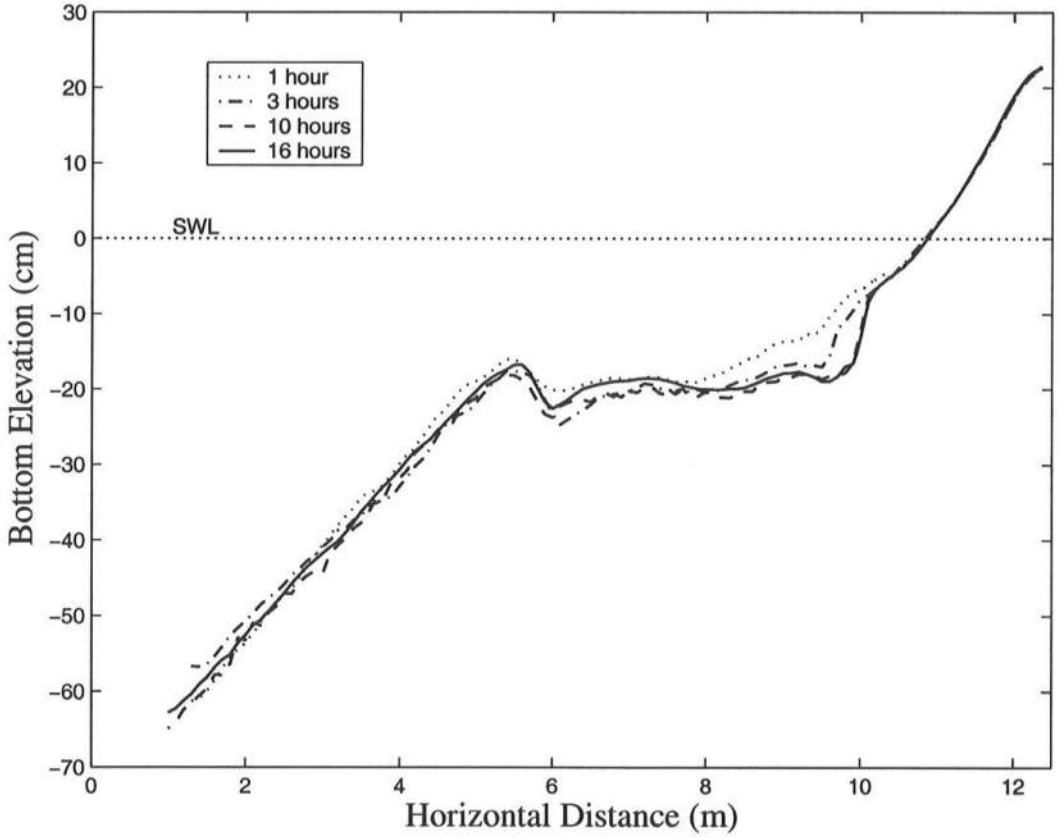

Figure 2.1: Measured beach profiles for test 2.6

the foreshore, terrace and offshore zone of the equilibrium profile are approximately 1:6, 1:100 and 1:9, respectively. The equilibrium profile has a sand bar in the outer

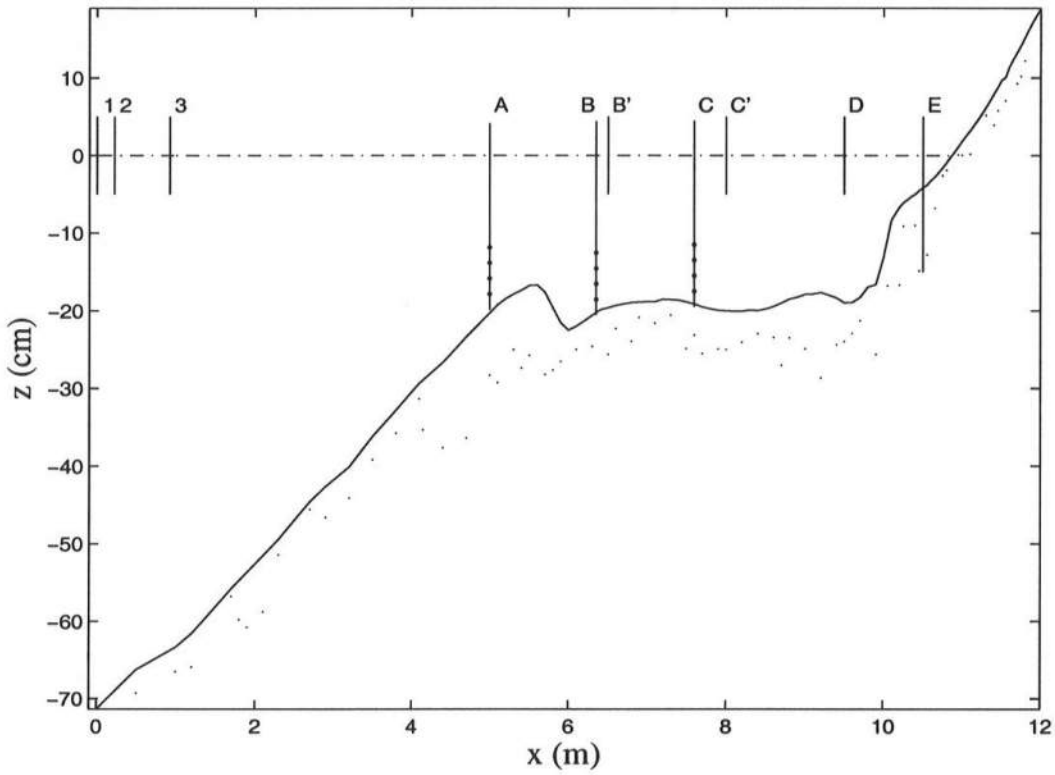

Figure 2.2: Cross-shore and vertical gauge locations above equilibrium beach for test 2.6 with the dots indicating the locations of velocities and sediment concentrations being measured

surf zone. Two-dimensional ripples in the surf zone and three-dimensional ripples seaward of the sand bar were present for test 2.6. After the equilibrium profile was established, 12 runs were conducted employing the same irregular waves lasting 400 s where the velocities and concentrations were measured at the elevation of 2, 4, 6 and 8 cm above the local bottom at line A, B and C, respectively, as shown in Figure 2.2. Two Acoustic Doppler Velocimeters (ADV) were used to measure the temporal variations of the fluid velocities at two alongshore locations simultaneously. A Fiber Optic Sediment monitor (FOBS-7) with two sensors was used to measure the suspended sediment concentrations at two alongshore locations simultaneously.

Eight capacitance wave gauges were placed as shown in Figure 2.2 to measure the temporal variations of the free surface elevations as explained in section 2.3. The offshore three wave gauges were used to ensure the repeatability of the incident and reflected waves. The sampling rate was 20 Hz for the measurements of the free surface, fluid velocities and suspended sediment concentrations.

2.2 Sand Characteristics

The sand beach was constructed of approximately 8 tons of fine quarry sand. The sand size distribution was obtained using a sieve test procedure consisting of nine different sieve sizes by Lawrence and Kobayashi [2003]. A sample of sand with a mass of 293.9 g was agitated for 20 minutes. The results are shown graphically in Figure 2.3 and are summarized in Table 2.1. The mean diameter, d_{50} was found to be 0.18 mm. Other characteristics of this sand such as the sand density, specific gravity and fall velocity were measured before the tests. The sand density was found from the ratio of the sand mass to the sand volume. The sand volume was determined by placing a known mass of sand in a graduated cylinder with a known volume of water. The amount of water displaced gave the volume of the sand. The specific gravity of the sand is defined as $s = \rho_s/\rho_w$, where ρ_w = density of fresh water and ρ_s = density of sand. The moisture content of the sand was found to be insignificant as the average value was 0.44%. The porosity n_p was then found using the measured dry sand mass and volume together with the specific gravity. The average specific gravity was determined to be $s = 2.6$ and the porosity was found to be $n_p = 0.4$.

The sediment falling velocity was determined experimentally by dropping several sand grains from each size group into a clear glass cylinder filled with water. The motion of the grains was visually timed for a distance of one meter. For each size group, ten falls were recorded and then averaged to obtain a mean fall velocity for each group. This mean velocity was then multiplied by a weighting factor

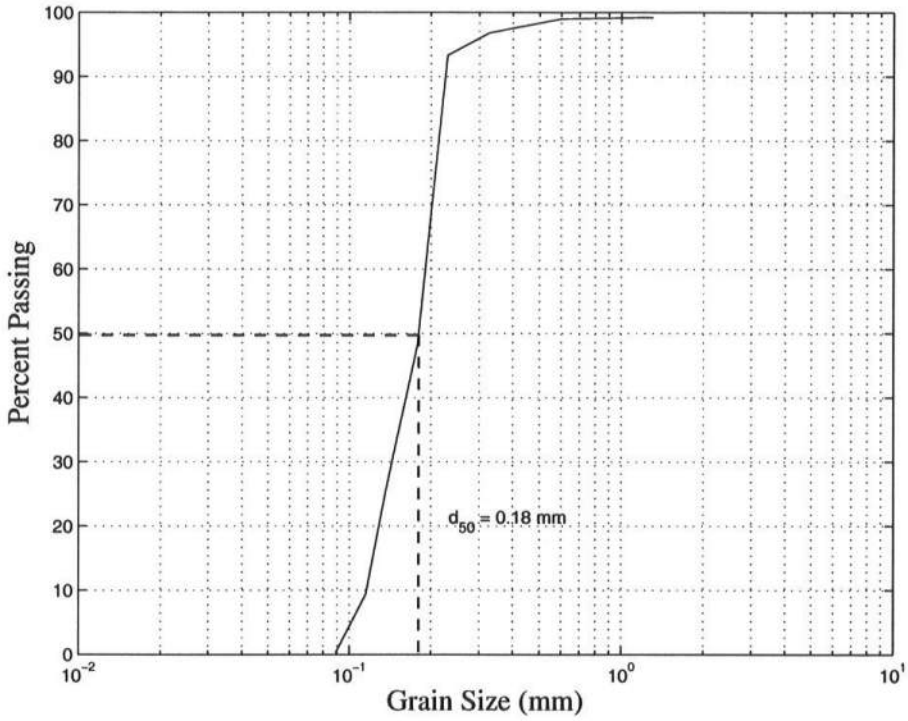

Figure 2.3: Sand grain size distribution

Table 2.1: Summary of sieve test

Sieve Size(mm)	Geometric Mean Diameter (mm)	Mass (g)	Percent of M_{total}	Percent Passing
2.0	-	0	0	100.0
0.850	1.300	2.3	0.77	99.2
0.425	0.601	0.8	0.27	99.0
0.250	0.326	6.5	2.20	96.8
0.212	0.230	10.1	3.44	93.3
0.150	0.178	132.6	45.12	48.2
0.125	0.137	65.7	22.34	25.9
0.106	0.115	48.3	16.42	9.4
0.075	0.089	26.8	9.13	0.3
Pan	-	0.9	0.30	0.0
TOTAL		293.9	100	-

Table 2.2: Wave gauge locations and water depths

Gauge	1	2	3	A	B	B'	C	C'	D	E
x(m)	0	0.22	0.92	5.0	6.35	6.5	7.6	8.0	9.5	10.5
d(cm)	71.36	68.64	64.07	20.32	20.26	19.63	19.14	20.00	18.94	4.15

proportional to each size group's percent of the total mass. The mean fall velocity obtained from the weighted averages was found to be $w_f = 2.0$ cm/s. The measured values of $s = 2.6$, $n_p = 0.4$ and $w_f = 2.0$ cm/s for test 2.6 are the same as those measured by Giovannozzi and Kobayashi [2002] and Tega et al. [2004] for tests 4.8 and 1.6.

2.3 Wave Gauge

The cross-shore locations of the eight capacitance wave gauges used to measure the temporal variations of the free surface elevations are shown in Figure 2.2. Wave gauges 1, 2 and 3 are located offshore and used to separate the incident and reflected waves in order to ensure the repeatability of the irregular waves. Wave gauges A and B are located in the breaker zone, C and D in the surf zone and E on the foreshore, buried in the sand. The horizontal coordinate x in this study is taken to be positive shoreward with x = 0 at the location of wave gauge 1. Wave gauges 2 and 3 are located at x = 0.22 and 0.92 m, respectively. For the first three runs of the velocity and concentration measurements at 4, 6 and 8 cm above the bottom at line A, the fifth and sixth wave gauges were located at B' and C' , respectively. For the other tests, the fifth and sixth wave gauges had to be moved to B and C, respectively, because of the locations of the side wall relative to the instrument carriage. The change did not influence the measurement of velocities and concentration. The cross-shore location x and the still water depth d for each wave gauge are shown in Table 2.2.

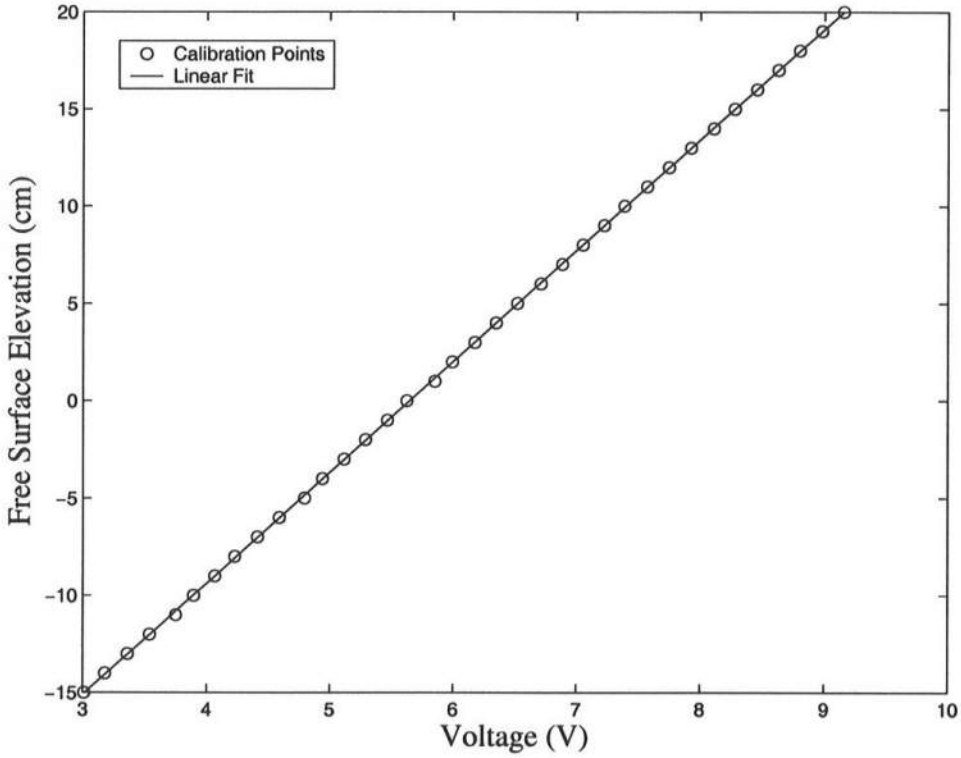

Figure 2.4: Wave gauge calibration for gauge 1

The wave gauges were calibrated before each run to ensure the accuracy of the experimental data. Calibrations were conducted by raising the water level 20 cm higher than the still water level and then gradually draining the tank while recording the wave gauge readings for every 1 cm change of the water level. This was done till the water level dropped 15 cm below the still water level. In total, 36 voltage readings for each wave gauge were obtained except for gauge E where the still water depth was 4.15 cm. As an example, the calibration data for wave gauge 1 followed a linear relation and is shown in Figure 2.4.

2.4 Acoustic-Doppler Velocimeters

Use was made of two Acoustic-Doppler Velocimeters (ADV). One with a 3D down-looking probe measured the cross-shore, alongshore and vertical velocities at a distance of 5 cm from the probe tip. The other with a 2D side-looking probe measuried the cross-shore and alongshore velocities at a distance of 5 cm from the probe tip. The velocities were measured at 12 different locations in a vertical plane above the equilibrium beach as shown by the dots in Figure 2.2. The sampling volume for both ADVs was approximately 0.1 cm^3. As depicted in Figure 2.5, the sampling volumes were at two alongshore symmetric locations, 13.5 cm from the flume centerline. The wave gauge was placed 22.5 cm laterally from the centerline when the velocities and concentrations were measured at the same cross-shore location.

The ADVs were fixed to adjustable mounts that can be raised or lowered to any desirable elevation above the local bottom. To ensure the accuracy of their elevations, the ADVs were repositioned before each test. The sampling volume elevation of the 3D ADV was determined using the ADV software supplied by the manufacturer within ± 0.5 mm and that of the 2D ADV was measured with a tape measure with ± 1 mm starting with the probe touching the local bottom. The software supplied by the manufacture also converts the ADV voltage into the corresponding velocities automatically. Therefore calibration was not required.

2.5 Fiber Optic Sediment Monitor

A Fiber Optic Sediment Monitor (FOBS-7) with two sensors was used to measure the sand concentration at the same elevation as the velocity measurement above the local bottom at the two alongshore locations as shown in Figure 2.5. The FOBS-7 is a laboratory version of the optic sensors used for concentration measurements on natural beaches [Downing *et al.*, 1981]. The monitor measures sediment concentration by detecting infrared radiation (IR) backscattered from particles in the water. The measurement area is limited to the volume where the transmit and

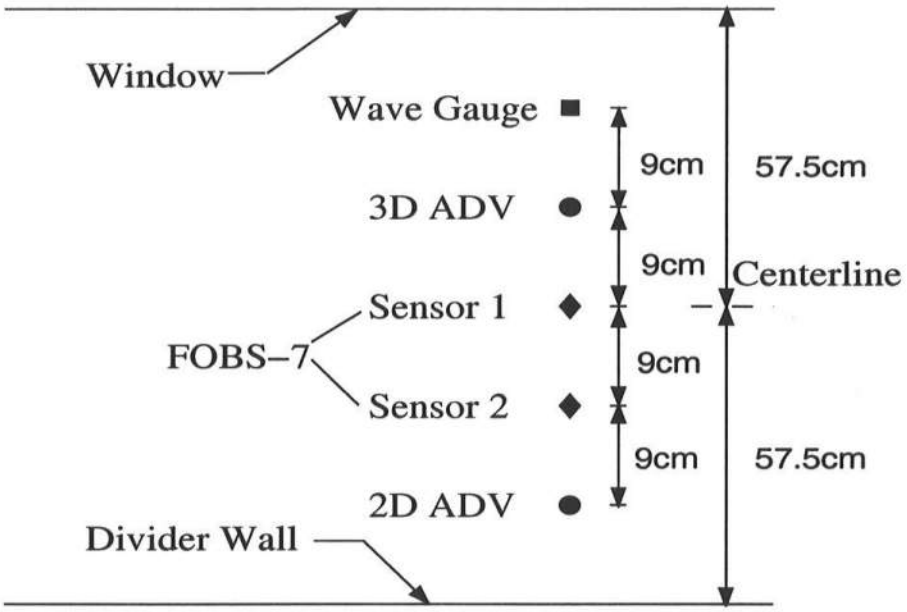

Figure 2.5: Alongshore ADV and FOBS locations

receive beams cross. The sampling volume is approximately 10 mm^3 and situated approximately 1.0 cm from the tip of the sensor.

The elevation, z_m, of the sampling volume was determined using an adjustable mount similar to the ADVs. The sensors were lowered to the local bottom to find $z_e = 0$ in Figure 2.6 where the readings of the sensors reached the maximum voltage value of about 2.6. Then, the sensors were raised very slowly in the still water to meet a sudden decrease of the readings, where this elevation was considered as $z_m = 0.0$ cm at the local bottom. The sensors were then raised to the desired elevation z_m. As shown in Figure 2.6, the sensors were mounted at an angle 30^0 from vertical. Thus, the sampling volume elevation z_m, was determined to be $z_m = (z_e - Rcos\theta + \frac{D}{2}sin\theta)$, where R is the distance of 1 cm from the sensor tip to the sampling volume, the diameter of the sensor D is 1 cm, and $\theta = 30^0$.

The sensors were calibrated before 12 runs by measuring the time series of the

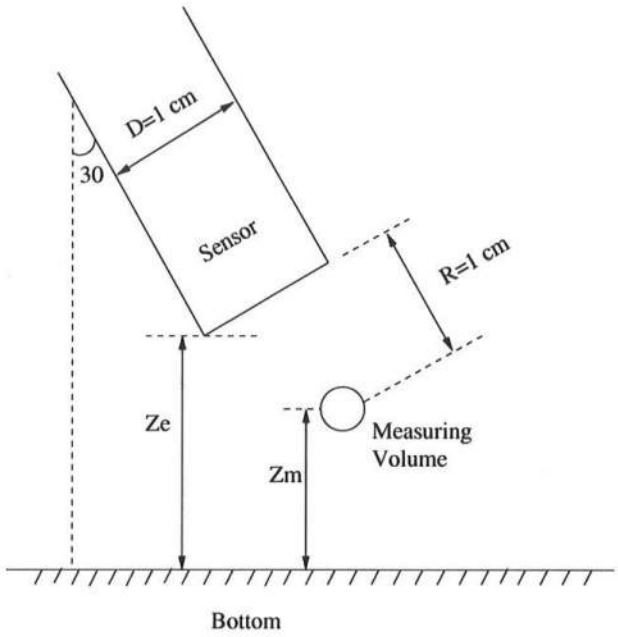

Figure 2.6: FOBS sensor positioning

voltage sampled at a rate of 20 Hz for 60 s for known sand concentrations in a well-mixed blender. For sensor 1, twenty-seven time series of the voltage were recorded for elevation 7, 8 and 9 cm above from the blender bottom with 0, 4, 8, 12, 16, 20, 24, 28 and 32 g sand in one liter water, respectively. For sensor 2, twenty-four time series of the voltage were recorded for elevation 7, 8 and 9 cm above from the blender bottom with 0, 4, 8, 12, 16, 20, 24 and 28 g sand in one liter water, respectively. The time-averaged voltage was used to establish the calibration relationship, whereas the fluctuating voltage was used to assess the error or uncertainty of this relationship which was about 20%. The calibration curves of the two sensors were shown in Figures 2.7 and 2.8.

2.6 Measurement of Beach Profiles

Two Panametrics 25DLHP ultrasonic depth gauges in deep water and a manual pointer with a vernier scale in the swash zone were employed to measure the

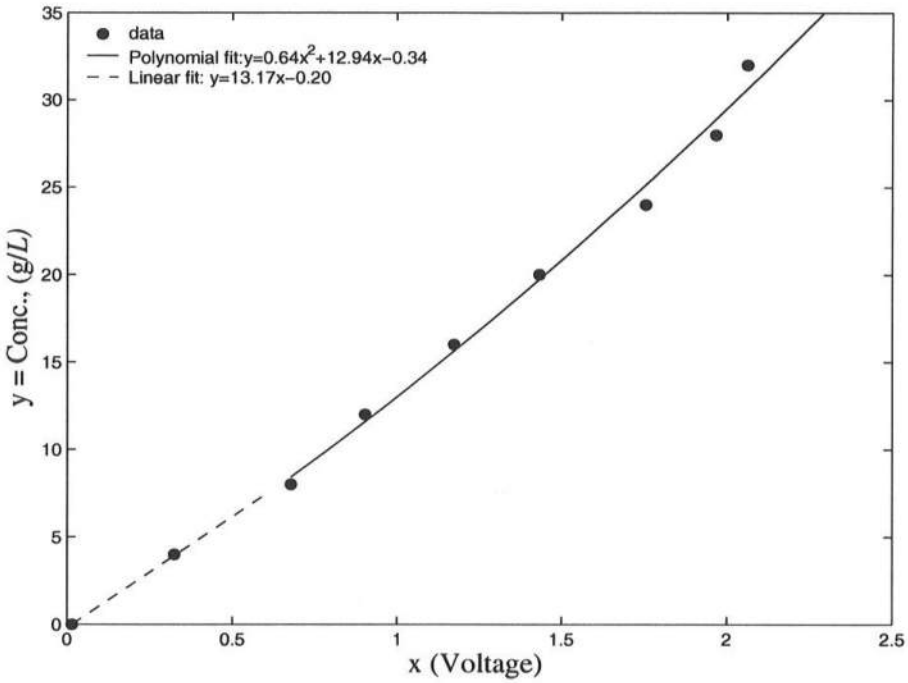

Figure 2.7: FOBS calibration curve for sensor 1

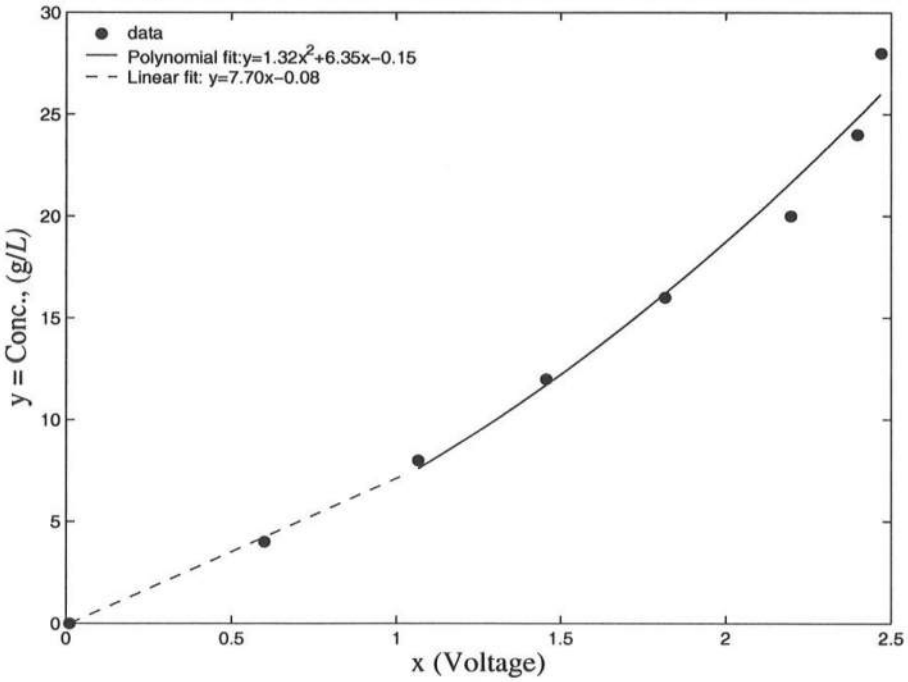

Figure 2.8: FOBS calibration curve for sensor 2

detailed bottom profile. The profile was measured every twenty bursts after the initial ten bursts before the profile reached equilibrium as shown in Figure 2.1. After the establishment of the equilbrium profile, the profile was also measured before and after the 12 runs on the equilibrium profile to ensure the negligible profile change during the 12 runs for test 2.6.

Profiles were taken along three cross-shore transects to ensure that there were little alongshore variations of the beach as discussed in section 2.1. The center transect was taken along the centerline of the 1.15-m wide wave flume and the other two were taken 23.5 cm on either side of the center transect. Each transect included 140 points with an overlap of 2 points at the transition from the ultrasonic depth gauge readings and the manual pointer readings. The spacing between measuring points of the ultrasonic depth gauge was 10 cm and that of the manual pointer was 5 cm. The alongshore variations were very small. Uniform two-dimensional ripples formed in the surf zone seaward of the steep slope of the foreshore in Figure 2.2 and three-dimensional ripples were present seaward of the sand bar. The height and length of ripples were approximately 0.7 and 8 cm, respectively.

2.7 Incident and Reflected Waves

The repeatability of the generated waves were checked by separating the incident and reflected waves for each of the 12 runs. The separated incident and reflected wave spectra were plotted together for all 12 runs, as shown in Figure 2.9 where the spectra were smoothed using band averaging with 16 degrees of freedom. The plotted spectra for the incident and reflected waves were almost indentical, which proves the repeatability of the tests. Table 2.3 lists the average values of the incident wave spectral peak period T_p, the incident spectral significant wave height $(H_{mo})_i$, the reflected spectral significant wave height $(H_{mo})_r$ and the average reflection coefficient $R = (H_{mo})_r/(H_{mo})_i$.

Table 2.3: Incident and reflected wave characteristics

T_p (s)	$(H_{mo})_i$ (cm)	$(H_{mo})_r$ (cm)	R
2.6	18.5	3.0	0.16

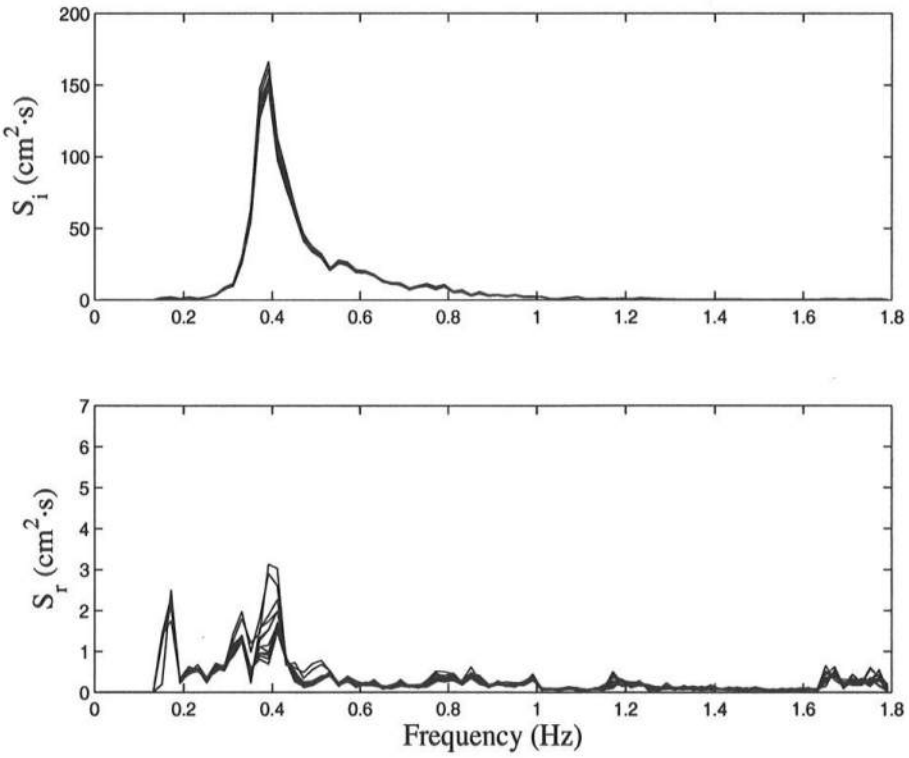

Figure 2.9: Frequency spectra for incident (top) and reflected (bottom) waves for 12 runs of test 2.6

Chapter 3

DATA ANALYSES

3.1 Overview of Three Tests

Two additional tests with the spectral peak periods of 4.8 and 1.6, respectively, were performed before test 2.6 in the same wave tank using the same fine sand. The sand beach was exposed to the specified irregular waves generated in a burst until the sand beach became quasi-equilibrium. The burst duration was 900 and 300 s for tests 4.8 and 1.6, respectively, in comparison with 400 s for test 2.6. The tests 4.8 and 1.6 were reported by Giovannozzi and Kobayashi [2002] and Tega et al. [2004]. Ten wave gauges were employed to measure the time series of the free surface elevation η above the still water level (SWL). Velocities and sediment concentrations were measured at seven cross-shore lines in the same way as for test 2.6 as shown in Figure 2.5. The experimental setup of these three tests are shown in Figure 3.1, where z is the vertical coordinate with $z = 0$ at SWL, the water depth in the flume was 0.9 m and the cross-shore coordinate x is positive onshore with $x = 0$ at wave gage 1 for each test.

Table 3.1 lists the sitll water depth, d, at the most seaward wave gauge 1 for the three tests where wave gauge 1 was located well outside the surf zone. The measured time series sampled at a rate of 20 Hz were repeatable within approximately 1% differences. The mean $\overline{\eta}$ and standard deviation σ_η of η are calculated for each wave gauge where the overbar indicates time averaging. The initial transition in each burst removed from the data analyses was 60, 10 and 20 s for tests

Table 3.1: Wave conditions at wave gauge 1 for tests 4.8, 1.6 and 2.6

T_p (s)	Duration (s)	d (cm)	$\overline{\eta}$ (cm)	H_{rms} (cm)	$(H_{rms})_i$ (cm)	Reflection Coefficient
4.8	900	80.6	-0.10	11.5	10.8	0.33
1.6	300	57.0	-0.13	11.7	11.6	0.14
2.6	400	71.4	-0.15	13.0	13.1	0.16

4.8, 1.6 and 2.6, respectively. The mean water depth $\overline{h}$ is the sum of $\overline{\eta}$ and the still water depth. The root-mean-square wave height H_{rms} is defined as $H_{rms} = \sqrt{8}\sigma_\eta$ in the following. Table 3.1 lists the values of $\overline{\eta}$ and H_{rms} at wave gauge 1 where the wave set-down was negligible and the wave height H_{rms} was in the range of 11.5 - 13.0 cm. The difference of the three equilibrium profiles were caused mostly by the difference of the spectral peak period T_p. The wave gauges 1 - 3 located outside the surf zone were also used to separate the incident and reflected waves using linear wave theory [Kobayashi et al., 1990]. The separated time series are used to obtain the root-mean-square wave heights $(H_{rms})_i$ and $(H_{rms})_r$ of the incident and reflected waves, respectively. Table 3.1 lists the values of $(H_{rms})_i$ and the reflection coefficient, $(H_{rms})_r/(H_{rms})_i$, where H_{rms} includes both incident and reflected waves but is approximately the same as $(H_{rms})_i$.

Table 3.2 lists the measured values of $\overline{\eta}$ and σ_η for the three tests where the onshore coordinate x with $x = 0$ at wave gauge 1 is used to indicate the cross-shore location of each gauge for each test. The still water depth d is also listed to indicate the gauge location on the equilibrium beach. These values of $\overline{\eta}$ and σ_η are plotted in chapter 4 in comparison with the corresponding predicted values.

The incident irregular waves on the terraced beach in test 4.8 did not break at gauge A, were breaking frequently at gauge B, broke intensely sometimes at gauges C and D, and became bores at gauges E - G. The height and cross-shore wavelength of ripples in the vicinity of gauge A were approximately 2 and 11 cm, respectively.

Table 3.2: Measured mean and standard deviation of free surface elevation η for tests 4.8, 1.6 and 2.6

Test	x (m)	d (cm)	$\overline{\eta}$ (cm)	σ_η (cm)
4.8	0	80.0	-0.1	4.06
	0.85	73.5	-0.1	3.99
	1.85	64.3	-0.2	3.91
	4.35	43.1	-0.2	4.63
	6.05	23.1	-0.5	4.60
	7.40	16.9	-0.2	3.76
	8.30	13.4	0.3	4.04
	9.30	11.2	0.8	3.14
	9.75	10.6	0.9	2.66
	9.95	10.2	0.9	2.68
1.6	0	54.1	-0.1	4.13
	0.10	53.4	-0.1	4.07
	0.55	50.3	-0.2	4.20
	2.05	24.0	-0.1	3.68
	2.35	22.2	0.0	3.17
	2.65	23.0	0.1	3.08
	3.25	26.6	0.2	2.95
	3.95	24.9	0.2	2.72
	4.75	23.4	0.2	2.72
	5.75	21.3	0.2	2.93
2.6	0	71.36	-0.15	4.59
	0.22	68.64	-0.17	4.59
	0.92	64.07	-0.18	4.56
	5.00	20.32	-0.48	5.11
	6.35	20.26	0.32	3.83
	6.50	19.63	0.34	3.69
	7.60	19.14	0.45	3.28
	8.00	20.00	0.53	3.17
	9.50	18.94	0.71	2.91
	10.50	4.15	0.72	2.63

No ripples were visible landward of gauge B inside the surf zone. For test 1.6, large incident waves broke at gauges A - C over the bar crest and became bores at gauges D - G in the bar trough region. The intensity of wave breaking was less on the barred beach and ripples were present in the surf zone. The height and cross-shore length of these ripples were approximately 1.3 cm and 6 cm, respectively. For test 2.6, the equilibrium profile was intermediate between the terraced and barred profiles in tests 4.8 and 1.6. The majority of incident waves broke at gauge A and above the bar crest and became bores at gauge B - C. Wave breaking was reduced considerately at gauge D. All waves broke on the steep slope of approximately 0.3 seaward of gauge E buried in the swash zone. The height and length of ripples in the region between gauges A and D were approximately 0.7 and 8 cm, respectively.

For each burst of the wave generation, the velocities and concentrations were measured at one particular location indicated by a dot in Figure 3.1. The number of dots in Figure 3.1 are 42, 40 and 12 for tests 4.8, 1.6 and 2.6, respectively. The measurement elevation was 1, 2, ... , n cm above the terraced beach in test 4.8 where the upper limit n along the vertical lines at each gauge location was decided by the submerged velocity measurement or negligible sand concentration. On the other hand, the measurement elevation z_m was 2, 4, ..., 2n cm above the barred beach in tests 1.6 and 2.6 except that the elevations of 3, 5, 7 and 9 cm were added for line 1.6D located at the deepest point of the bar trough. The different vertical lines in Figure 3.1 are identified by the numeral of each test followed by the letter of A to G. The same 3D ADV and 2D ADV were employed in tests 4.8 and 1.6 at the same alongshore locations as indicted in Figure 2.5 for test 2.6.

The measured horizontal velocities U_1 and U_2 were essentially in phase apart from high frequency oscillations associated with turbulence. The average horizontal velocity $U = (U_1 + U_2)/2$ is used here to calculate the mean $\overline{U}$ and the standard deviation σ_U at each measuring elevation.

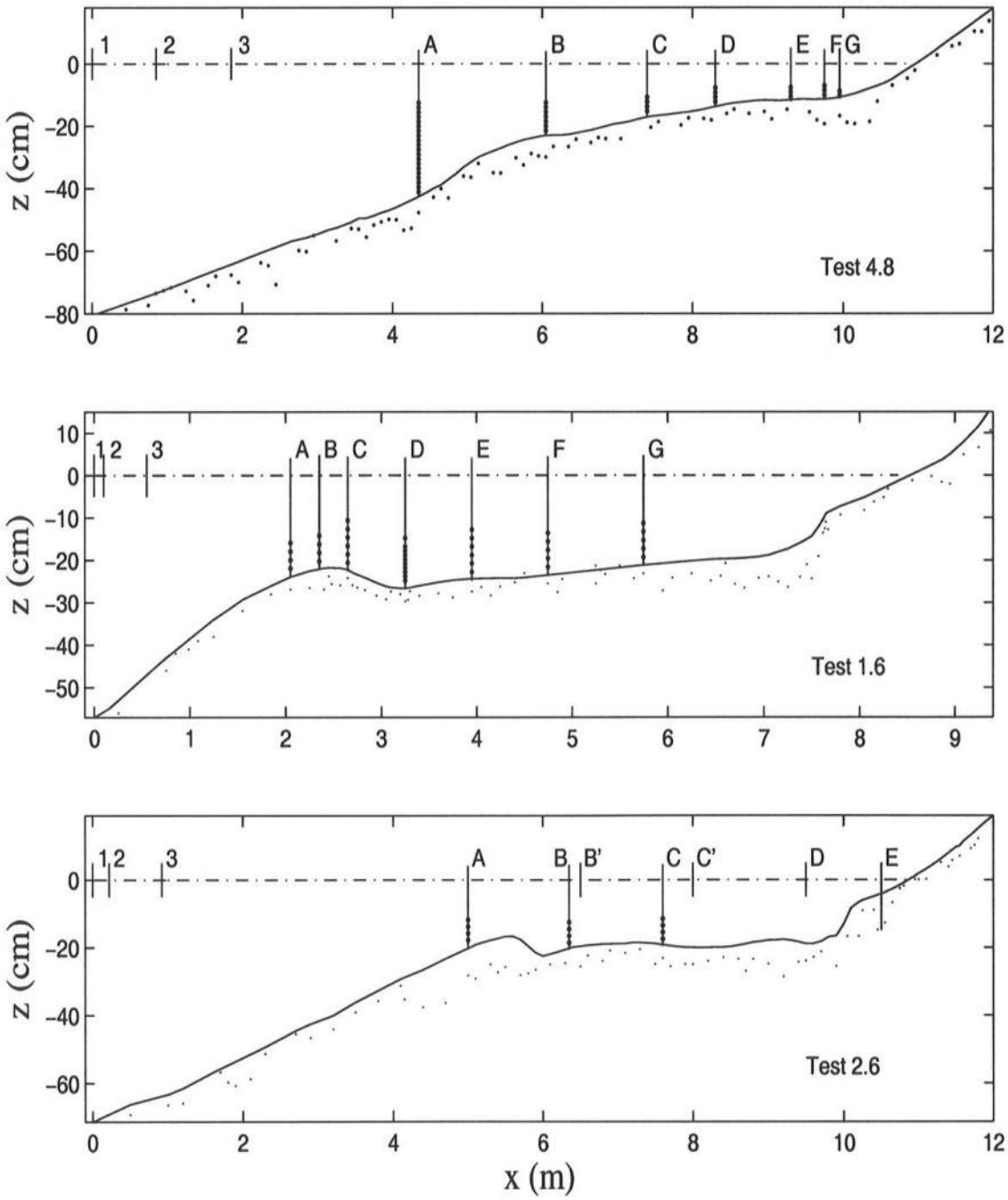

Figure 3.1: Cross-shore wage gauge locations of three tests

Table 3.3 lists the measured values of $\overline{U}$ and σ_U for the three tests where z_m is the elevation above the local bottom.The mean horizontal velocity $\overline{U}$ is negative and represents the offshore undertow current. The vertical distributions of $\overline{U}$ is discussed in section 3.2. The vertical variation of σ_U is small as was observed previously [e.g., Guza and Thornton, 1980].

To estimate the time-averaged turbulent velocity, use is made of the method proposed by Trowbridge [1998]. The measured velocities U_1 and U_2 are assumed to be expressible in the form

$$U_1 = \overline{U_1} + u_w + u_1^{'} \quad ; \quad U_2 = \overline{U_2} + u_w + u_2^{'} \tag{3.1}$$

where the wave component u_w is assumed to be the same and the prime indicates the turbulent component. Assuming that $\overline{u_1'^2} \simeq \overline{u_2'^2} \simeq \overline{u'^2}$ and $\overline{u_1' u_2'} \simeq 0$, the turbulent velocity variance $\overline{u'^2}$ is estimated as

$$\overline{u'^2} \simeq \frac{1}{2}\overline{[(U_1 - \overline{U_1}) - (U_2 - \overline{U_2})]^2} \tag{3.2}$$

Substitution of equation (3.1) into $U = (U_1 + U_2)/2$ yields $\overline{U} = (\overline{U_1} + \overline{U_2})/2$ and $\sigma_U^2 = \overline{(U - \overline{U})^2} \simeq \overline{u_w^2}$ where the wave velocity u_w was much larger than the turbulent velocities $u_1^{'}$ and $u_2^{'}$.

The measured alongshore velocities V_1 and V_2 did not contain any wave component. The turbulent velocity variance $\overline{v'^2}$ is estimated as the average of the two velocity variances

$$\overline{v'^2} \simeq \frac{1}{2}[\overline{(V_1 - \overline{V_1})^2} + \overline{(V_2 - \overline{V_2})^2}] \tag{3.3}$$

where the measured mean $\overline{V_1}$ and $\overline{V_2}$ were practically zero.

The vertical velocity W was measured by the 3D probe only. It is noted that the use of the 2D and 3D probes was intended for the comparison of the horizontal velocity measurements in the vicinity of the bottom. The measured vertical velocity was relatively small and appeared to correspond to the fluid velocity in the region

Table 3.3: Measured mean and standard deviation of horizontal velocity U for three tests

Test	$x(m)$	$z_m(cm)$	$\overline{U}(cm/s)$	$\sigma_U(cm/s)$	Test	$x(m)$	$z_m(cm)$	$\overline{U}(cm/s)$	$\sigma_U(cm/s)$
		1	-1.3	14.1			4	-5.1	21.5
		2	-2.0	18.5		2.35	6	-5.3	21.8
		3	-2.1	17.9			8	-6.0	21.9
		4	-1.7	17.1			2	-3.0	19.3
		5	-2.1	17.9			4	-5.2	19.8
		6	-2.3	17.9		2.65	6	-5.7	19.7
		7	-2.4	17.8			8	-6.0	19.6
		8	-2.4	17.9			10	-6.5	19.9
		9	-2.3	18.2			12	-6.4	20.0
	4.35	10	-2.2	18.0			2	-6.4	15.6
		11	-2.2	17.9			3	-6.4	15.4
		12	-2.0	18.1			4	-7.1	15.6
		13	-2.1	18.1			5	-7.5	15.5
		14	-1.9	18.1		3.25	6	-7.1	15.8
		15	-1.7	18.3			7	-7.1	15.5
		16	-1.8	18.3			8	-6.7	15.8
		17	-1.8	18.4			9	-6.1	15.8
		18	-1.6	18.4	1.6		10	-6.4	15.6
		19	-1.4	18.5			12	-5.2	16.1
		20	-1.6	18.6			2	-5.4	15.9
		1	-5.0	27.9			4	-5.9	15.8
4.8		2	-6.3	29.0			6	-5.9	16.0
		3	-6.7	28.5		3.95	8	-6.0	16.1
	6.05	4	-6.9	28.0			10	-5.7	16.3
		5	-7.3	29.2			12	-4.7	16.6
		6	-7.2	29.7			2	-4.4	16.5
		7	-6.6	29.2			4	-4.0	15.9
		1	-6.1	28.3		4.75	6	-4.6	17.0
		2	-6.9	28.8			8	-4.2	17.1
	7.40	3	-7.6	28.4			10	-3.7	17.6
		4	-6.7	27.4			2	-2.0	18.3
		1	-7.2	23.3			4	-2.6	18.1
	8.30	2	-7.6	24.3		5.75	6	-3.0	17.2
		3	-6.5	23.2			8	-3.2	17.3
		1	-5.3	25.7			10	-3.0	17.6
	9.30	2	-5.2	25.8			2	-5.38	26.30
		3	-4.8	25.7			4	-6.48	26.36
		1	-3.2	25.6		5.00	6	-7.20	27.35
	9.75	2	-3.7	25.9			8	-7.03	27.36
		3	-3.1	25.7			2	-8.12	18.28
		1	-3.0	27.1			4	-7.97	18.80
	9.95	2	-3.0	26.4	2.6	6.35	6	-8.94	19.01
		2	-3.0	18.0			8	-8.15	19.04
		4	-3.2	17.6			2	-5.95	16.77
1.6	2.05	6	-2.9	17.9			4	-7.46	17.50
		8	-3.1	18.3		7.60	6	-6.67	17.43
	2.35	2	-3.8	21.9			8	-5.76	17.50

of very small sand concentrations and an intermediate velocity between the fluid and sand velocities in the region of high sand concentrations. The mean velocity $\overline{W}$ is compared with the sand fall velocity $w_f = 2.0$ cm/s measured in quite water as depicted in Figure 3.2. The measured values of $\overline{W}/w_f$ were in the range of -0.88 to 0.30 with the average being -0.34. The variance σ_W^2 of the measured vertical velocity increased upward due to the increase of the wave-induced vertical velocity with the elevation z_m above the local bottom. Assuming no correlation between the wave and turbulent components, the turbulent variance $\overline{w'^2}$ is crudely estimated as

$$\overline{w'^2} \simeq \sigma_W^2 - \left(\frac{2\pi\sigma_\eta}{T_p}\frac{z_m}{\overline{h}}\right)^2 \tag{3.4}$$

where linear long wave theory [e.g., Dean and Dalrymple, 1984] is used to estimate the wave velocity variance using the measured values of σ_η and $\overline{h}$ at each line and the wave period represented by the peak period T_p. The turbulent velocity variances estimated using equations (3.2) - (3.4) are presented in section 3.2.

The measured sediment concentrations C_1 and C_2 by the two FOBS-7 sensors were not always in phase, but intermittent high concentration events occurred simultaneously in both time series. The average concentration $C = (C_1 + C_2)/2$ is used here to calculate the mean $\overline{C}$ and the standard deviation σ_C at each measuring elevation. The synchronous measurements of U and C are used to obtain the correlation coefficient γ_{UC} defined as

$$\gamma_{UC} = \overline{(U - \overline{U})(C - \overline{C})}/(\sigma_U \sigma_C) \tag{3.5}$$

Table 3.4 lists the measured values of $\overline{C}, \sigma_C$ and γ_{UC} for the three tests where the sediment concentration is expressed in grams per liter. The vertical variations of these values are analyzed in section 3.3 where use is made of the volumetric concentration which equals C (g/l) divided by 2,600 for the present sand with the specific gravity s = 2.6 in fresh water.

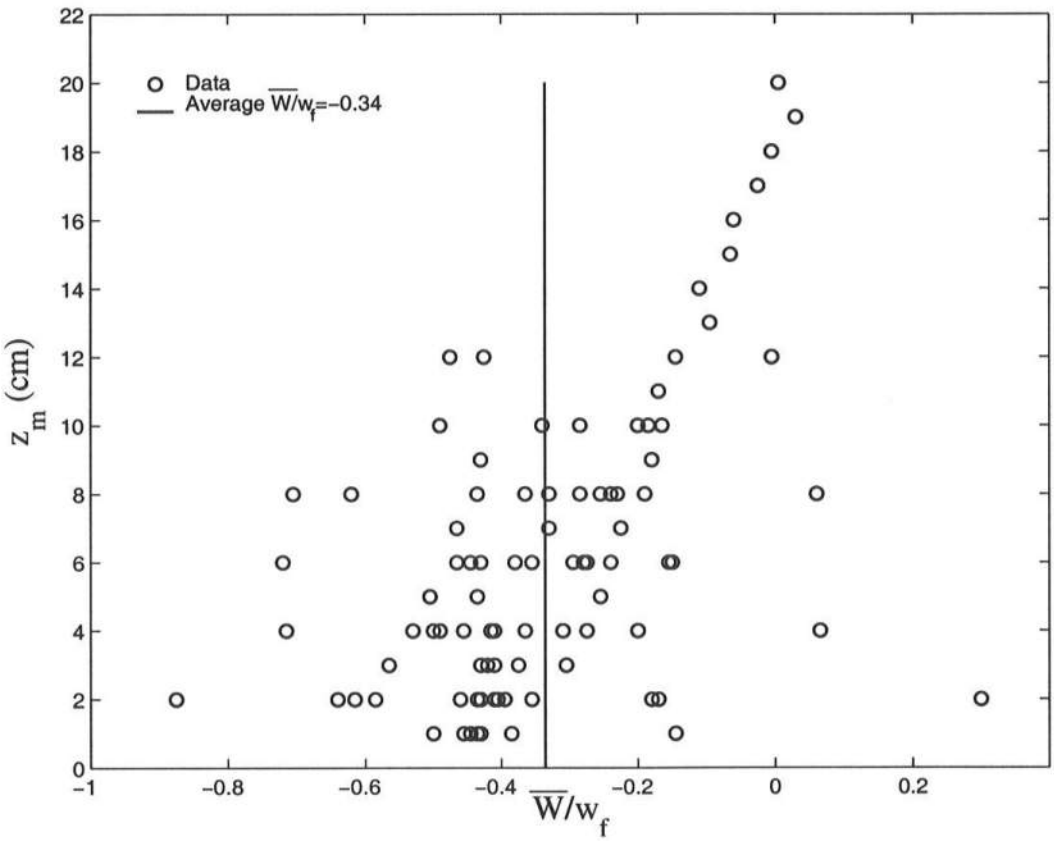

Figure 3.2: Ratio between measured mean vertical velocity $\overline{W}$ and sediment fall velocity w_f at elevation z_m above local bottom for three tests

Table 3.4: Measured mean and standard deviation of sediment concentration C and correlation coefficeint γ_{UC} between U and C for tests 4.8, 1.6 and 2.6

Test	$x(m)$	z_m (cm)	$\overline{C}(g/l)$	$\sigma_C(g/l)$	γ_{UC}
4.8	4.35	1	7.43	9.48	0.28
		2	2.30	3.53	0.33
		3	1.24	2.05	0.32
		4	0.82	1.63	0.21
		5	0.46	0.74	0.18
		6	0.42	1.00	0.06
		7	0.33	0.79	0.06
		8	0.29	0.55	0.05
		9	0.29	0.65	0.04
		10	0.27	0.54	0.06
		11	0.30	0.72	0.06
		12	0.26	0.60	0.03
		13	0.27	0.49	0.09
		14	0.24	0.35	0.11
		15	0.26	0.60	0.06
		16	0.23	0.37	0.08
		17	0.21	0.30	0.07
		18	0.23	0.27	0.12
		19	0.23	0.43	0.05
		20	0.20	0.17	0.11
	6.05	1	3.60	5.56	0.15
		2	3.57	5.99	0.13
		3	2.44	3.59	0.13
		4	1.95	3.04	0.09
		5	2.82	4.98	0.09
		6	2.80	5.07	0.09
		7	2.40	4.31	0.08
	7.40	1	5.66	6.11	0.18
		2	4.83	5.45	0.18
		3	4.24	4.83	0.18
		4	3.93	4.59	0.18
	8.30	1	3.93	5.37	0.19
		2	3.17	4.37	0.17
		3	2.65	3.59	0.18
	9.30	1	1.79	2.67	0.23
		2	1.45	2.32	0.23
		3	1.22	1.98	0.21
	9.75	1	1.24	2.03	0.21
		2	0.67	1.07	0.20
		3	0.68	1.12	0.20
	9.95	1	0.40	0.70	0.20
		2	0.49	0.69	0.19
1.6	2.05	2	4.84	4.66	0.15
		4	1.60	1.52	0.14
		6	0.82	0.78	0.10
		8	0.60	0.34	0.09

Table 3.4: continued (NR implies 'not reliable')

Test	$x(m)$	z_m (cm)	$\overline{C}(g/l)$	$\sigma_C(g/l)$	γ_{UC}
1.6	2.35	2	6.57	5.93	0.08
		4	3.62	3.74	0.04
		6	2.49	2.39	0.02
		8	1.91	2.38	-0.02
	2.65	2	4.33	3.02	0.104
		4	2.61	1.93	0.065
		6	2.17	1.80	0.041
		8	1.58	1.19	0.047
		10	1.43	1.39	0.014
		12	1.02	0.91	0.002
	3.25	2	2.00	1.40	-0.021
		3	1.31	0.94	0.029
		4	1.18	0.81	0.003
		5	0.97	0.66	-0.047
		6	1.01	0.73	0.024
		7	1.05	0.58	-0.031
		8	0.78	0.54	0.022
		9	0.80	0.59	0.003
		10	0.69	0.45	0.018
		12	0.68	0.51	0.006
	3.95	2	1.57	1.26	0.063
		4	0.83	0.53	0.060
		6	0.62	0.37	0.075
		8	0.48	0.30	0.014
		10	0.44	0.27	0.004
		12	0.36	0.23	-0.009
	4.75	2	2.52	1.76	NR
		4	1.00	0.72	0.103
		6	0.63	0.42	0.109
		8	0.37	0.24	0.075
		10	0.32	0.22	0.035
	5.75	2	2.11	1.59	NR
		4	1.02	0.75	0.157
		6	0.61	0.44	0.153
		8	0.34	0.24	0.122
		10	0.31	0.17	0.077
2.6	5.00	2	5.19	4.96	0.250
		4	4.63	4.91	0.193
		6	3.91	4.52	0.163
		8	3.10	4.01	0.125
	6.35	2	3.27	2.93	0.133
		4	2.71	2.29	0.097
		6	2.38	2.38	0.049
		8	2.10	1.65	0.070
	7.60	2	1.72	0.89	0.222
		4	1.20	0.55	0.177
		6	1.06	0.51	0.163
		8	0.97	0.41	0.163

3.2 Vertical Variations of Velocity Data

The vertical variation of the mean cross-shore velocity $\overline{U}$ is normally predicted using the time-averaged cross-shore momentum equation which includes the terms related to the correlation between the measured velocity U and W [Deigaard and Fredsφe, 1989]. The correlation coefficient γ_{UW} defined in the form of equation (3.5) with C being replaced by W is calculated and plotted as a function of z_m as shown in Figure 3.3 to examine the reliability of the measured γ_{UW} in comparison with the data of Cox and Kobayashi [1996] who conducted an experiment on a fixed bottom. The comparison indicates that the measured γ_{UW} is not reliable because the relatively small velocity W was affected by the suspended sand.

Alternatively, the measured $\overline{U}$ at each line is fitted to the parabolic profile [Svendsen, 1984]

$$\overline{U} = a_U z_m^2 + b_U z_m + c_U \tag{3.6}$$

where a_U, b_U and c_U are the coefficients determined to minimize the mean square error. Figure 3.4 compares the measured $\overline{U}$ with the fitted $\overline{U}$ using equaiton (3.6) for the three tests. The correlation coefficient between the measured and fitted values, denoted as CC hereafter, is 0.996. As a result, equation (3.6) may be used to extrapolate the measure $\overline{U}$ to the range of $0 < z_m < h_0$ where $\overline{U} = 0$ at $z_m = h_0$ and $\overline{U} < 0$ for $0 < z_m < h_0$. The vertical distance $(\overline{h} - h_0)$ below the mean water level with $\overline{h}$ being the measured mean water depth is of the order of $2\sigma_\eta$ except for the lines 1.6A - C and 2.6A - B near the bar crest where $(\overline{h} - h_0)$ is of the order of $0.5\sigma_\eta$ as shown in Figure 3.5. The time-averaged offshore volume flux q_0 and corresponding velocity $\overline{U_0}$ are defined as

$$q_0 = \int_0^{h_0} (-\overline{U}) dz_m \qquad ; \qquad \overline{U_0} = q_0/h_0 \tag{3.7}$$

where equation (3.6) is used to find the positive values of q_0 and $\overline{U_0}$ at each line.

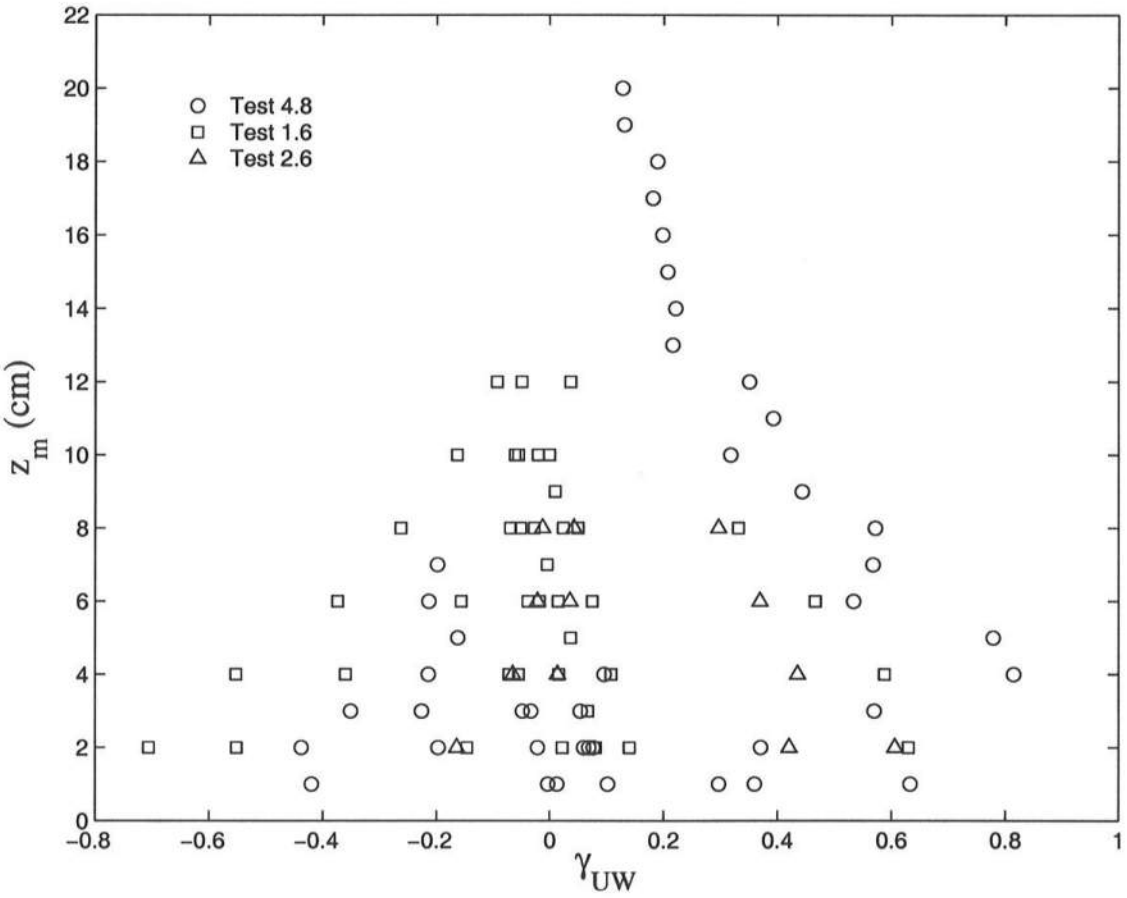

Figure 3.3: Correlation coefficient γ_{UW} between measured horizontal and vertical velocities at elevation z_m above the local bottom for tests 4.8, 1.6 and 2.6

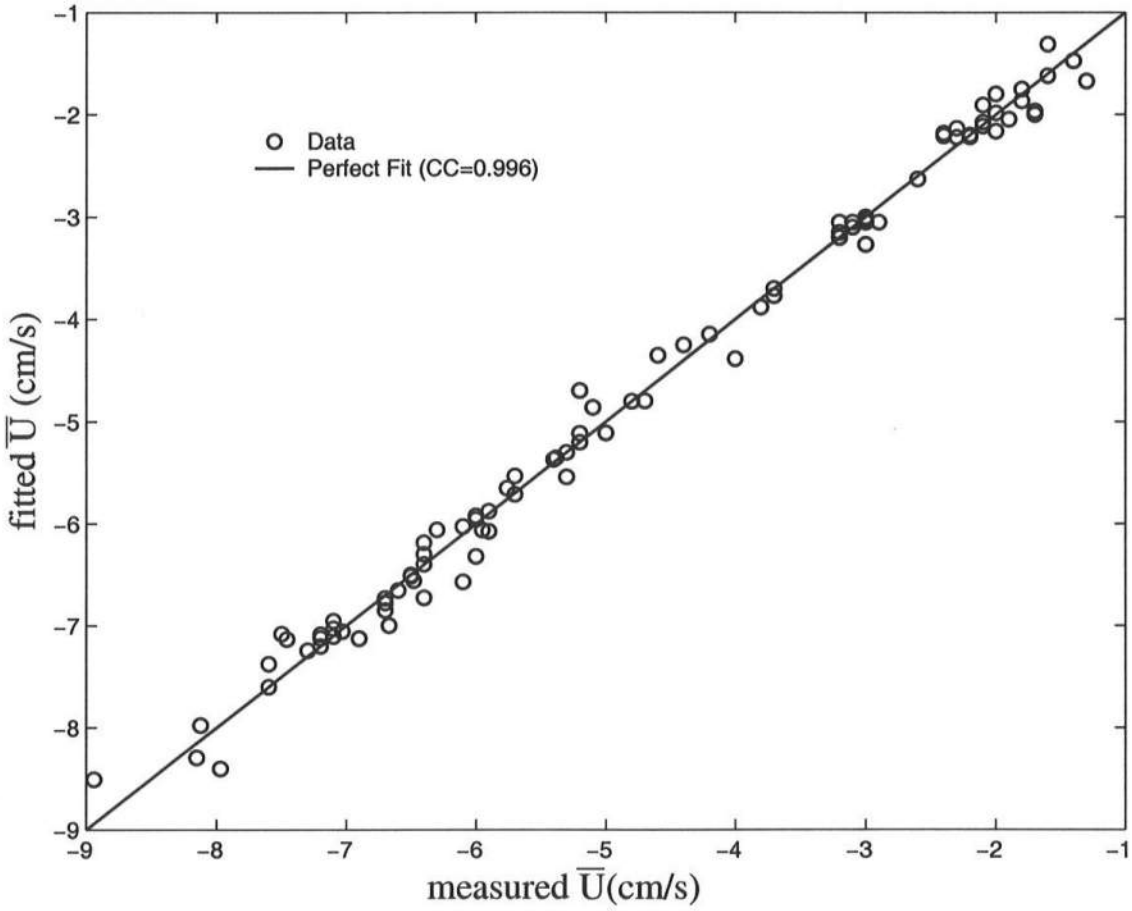

Figure 3.4: Comparison between measured mean horizontal velocity $\overline{U}$ and fitted $\overline{U}$ using parabolic undertow profile for three tests

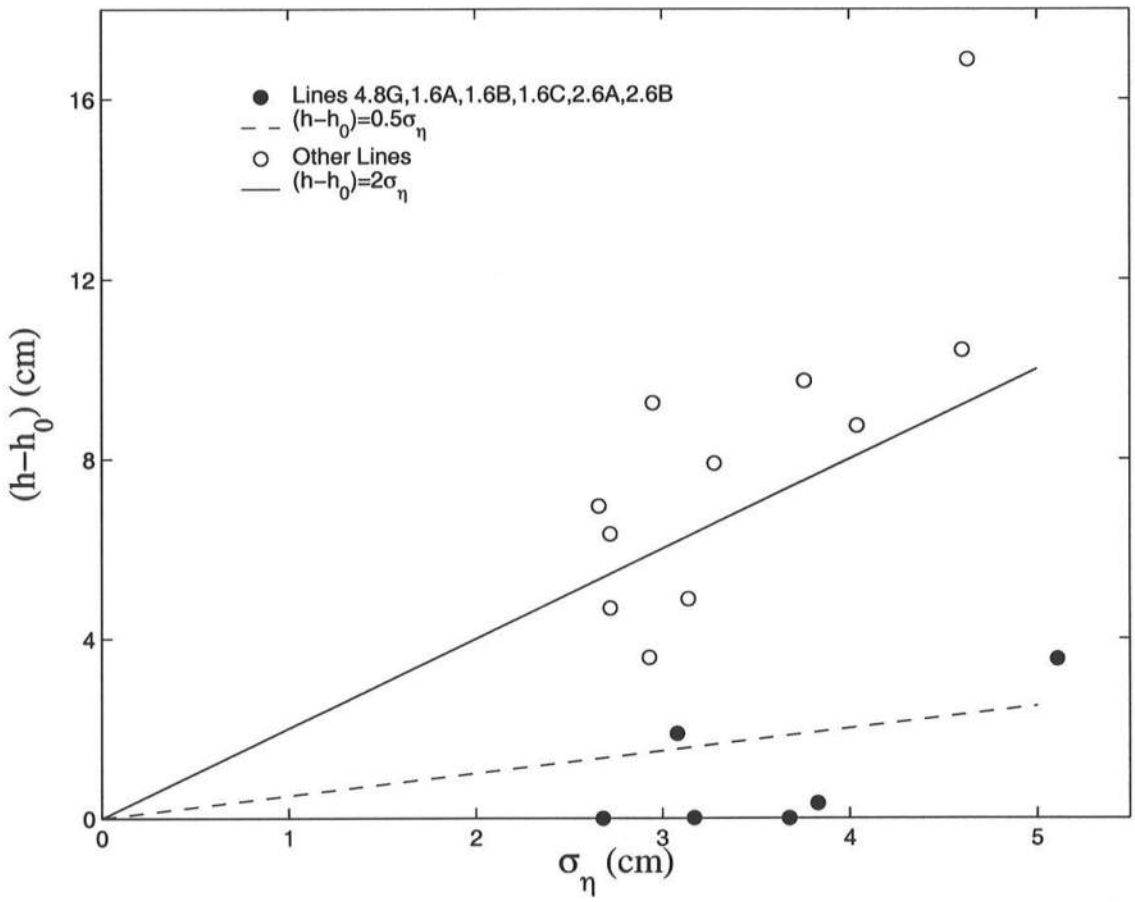

Figure 3.5: Vertical distance $(\overline{h} - h_0)$ below mean water level as a function of the standard deviation of the free surface elevation σ_η at each line for three tests

The time-averaged turbulent kinetic energy k per unit mass is defined as

$$k = \frac{1}{2}(\overline{u'^2} + \overline{v'^2} + \overline{w'^2}) \tag{3.8}$$

where the turbulent velocity variances are obtained using equation (3.2) - (3.4). Figure 3.6 shows that the relations between the turbulent velocity variances which are approximated as

$$\overline{u'^2}/(2k) \simeq 0.6 \quad ; \quad \overline{v'^2}/(2k) \simeq 0.3 \quad ; \quad \overline{w'^2}/(2k) \simeq 0.1 \tag{3.9}$$

The value of CC for each empirical equation is shown in Figure 3.6 and subsequent figures. It is noted that equation (3.4) yields $\overline{w'^2} < 0$ at $z_m = 6$ and 8 cm for line 1.6A and at $z_m = 6$, 8 and 10 cm for line 1.6G. These five points plotted as $\overline{w'^2} = 0$ in Figure 3.6 are in the range of $k < 12\ cm^2/s^2$. The ratios in equation (3.9) are similar to those associated with the boundary layer flow in the inner region [Svendsen, 1987]. Equation (3.9) is applicable only to the region of the velocity measurements in Figure 3.1 where no velocities were measured near the free surface.

Table 3.5 lists the turbulent velocity $k^{0.5}$ for the three tests. The time-averaged turbulent velocity $k^{0.5}$ has been assumed to decay exponentially downward [Svendsen, 1987; Roelvink and Stive, 1989]. The measured values of $k^{0.5}$ at each line are fitted to the exponential distribution

$$k^{0.5} = u_0' exp(z_m/\ell_t) \tag{3.10}$$

where u_0' is the turbulent velocity extrapolated to the bottom at $z_m = 0$ and ℓ_t is the vertical length scale of $k^{0.5}$. Figure 3.7 shows $k^{0.5}/u_0'$ as a function of $z_m/\mid \ell_t \mid$ where use is made of the fitted values of u_0' and ℓ_t at each line. At lines 4.8A, 1.6A,1.6G and 2.6A, where wave breaking was infrequent or weak, $\ell_t < 0$ and $k^{0.5}$ decreased upward in the region of the velocity measurement. The length scale is approximately given by $\mid \ell_t \mid \simeq \overline{h}$ with $CC = 0.81$ except that $\ell_t/\overline{h} = 2.8$ and 5.8 at lines 1.6B and 1.6C, respectively, as shown in Figure 3.8. At these two lines above

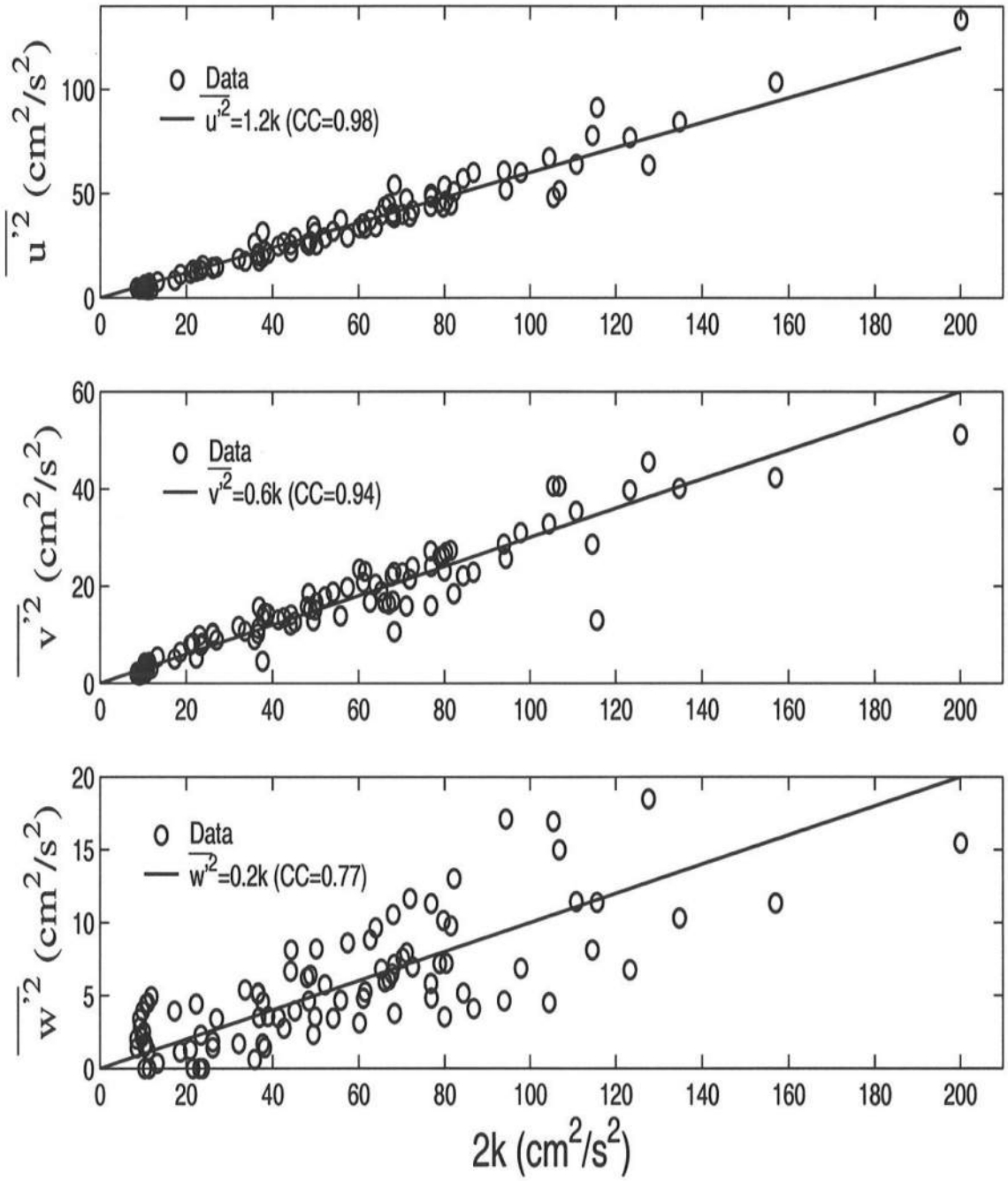

Figure 3.6: Measured turbulent velocity variances $\overline{u'^2}$, $\overline{v'^2}$ and $\overline{w'^2}$ as a function of $2k = (\overline{u'^2} + \overline{v'^2} + \overline{w'^2})$

Table 3.5: Measured time-averaged turbulent velocity $k^{0.5}$ for tests 4.8, 1.6 and 2.6

Test	$x(m)$	$z_m(cm)$	$k^{0.5}(cm/s)$	Test	$x(m)$	$z_m(cm)$	$k^{0.5}(cm/s)$
4.8	4.35	1	4.34	1.6	2.35	4	4.55
		2	3.34			6	4.94
		3	3.05			8	5.01
		4	4.29		2.65	2	6.20
		5	3.67			4	5.96
		6	3.24			6	5.75
		7	2.37			8	6.49
		8	2.28			10	6.59
		9	2.28			12	6.33
		10	2.07		3.25	2	4.41
		11	2.31			3	5.11
		12	2.21			4	4.92
		13	2.06			5	4.90
		14	2.26			6	5.82
		15	2.16			7	5.93
		16	2.14			8	6.02
		17	2.23			9	6.38
		18	2.32			10	6.20
		19	2.36			12	7.22
		20	2.44		3.95	2	4.10
	6.05	1	4.98			4	4.28
		2	5.00			6	4.28
		3	5.85			8	4.71
		4	5.79			10	5.71
		5	5.60			12	5.66
		6	5.83		4.75	2	3.42
		7	6.41			4	3.61
	7.40	1	6.85			6	3.61
		2	6.99			8	4.01
		3	7.57			10	4.37
		4	8.86		5.75	2	5.28
	8.30	1	7.85			4	4.23
		2	8.21			6	3.45
		3	10.00			8	3.29
	9.30	1	6.34			10	3.40
		2	6.31	2.6		2	7.60
		3	7.44			4	4.70
	9.75	1	5.49		5.00	6	4.34
		2	5.55			8	4.75
		3	6.28		6.35	2	5.84
	9.95	1	5.53			4	7.31
		2	6.20			6	7.26
1.6	2.05	2	2.94			8	7.99
		4	2.58		7.60	2	5.20
		6	2.28			4	5.36
		8	2.39			6	6.00
	2.35	2	4.62			8	6.87

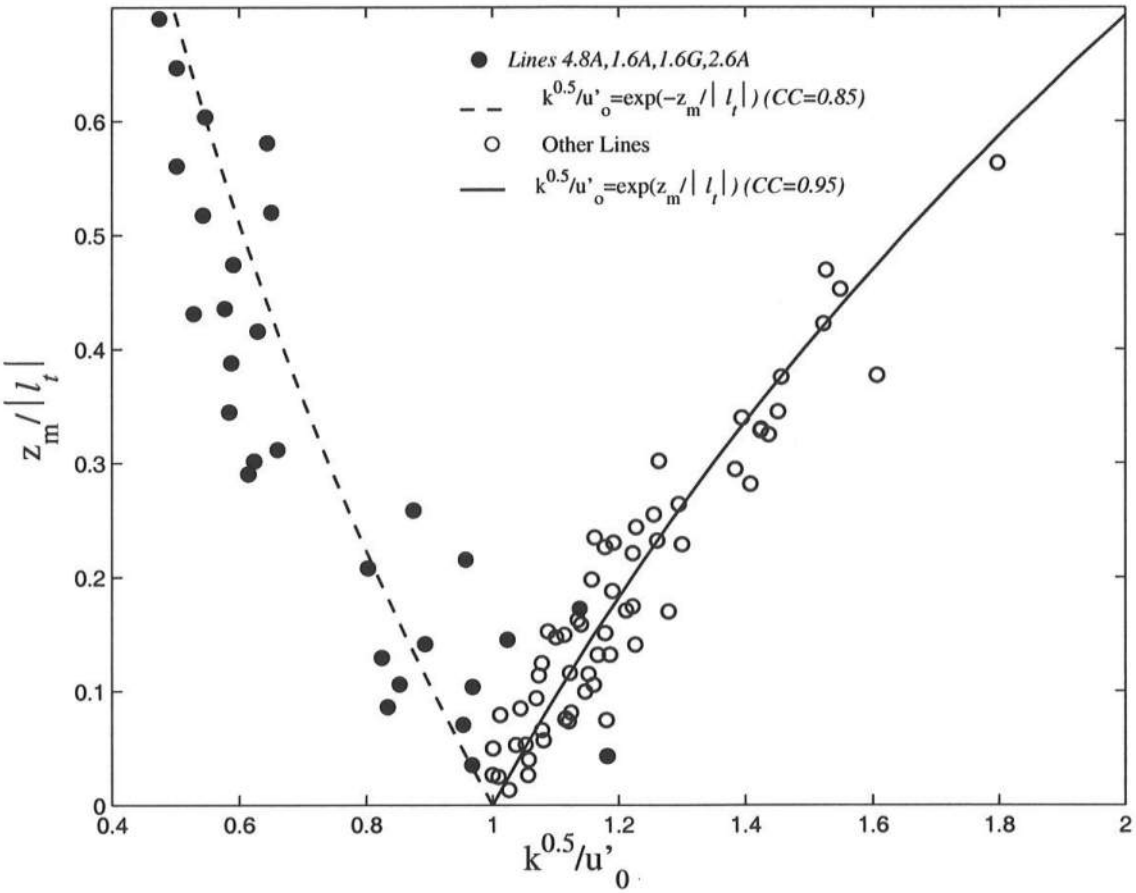

Figure 3.7: Vertical distribution of turbulent velocity $k^{0.5}$ expressed as $k^{0.5} = u_0' exp(z_m/\ell_t)$ at each line where $\ell_t < 0$ at lines 4.8A, 1.6A, 1.6G and 2.6A

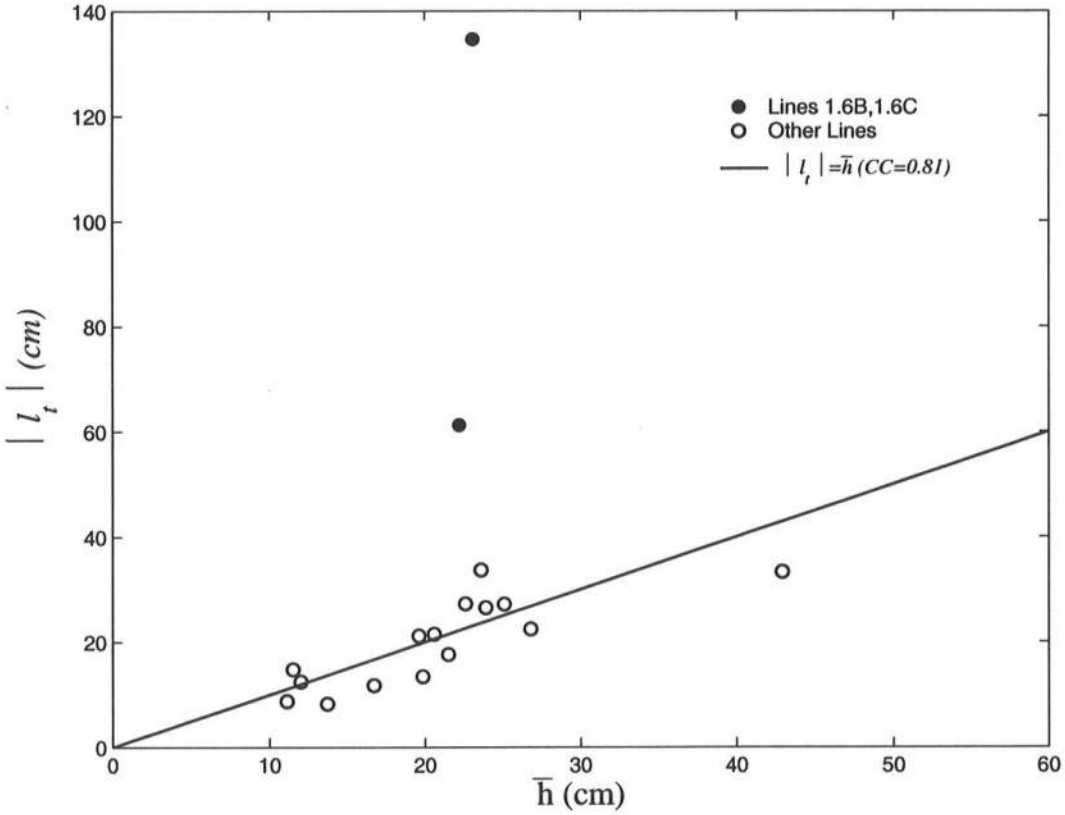

Figure 3.8: Vertical length scale ℓ_t of time-averaged turbulent velocity $k^{0.5}$ as a function of mean water depth $\overline{h}$

the bar crest, the upward increase of $k^{0.5}$ was very small. The fitted values of u_0' and $u_0' exp(z_m/\ell_t)$ at each line are compared with the computed turbulent velocities due to bottom friction and wave breaking in chapter 4.

3.3 Vertical Variations of Concentration Data

The concentration data are analyzed on the basis of the continuity equation of suspended sediment which is expressed as

$$\frac{\partial C}{\partial t} + \frac{\partial}{\partial x_j}[(U_j - w_f \delta_{j3})C] = 0 \tag{3.11}$$

where use is made of the repeated indexes with j = 1, 2 and 3, t is time, x_j is the Cartesian coordinate system with x_3 being the vertical coordinate, positive upward, C is the instantaneous volumetric sediment concentration, U_j is the instantaneous fluid velocity, w_f is the sediment fall velocity, and δ_{j3} is the Kronecker delta. The continuity equation of fluid is given by $\partial U_j/\partial x_j = 0$ where the volumetric concentration C is assumed to be much smaller than unity. In equation (3.11), the molecular diffusion of C is neglected and the sediment velocity is assumed to be given by $(U_j - w_f\delta_{j3})$ so as to avoid the use of the sediment momentum equations [e.g., Hsu and Liu, 2004]. Ensemble averaging of equation (3.11) yields

$$\frac{\partial \overline{C}}{\partial t} + \frac{\partial}{\partial x_j}[(\overline{U_j} - w_f\delta_{j3})\overline{C} + \overline{u_j c}] = 0 \tag{3.12}$$

where the overbar denotes ensemble averaging, which is later assumed to be the same as time averaging, $u_j = (U_j - \overline{U_j})$ is the fluctuating velocity, and $c = (C - \overline{C})$ is the fluctuating concentration. The equation for c is obtained by subtracting equation (3.12) from equation (3.11). Multiplying this equation by c and ensemble averaging the resulting equation, the equation for $\overline{c^2}$ is obtained

$$\frac{\partial}{\partial t}\left(\overline{c^2}\right) + \left(\overline{U_j} - w_f\delta_{j3}\right)\frac{\partial}{\partial x_j}\left(\overline{c^2}\right) = -\frac{\partial}{\partial x_j}\left(\overline{u_j c^2}\right) - 2\overline{u_j c^2}\frac{\partial \overline{C}}{\partial x_j} \tag{3.13}$$

The assumptions of steadiness, horizontal uniformity and $\overline{U_3} = 0$ may be made for the suspended sediment transport on the equilibrium beach in the present experiment. Under these assumptions, equations (3.12) and (3.13) are simplified as

$$\overline{wc} = w_f\overline{C} \tag{3.14}$$

$$w_f\frac{\partial}{\partial z}\left(\overline{c^2}\right) = \frac{\partial}{\partial z}\left(\overline{wc^2}\right) + 2\overline{wc}\frac{\partial \overline{C}}{\partial z} \tag{3.15}$$

where $w = u_3$ is the vertical fluctuating fluid velocity, $z = x_3$ is the vertical coordinate, and the overbar is regarded as time averaging. Substitution of equation (3.14) into equation (3.15) yields

$$w_f\overline{c^2} = \overline{wc^2} + w_f\left(\overline{C}\right)^2 + A \tag{3.16}$$

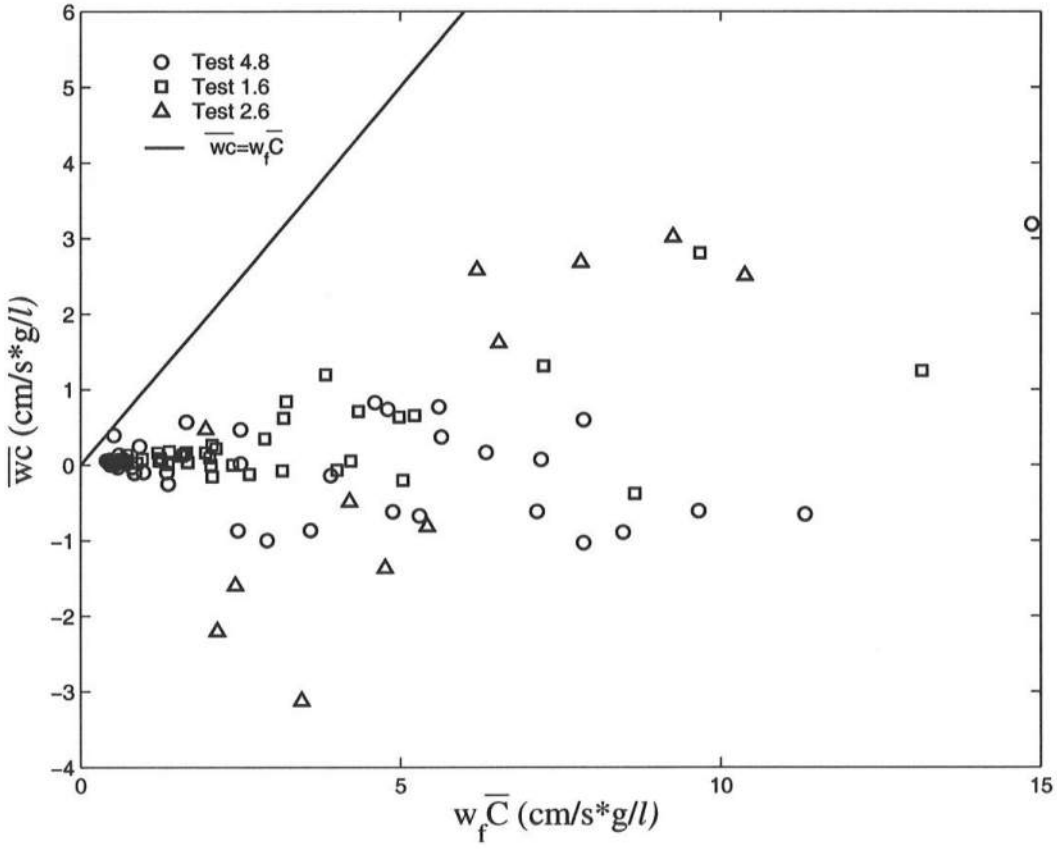

Figure 3.9: Measured $\overline{wc}$ in comparison with $w_f\overline{C}$ for three tests

where A is the constant of integration with respect to z. For the case of horizontal uniformity, $A = 0$ may be assumed because equation (3.16) must be satisfied in the region of negligible suspended sediment.

Equation (3.14) is evaluated using the measured time series of $W = (\overline{W} + w)$ and $C = (\overline{C} + c)$ at each elevation z_m. The measured $\overline{wc}$ does not increase with the increase of $w_f\overline{C}$ and remains roughly zero as shown in Figure 3.9 probably because the measured vertical velocity is not the fluid velocity as discussed in relation to equation (3.4). Consequently, the vertical distribution of $\overline{C}$ is examined using the conventional approach based on $\overline{cw} = (-\epsilon_v \partial\overline{C}/\partial z)$ in equation (3.14) [Nielsen,

1992]. The vertical mixing coefficient ϵ_v includes the effects of the wave-induced and turbulent velocities. The assumption of constant ϵ_v results in

$$\overline{C} = \overline{C_b} exp(-z_m/\ell_C) \quad ; \quad \ell_c = \epsilon_v/w_f \tag{3.17}$$

where $\overline{C_b}$ is the sediment concentration extrapolated to the bottom $z_m = 0$, and ℓ_C is the vertical length scale of $\overline{C}$. The exponential distribution of $\overline{C}$ has been shown to represent the measured concentration profiles in surf zones [e.g., Peters and Dette, 1999] and over rippled beds in a water tunnel [Ribberink and Al-Salem, 1994]. On the other hand, the assumption of $\epsilon_v = z_m \upsilon_C$ with υ_C being the velocity scale of ϵ_v yields

$$\overline{C} = \overline{C_a}(z_a/z_m)^n \quad ; \quad n = w_f/\upsilon_C \tag{3.18}$$

where $\overline{C_a}$ is the reference concentration at $z_m = z_a$ and the reference elevation z_a is taken as $z_a = 1$ cm which was the lowest elevation of the concentration measurements in Figure 3.1. The distribution of $\overline{C}$ in power form has been shown to represent the measured concentration profiles in sheet flow in a water tunnel [Ribberink and Al-Salem,1994].

The measured distribution of $\overline{C}(z_m)$ are fitted to the exponential and power-form distributions given by equations (3.17) and (3.18) as shown in Figure 3.10 and 3.11 where $\overline{C_b}, \ell_C, \overline{C_a}$ and n are fitted at each line. Both distributions represent the measured profiles fairly well except for lines 4.8A and 4.8B. For the present data, ℓ_C and n are related empirically as $n \simeq 0.2\overline{h}/\ell_C$ with $CC = 0.97$ for the range of $\overline{h}/\ell_C = 1.3 - 8.3$ as depicted in Figure 3.12. The parameter n is the ratio between the sediment fall velocity w_f and the velocity scale υ_C which may be related to the turbulent velocity u_0' in equation (3.10). The correlation between n and w_f/u_0' turns out to improve when $u_0' - w_f$ is used instead of u_0' to account for the initiation of sediment suspension [e.g., Lee et al., 2004]. As depicted in Figure 3.13, this regression analysis yields $n \simeq 0.8w_f/(u_0' - w_f)$ with $CC = 0.75$ for $w_f = 2.0$

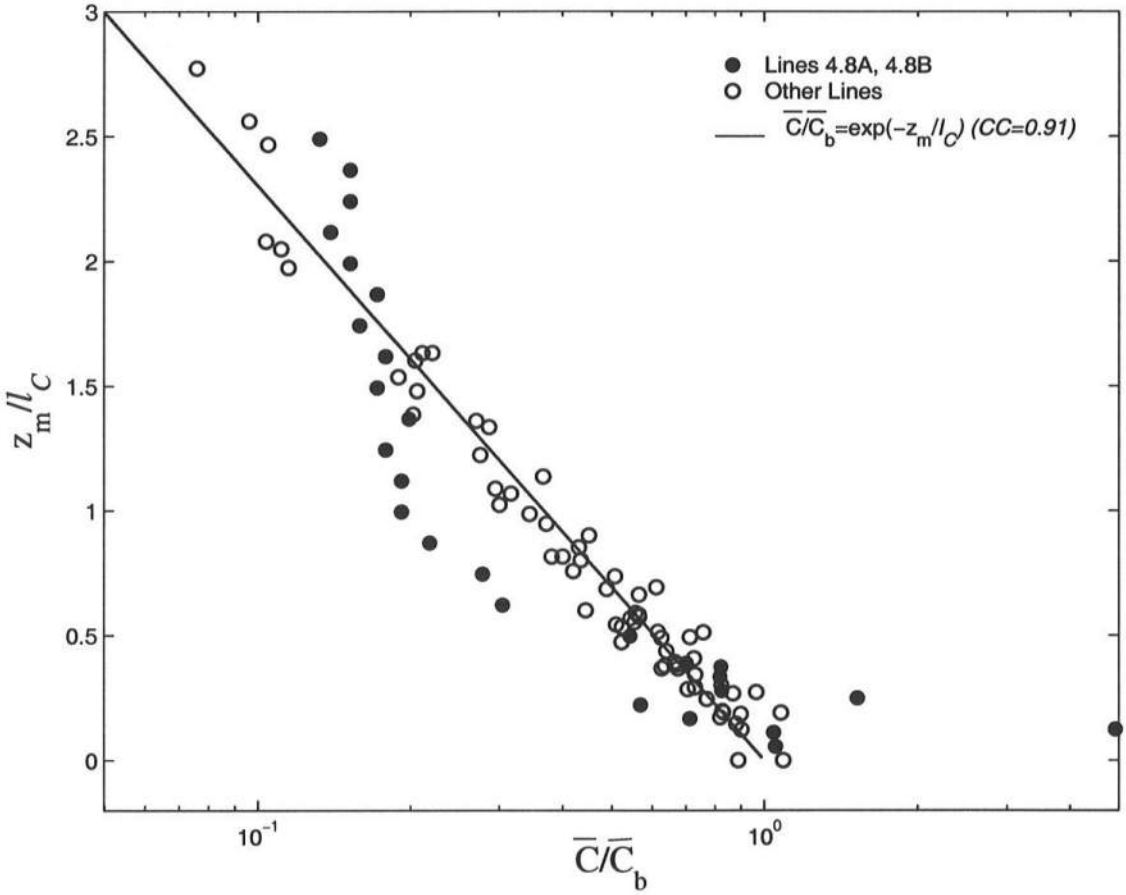

Figure 3.10: Vertical distribution of mean concentration $\overline{C}$ expressed as $\overline{C_b} exp(-z_m/\ell_C)$ at each line where the exponential distribution did not fit well at lines 4.8A and 4.8B.

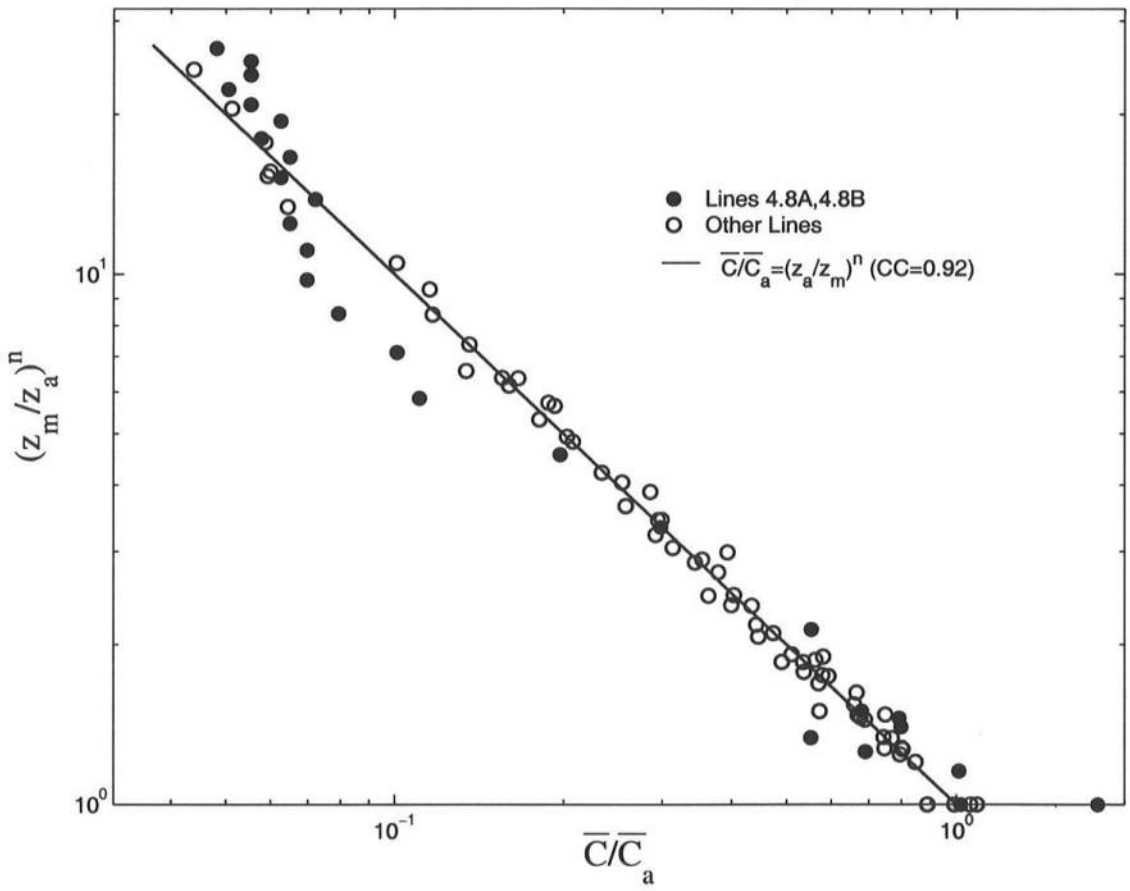

Figure 3.11: Vertical distribution of mean concentration $\overline{C}$ expressed as $\overline{C_a}(z_a/z_m)^n$ with $z_a = 1$ cm at each line where the distribution in power-form did not fit well at lines 4.8A and 4.8B

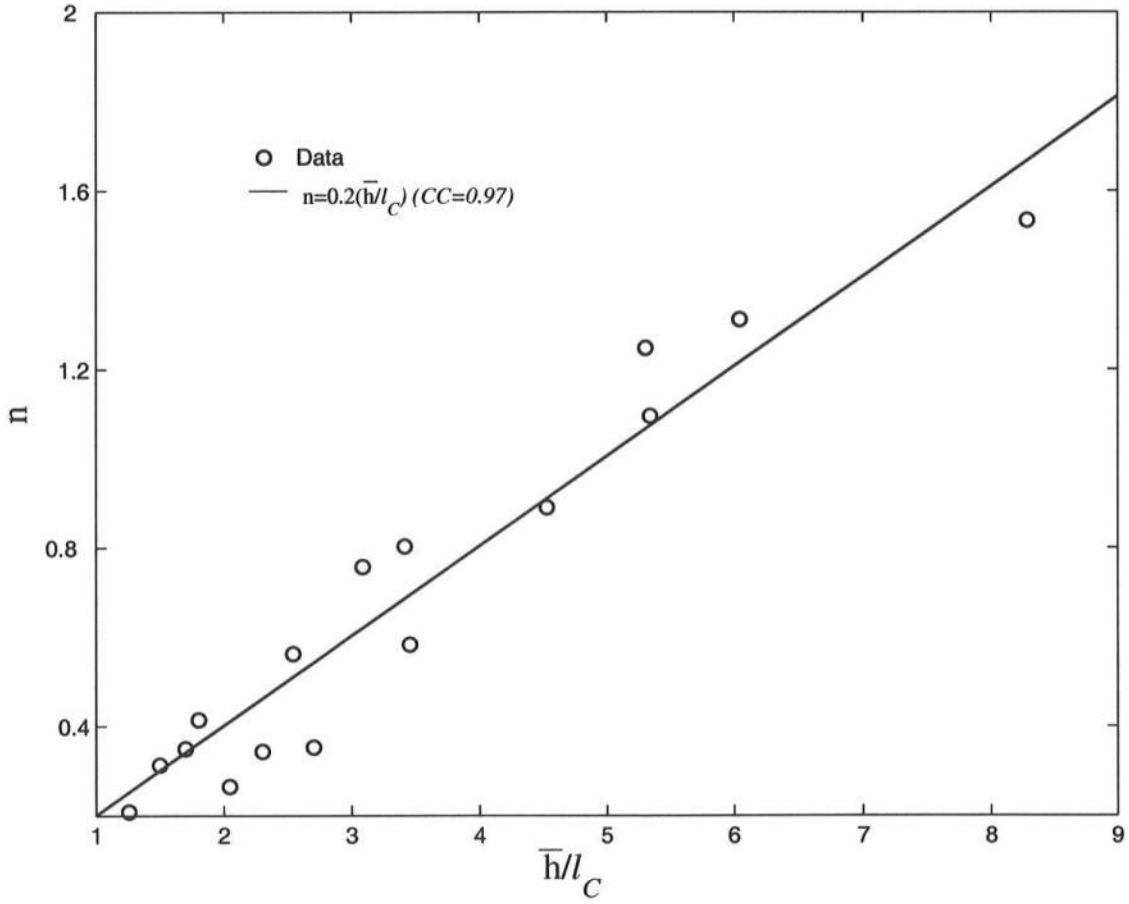

Figure 3.12: Parameter n as a function of $\overline{h}/\ell_C$ at each line for three tests

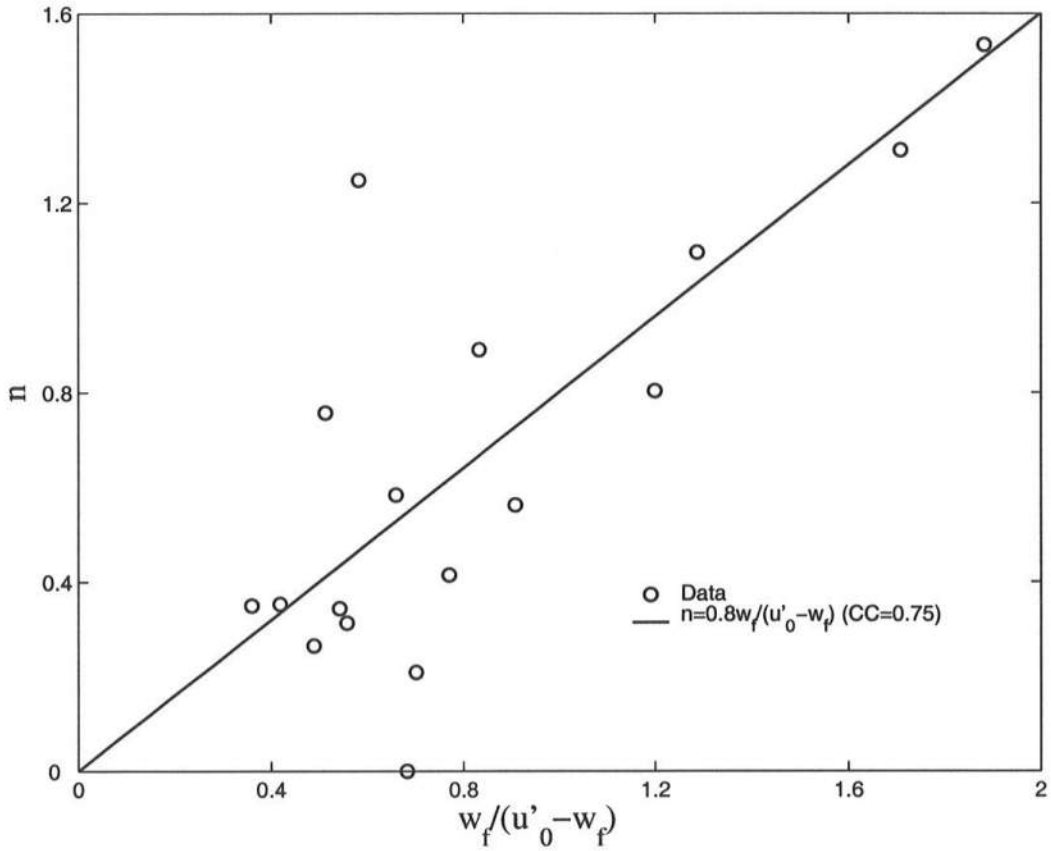

Figure 3.13: Parameter n as a function of $w_f/(u_0^{'} - w_f)$ at each line for three tests

cm/s and $u_0^{'} = 3.1 - 7.6$ cm/s. Equating the two empirical equations for n above, $(\ell_C/\overline{h}) \simeq 0.25(u_0^{'}/w_f - 1)$ with $CC = 0.49$ as shown in the top panel of Figure 3.14. Alternatively, ℓ_C may be expressed simply as $\ell_C \simeq 2\sigma_\eta$ with $CC = 0.55$ as shown in the bottom panel of Figure 3.14. In short, it is difficult to estimate ℓ_C and n accurately.

As for $\overline{C_b}$ and $\overline{C_a}$, Dunkley et al. [1999] showed that empirical formulas could predict only the order of magnitude of the reference concentration under breaking waves. It is noted that upward the sediment flux $\overline{cw}$ may alternatively be predicted but it is equal to $w_f\overline{C}$ in equation (3.14) for the case of horizontal uniformity. The

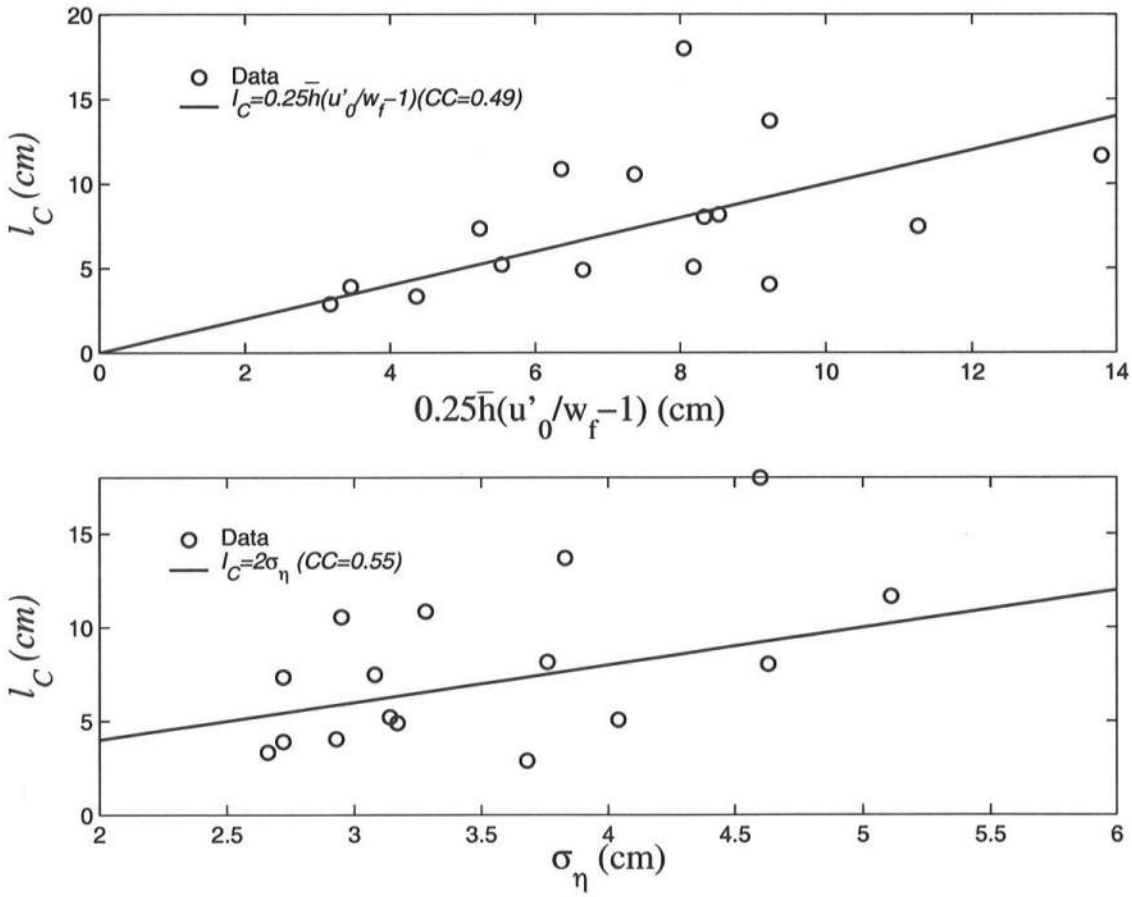

Figure 3.14: Vertical length scale ℓ_C as a function of $0.25\overline{h}(u_0'/w_f - 1)$ (top) and σ_η (bottom)

time-averaged suspended sediment volume $\overline{V}$ per unit horizontal area is used and predicted in the following analysis of suspended sediment transport. The value of $\overline{V}$ at each line is obtained by integrating equation (3.17) and (3.18) from $z_m = 0$ or z_a to $z_m = \overline{h}$ where (3.18) cannot be extrapolated to $z_m = 0$. The integration yields

$$\overline{V_b} = \overline{C_b}\ell_C \left[1 - exp(-\frac{\overline{h}}{\ell_C})\right] \quad ; \quad \overline{V_a} = \frac{\overline{C_a} z_a}{1-n}\left[\left(\frac{\overline{h}}{z_a}\right)^{1-n} - 1\right] \tag{3.19}$$

where $\overline{V_b}$ and $\overline{V_a}$ are the values of $\overline{V}$ based on the exponential and power-form distributions and are of the order of 0.01 cm as shown in section 3.4. The difference between $\overline{V_b}$ and $\overline{V_a}$ is less than 17%.

The standard deviation of σ_C of the sediment concentration is related to the mean concentration $\overline{C}$ in view of equation (3.16) with $A = 0$ where $\overline{c^2} = \sigma_C^2$. The measured values of $\alpha = \sigma_C/\overline{C}$ at each line are approximately constant as shown in Figure 3.15 where $< \alpha >$ is the average value at each line. The differences between α and $< \alpha >$ are less than about 20% except for lines 4.8A, 1.6A and 2.6A of no or infrequent wave breaking. If $\alpha = \sigma_C/\overline{C}$ is constant at each line, equation (3.16) requires that $\overline{wc^2}/(w_f\sigma_C^2) = (1 - \alpha^{-2})$. This requirement could not be examined because of the uncertainty of the measured w. To simplify the following data analysis, the average value $< \alpha >$ without the brackets is used with the assumption of constant α at each line. The values of α at the different lines are empirically related to the Dean number D_n defined here as $D_n = \sigma_\eta/(w_f T_p)$, which has been shown to be an important parameter for suspended sediment transport in surf zones [e.g., Dalrymple, 1992; Kobayashi and Johnson, 2001]. The value of $\alpha = \sigma_C/\overline{C}$ is expected to decrease with the increase of D_n which is the ratio between the sediment settling time σ_η/w_f and the wave period T_p. As shown in Figure 3.16, for the present experiment with $D_n = 0.28 - 1.15$ and $\alpha = 0.47 - 1.81$, $\alpha^{-1} \simeq (0.83D_n + 0.49)$ with $CC = 0.55$.

The measured correlation coefficient γ_{UC} between U and C decreases upward gradually because the concentration C of the sediment suspended from the bottom

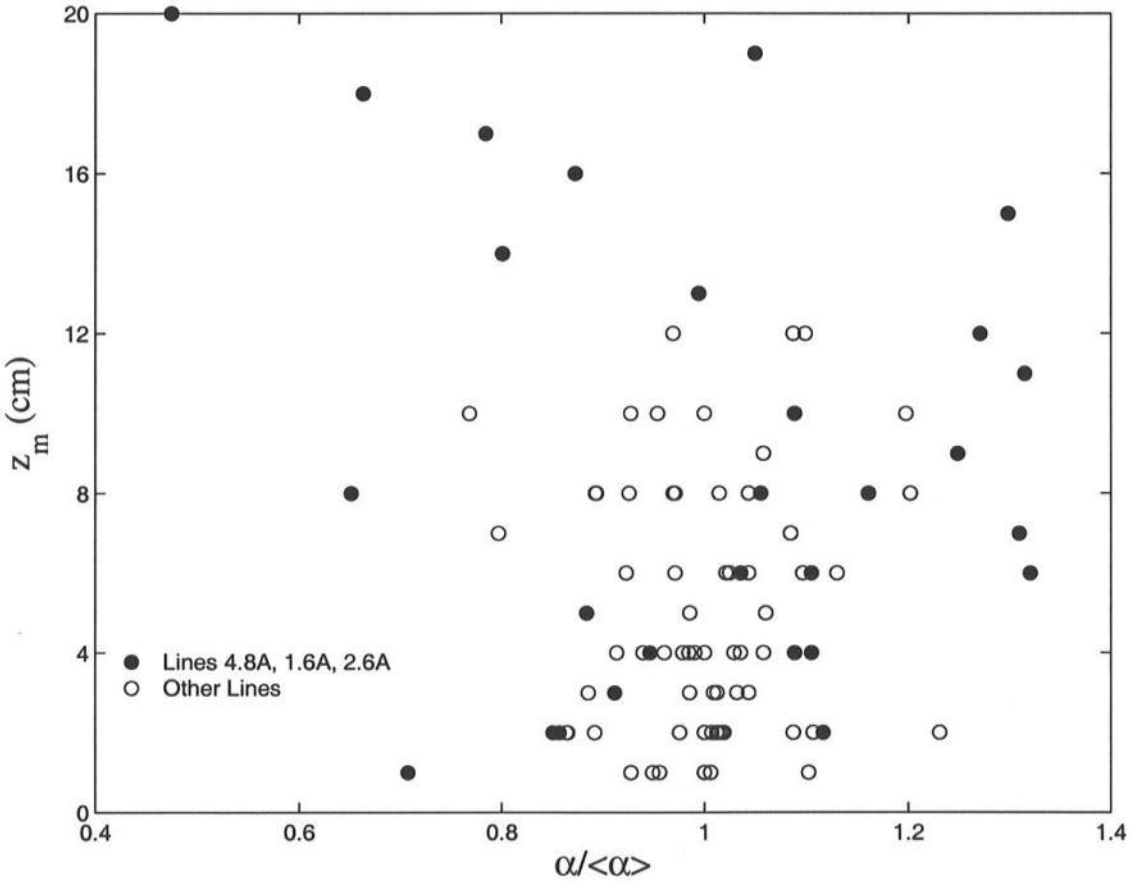

Figure 3.15: Vertical variation of ratio $\alpha = \sigma_C/\overline{C}$ normalized by the vertically-averaged value $< \alpha >$ at each line where the ratio varied more at lines 4.8A, 1.6A and 2.6A

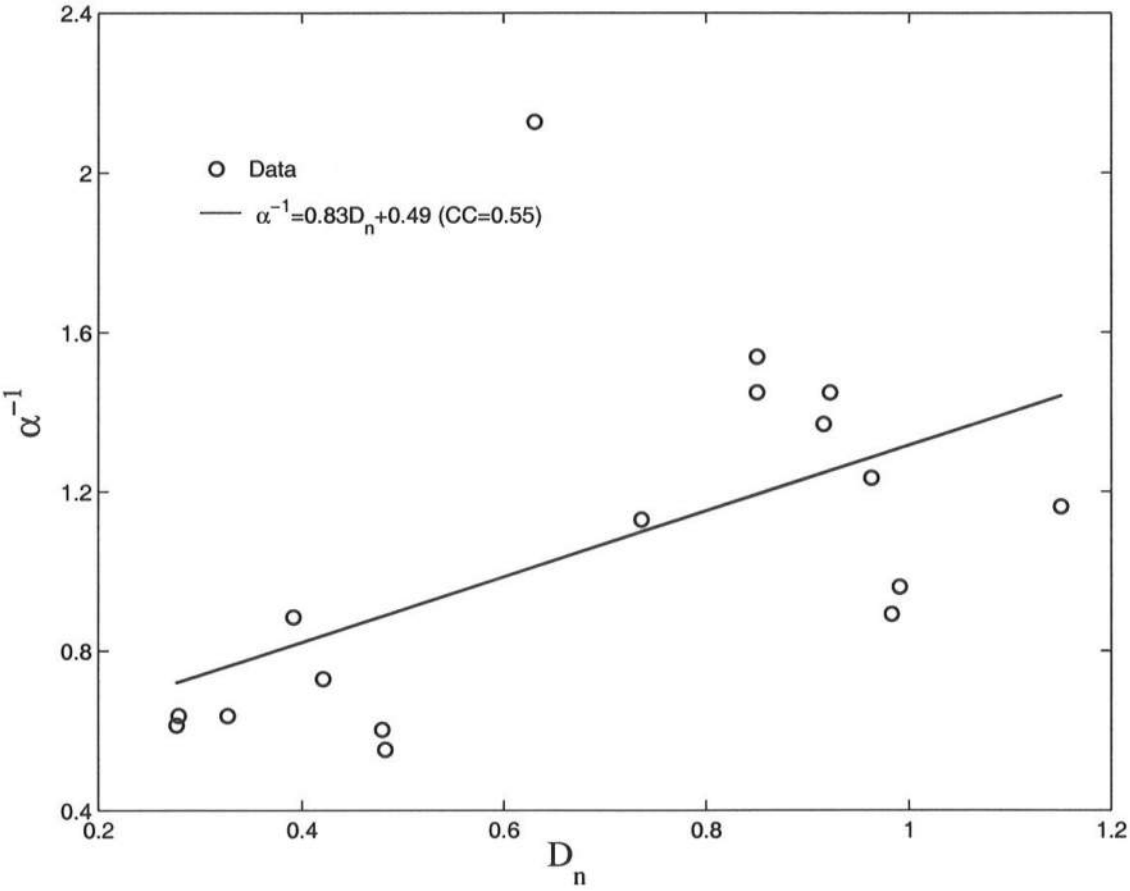

Figure 3.16: Measured $\alpha = \sigma_C/\overline{C}$ as a function of Dean number expressed as $\alpha^{-1} = 0.83D_n + 0.49$

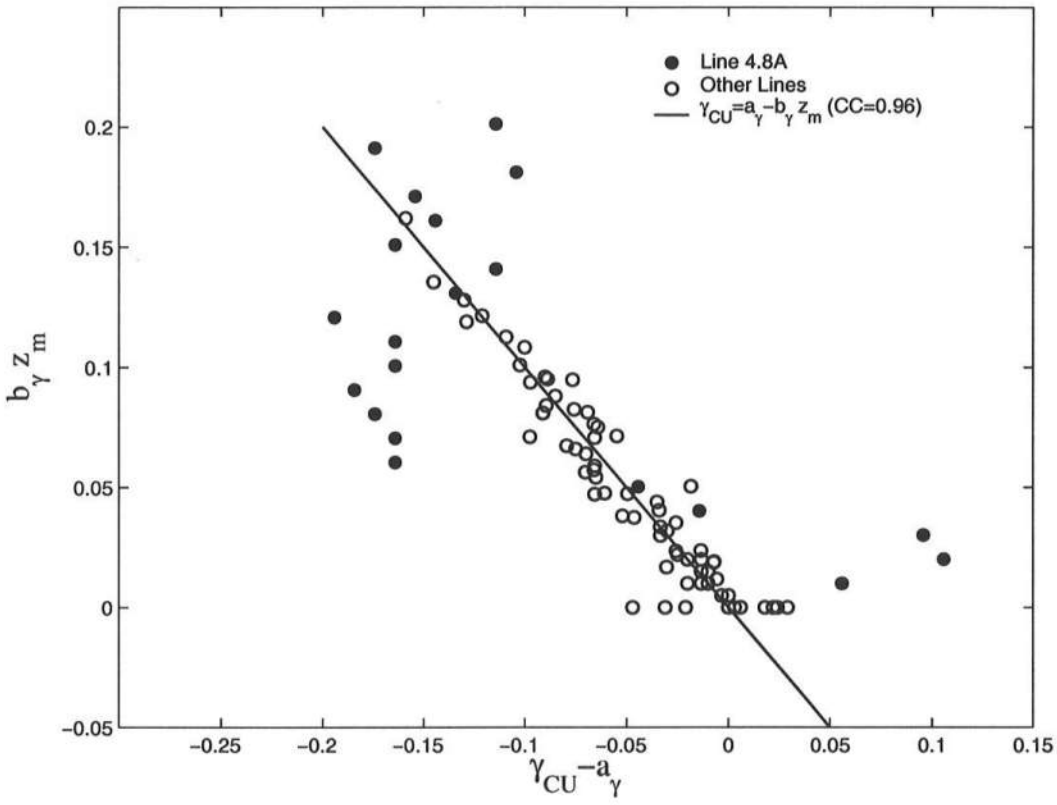

Figure 3.17: Vertical distribution of correlation coefficient γ_{UC} expressed as $\gamma_{UC} = (a_\gamma - b_\gamma z_m)$ at each line where the linear distribution did not fit well at line 4.8A

becomes less correlated with the fluid velocity U with the increase of the vertical distance z_m. The measured values of γ_{UC} at each line are expressed as

$$\gamma_{UC} = a_\gamma - b_\gamma z_m \tag{3.20}$$

where a_γ is the extrapolated value of γ_{UC} at $z_m = 0$ and b_γ is the inverse of the length scale associated with the upward decrease of γ_{UC} at each line. Figure 3.17 shows the measured values of $(\gamma_{UC} - a_\gamma)$ plotted as a function of $b_\gamma z_m$ for all the lines where $a_\gamma = 0.09 - 0.28$ except for $a_\gamma = 0$ at line 1.6D above the bar trough and ${b_\gamma}^{-1}$ is of the order of 100 cm. The measured upward decrease of γ_{UC} is well represented

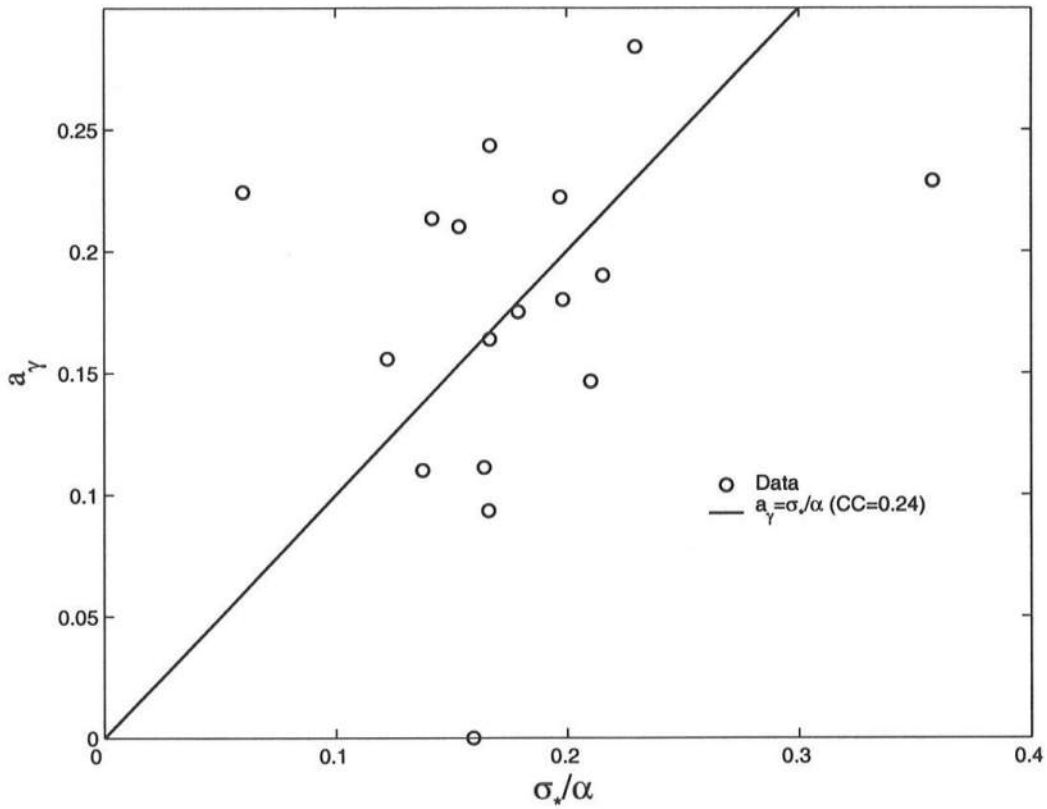

Figure 3.18: Extrapolated correlation coefficient a_γ expressed as $a_\gamma = \sigma_*/\alpha$

by equation (3.20) except for line 4.8A of no wave breaking. The fitted a_γ at each line is related to the measured values of $\sigma_* = \sigma_\eta/\overline{h}$ and α at the same line for the convenience of the subsequent sediment transport analysis. The fitted values of a_γ are of the order of σ_*/α where $a_\gamma \simeq \sigma_*/\alpha$ with $CC = 0.24$ for $\sigma_* = 0.11 - 0.29$ and $\sigma_*/\alpha = 0.06 - 0.36$ as shown in Figure 3.18. The value of CC is low partly because of the narrow ranges of a_γ and σ_*/α. Plant et al. [2001] observed the increase of γ_{UC} with the increase of σ_* for $\sigma_* < 0.09$ on a natural beach. On the other hand, the fitted values of a_γ/b_γ are of the order of the mean depth $\overline{h} = 11.1 - 42.9$ cm at the lines of the velocity and concentration measurements as shown in Figure 3.19.

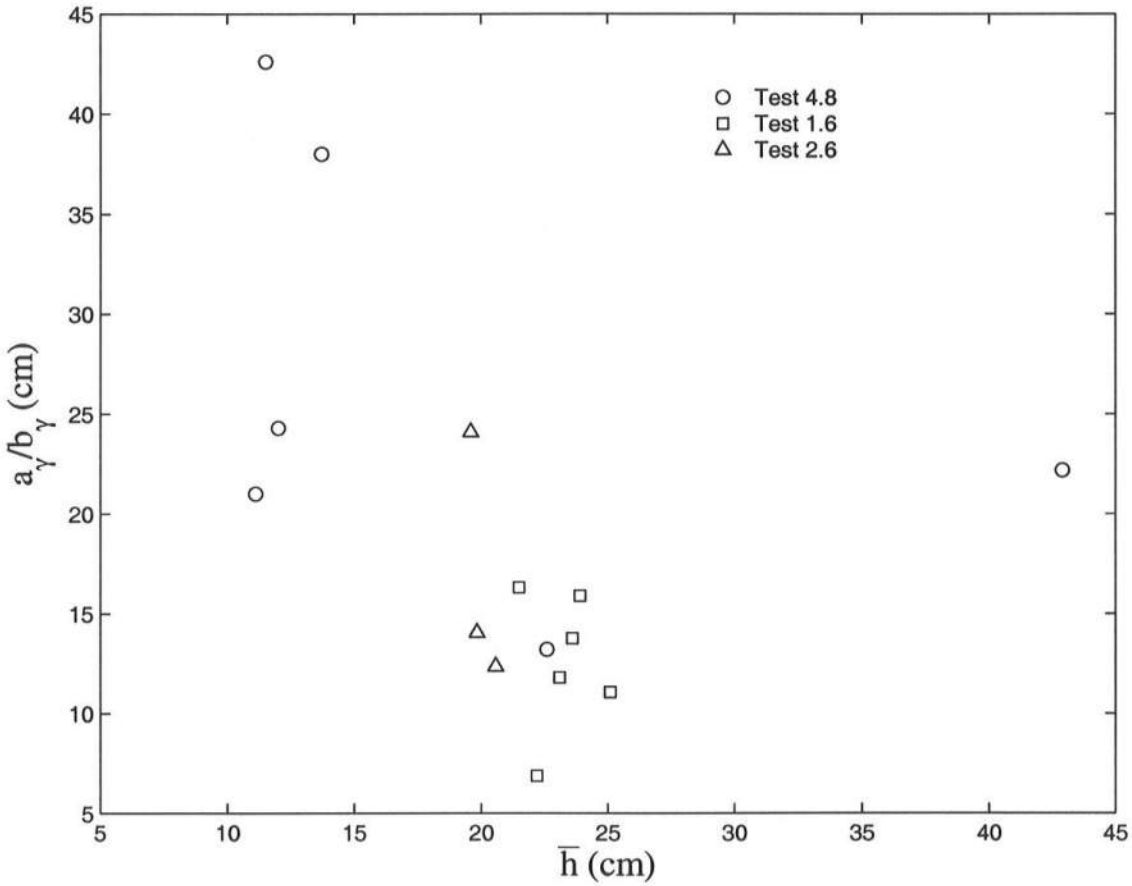

Figure 3.19: Ratio between a_γ and b_γ in comparison with mean water depth $\overline{h}$

3.4 Cross-Shore Suspended Sediment Transport

The cross-shore suspended sediment transport is analyzed using $\overline{UC} = (\overline{U}\overline{C} + \overline{uc})$ with $\overline{uc} = \sigma_U \sigma_C \gamma_{UC}$ from equation (3.5). The offshore suspended sediment transport rate q_{off} due to the negative mean velocity $\overline{U}$ is calculated as

$$q_{off} = \int_{z_0}^{h_0} (-\overline{U})\overline{C} dz_m \tag{3.21}$$

where $\overline{U}$ is given by equation (3.6) and $\overline{U} < 0$ for $z_m < h_0$ as explained in relation to equation (3.7), and the mean concentration $\overline{C}$ is expressed by equation (3.17) with the lower limit $z_0 = 0$ or equation (3.18) with $z_0 = z_a = 1$ cm as explained in relation to equation (3.19). Equation (3.21) can be integrated analytically.

To estimate the onshore suspended sediment transport rate q_{on}, use is made of $\overline{cu} = \alpha \sigma_U \gamma_{UC} \overline{C}$ where α and σ_U are the averaged values at each line. The offshore volume flux q_0 given by equation (3.7) requires the same onshore volume flux above $z_m = h_0$ in this two-dimensional experiment. The onshore sediment flux above $z_m = h_0$ may be estimated as $q_0 \overline{C_h}$ where $\overline{C_h} = \overline{C}$ at $z_m = \overline{h}$. As a result, q_{on} is calculated as

$$q_{on} = \alpha \sigma_U \int_{z_0}^{h_0} \gamma_{CU} \overline{C} dz_m + q_0 \overline{C_h} \tag{3.22}$$

where γ_{UC} is given by equation (3.20) and $\overline{C}$ is expressed by equation (3.17) with $z_0 = 0$ or (3.18) with $z_0 = z_a$. Equation (3.22) can be integrated analytically. The term $q_0 \overline{C_h}$ turns out to be important in the breaker zone where the extrapolated concentration $\overline{C_h}$ is not negligible.

Figure 3.20 shows that the estimated values of q_{off} and q_{on} using the exponential and power-form distributions of $\overline{C}$ for tests 4.8, 1.6 and 2.6. The average difference between the two estimates using equations (3.17) and (3.18) is approximately 10 and 23% for q_{off} and q_{on} where q_{on} is more uncertain because of the uncertainty of the extrapolated value of $\overline{C_h}$ at the mean water level. For both distributions, $q_{on} > q_{off}$ for test 4.8 but $q_{on} < q_{off}$ for test 1.6, whereas for test 2.6,

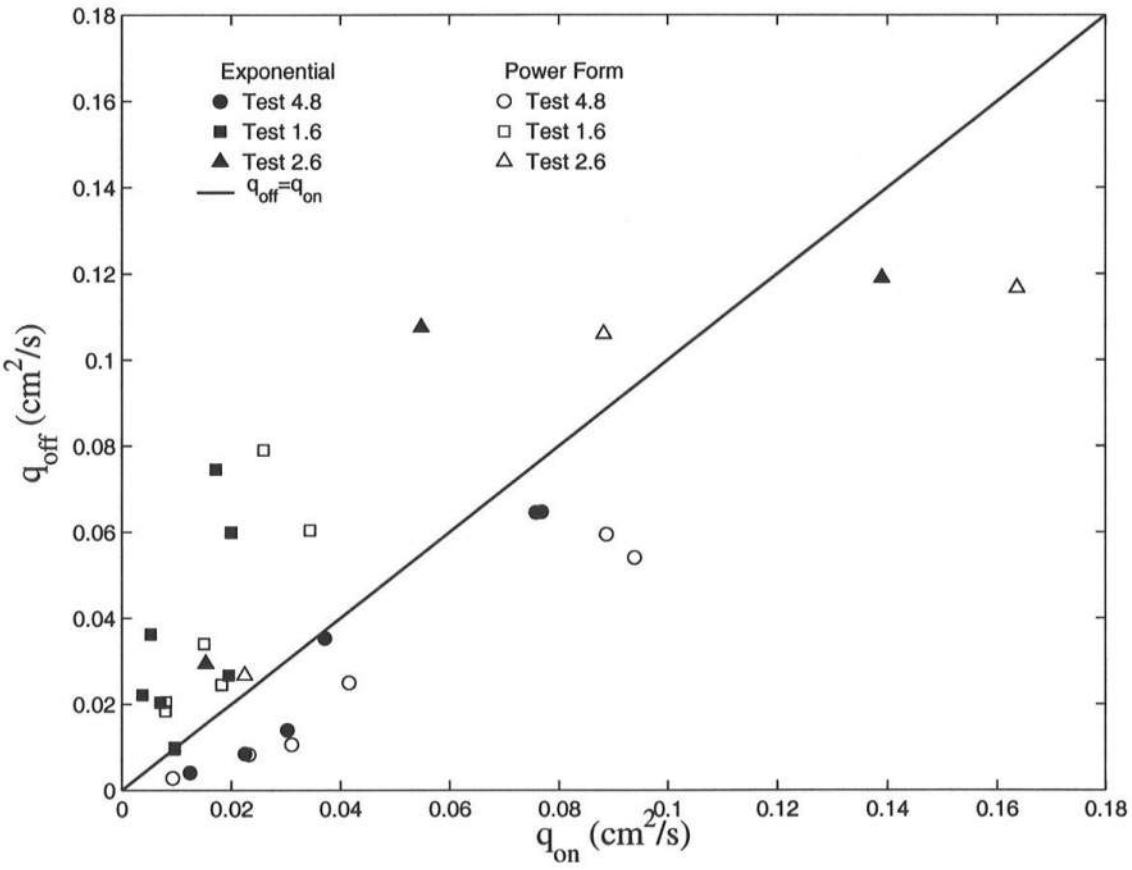

Figure 3.20: Estimated onshore and offshore suspended sand transport rates q_{on} and q_{off} using the exponential and power-form distributions of $\overline{C}$ at each line

$q_{on} > q_{off}$ at line 2.6A but $q_{on} < q_{off}$ at lines 2.6B and 2.6C. Since the net cross-shore sediment transport rate is zero on the equilibrium beach in Figure 3.1, the difference $(q_{on} - q_{off})$ may be regarded as the offshore bed load transport rate in the region of $z_m < z_a = 1$ cm for the power-form distribution or the transport rate which is not accounted for in the exponential distribution extrapolated to $z_m = 0$. The analysis of the bed load transport rate is beyond the scope of this study. It is noted that the bed load formula of Meyer - Peter and Mueller may be limited to the median sand diameter $d_{50} \geq 0.2$ mm [Ribberink, 1998]. For the present experiment, $d_{50} = 0.18$ mm and the bed load sediment did not move in a layer under breaking waves even in the absence of ripples.

Equations (3.21) and (3.22) are not convenient for the prediction of q_{off} and q_{on}. If $(-\overline{U})$ in equation (3.21) is approximated by the averaged offshore mean velocity $\overline{U_0}$ given by the equation (3.7), $q_{off} \simeq \overline{V}\ \overline{U_0}$ where $\overline{V}$ is the suspended sediment volume per unit area given by equation (3.19). If γ_{UC} in equation (3.22) is approximated by a_γ with $\gamma_{UC} \leq a_\gamma$ in equation (3.20) and $q_0\overline{C_h}$ is neglected for simplicity, $q_{on} \simeq \alpha a_\gamma \sigma_U \overline{V}$, which is simplified as $q_{on} \simeq \sigma_* \sigma_U \overline{V}$ using $a_\gamma \simeq \sigma_*/\alpha$ as discussed in relation to equation(3.20). These simplified equations are evaluated in Figure 3.21 and 3.22 for the exponential and power-form distributions of $\overline{C}$. The fitted equations in these figures are expressed as

$$q_{off} = 0.9\overline{V}\ \overline{U_0} \qquad ; \qquad q_{on} = 0.8\sigma_* \sigma_U \overline{V} \tag{3.23}$$

It is noted that the regression analysis between q_{on} and $(\alpha a_\gamma \sigma_U \overline{V})$ does not improve the agreement as shown in Figure 3.23. Equation (3.23) involves $\overline{V}, \overline{U_0}, \sigma_* = \sigma_\eta/\overline{h}$ and σ_U which may be predicted by a cross-shore one-dimensional model.

Finally, Table 3.6 summarizes the values of $\sigma_*, \overline{U_0}, \sigma_U, \overline{V}, q_{off}$ and q_{on} at each line used to plot Figures 3.20 - 3.22.

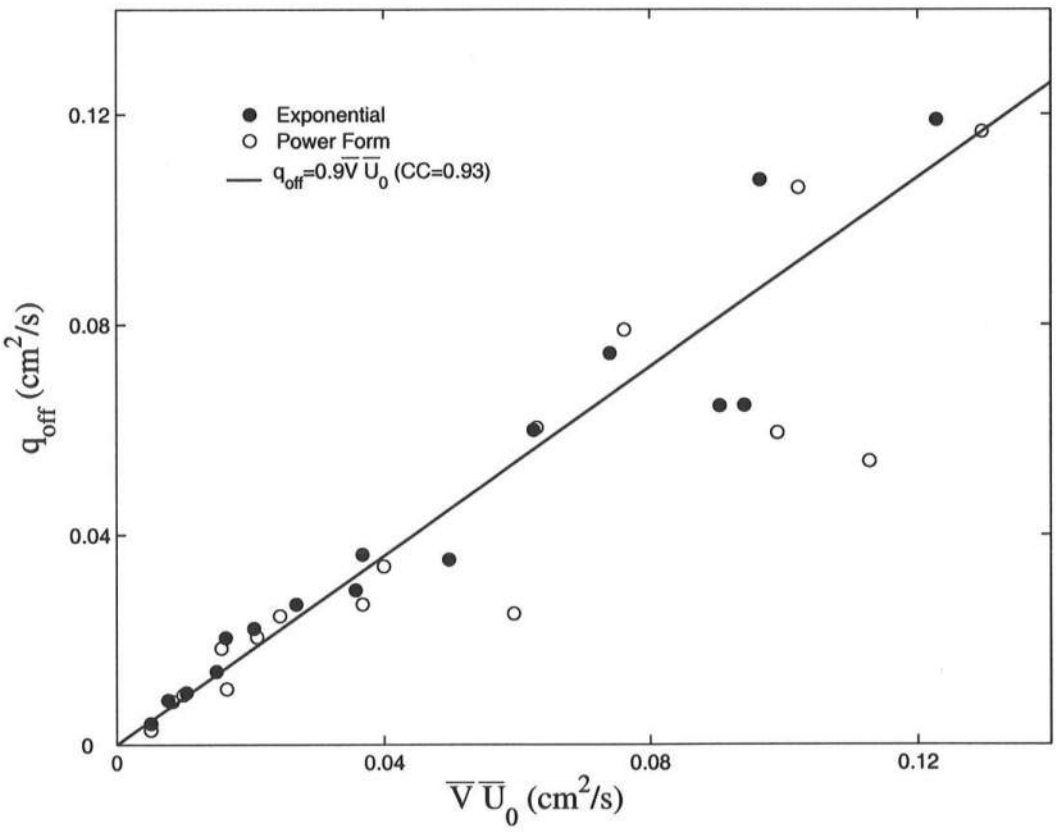

Figure 3.21: Offshore transport rate q_{off} in comparison with offshore return current $\overline{U_0}$ multiplied by suspended sediment volume $\overline{V}$ per unit area

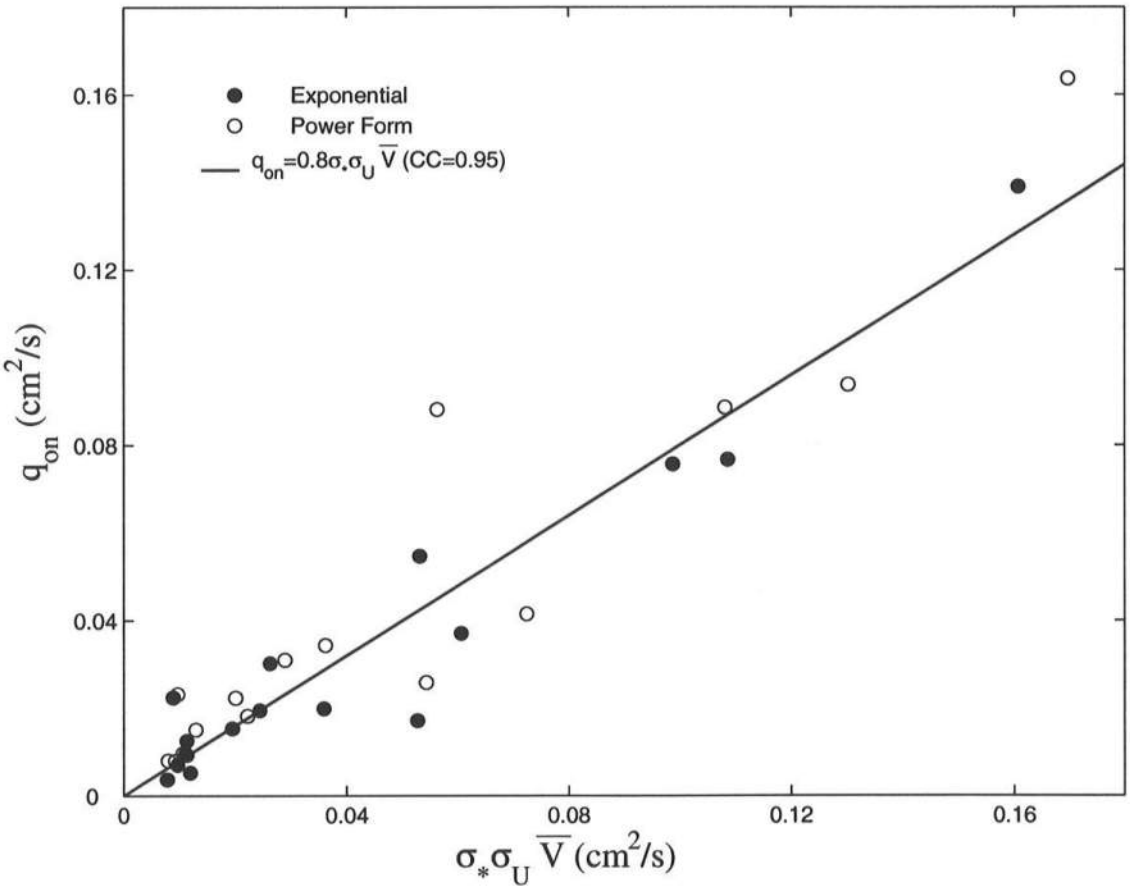

Figure 3.22: Onshore transport rate q_{on} in comparison with $\sigma_*\sigma_U\overline{V}$

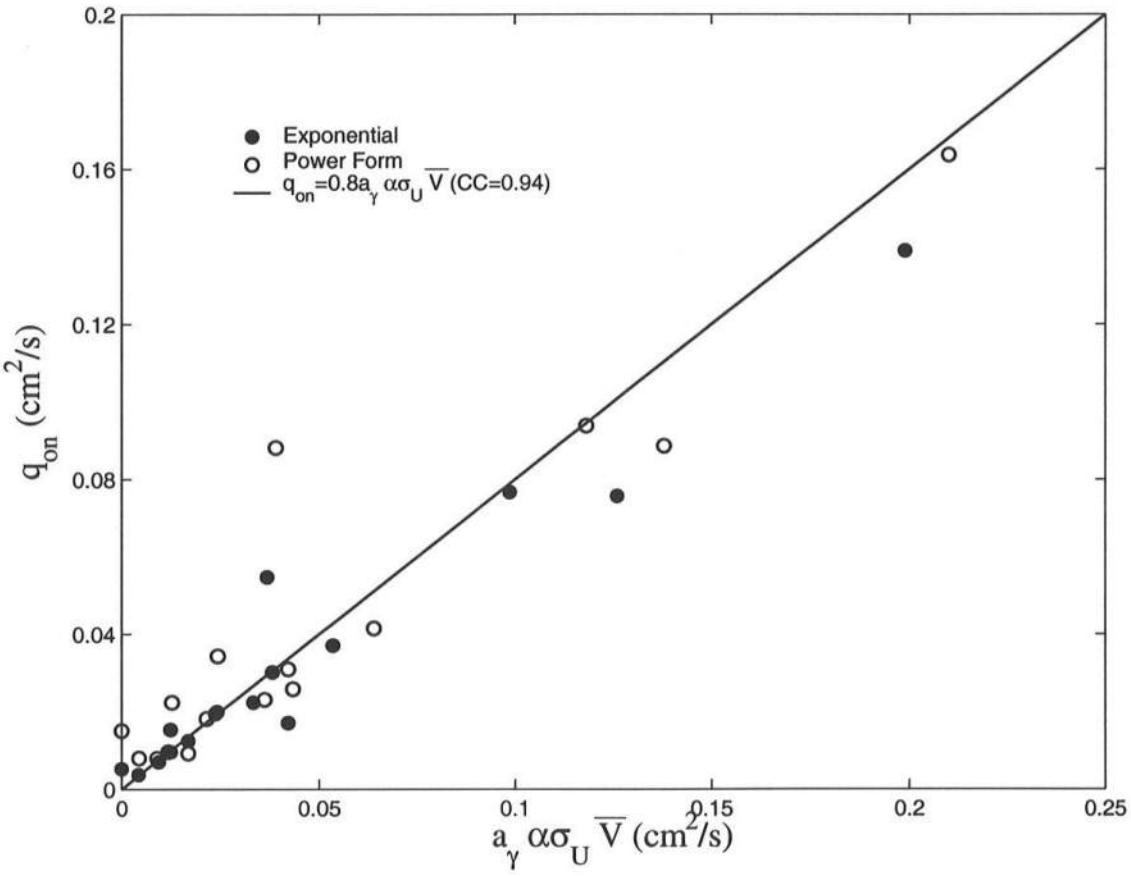

Figure 3.23: Onshore transport rate q_{on} in comparison with $a_\gamma \alpha \sigma_U \overline{V}$

Table 3.6: Quantities involved in cross-shore suspended sediment transport

Test	x (m)	σ_*	$\overline{U_0}$ (cm/s)	σ_U (cm/s)	Exponential			Power-form		
					$\overline{V}$ (cm)	q_{off} (cm^2/s)	q_{on} (cm^2/s)	$\overline{V}$ (cm)	q_{off} (cm^2/s)	q_{on} (cm^2/s)
	4.35	0.108	1.66	17.9	0.0046	0.0085	0.0224	0.0050	0.0083	0.0231
	6.05	0.203	5.35	28.8	0.0169	0.0646	0.0757	0.0185	0.0594	0.0887
	7.40	0.224	5.47	28.2	0.0172	0.0647	0.0768	0.0206	0.0541	0.0938
4.8	8.30	0.295	5.72	23.6	0.0087	0.0353	0.0371	0.0104	0.0250	0.0415
	9.30	0.262	3.82	25.7	0.0039	0.0140	0.0302	0.0043	0.0106	0.0310
	9.75	0.231	2.70	25.7	0.0019	0.0040	0.0125	0.0019	0.0028	0.0093
	9.95	0.241	3.00	26.8	0.0019	NR	0.0058	0.0019	NR	0.0168
	2.05	0.154	3.05	18.0	0.0088	0.0267	0.0195	0.0080	0.0301	0.0182
	2.35	0.143	4.38	21.8	0.0169	0.0746	0.0172	0.0174	0.0790	0.0259
	2.65	0.133	4.57	19.7	0.0137	0.0599	0.0200	0.0138	0.0604	0.0344
1.6	3.25	0.110	5.33	15.7	0.0069	0.0363	0.0053	0.0075	0.0340	0.0151
	3.95	0.108	4.56	16.1	0.0045	0.0221	0.0037	0.0046	0.0205	0.0080
	4.75	0.115	3.25	16.8	0.0050	0.0204	0.0070	0.0048	0.0184	0.0080
	5.75	0.136	2.26	17.7	0.0046	0.0100	0.0097	0.0044	0.0095	0.0097
	5.00	0.257	5.27	26.84	0.0233	0.1190	0.1390	0.0246	0.1167	0.1637
2.6	6.35	0.186	6.35	18.78	0.0152	0.1076	0.0548	0.0161	0.1061	0.0882
	7.60	0.168	5.33	17.30	0.0067	0.0295	0.0154	0.0069	0.0267	0.0224

Chapter 4

NUMERICAL MODEL AND COMPARISONS WITH DATA

4.1 Time-Averaged Numerical Model

The time-averaged model developed here is an extension of the Dutch models by Battjes and Stive [1985], Stive and DeVriend [1994], and Ruessink et al. [2001]. The major improvement is the extension of the model to the lower swash zone. The time-averaged cross-shore momentum and energy equations are expressed as

$$\frac{dS_{xx}}{dx} = \rho g \overline{h} \frac{d\overline{\eta}}{dx} - \tau_b \qquad ; \qquad \frac{dF}{dx} = -D_B - D_f \tag{4.1}$$

where x is the cross-shore coordinate, positive onshore, S_{xx} is the cross-shore radiation stress, ρ is the fluid density, g is the gravitational acceleration, $\overline{h}$ is the mean water depth given by $\overline{h} = (\overline{\eta} - z_b)$ with z_b being the bottom elevation, $\overline{\eta}$ is the mean free surface elevation, τ_b is the bottom shear stress, F is the wave energy flux, and D_B and D_f are the energy dissipation rates due to wave breaking and bottom friction, respectively. The terms τ_b and D_f are normally neglected but included here because of the importance of bottom friction for sediment transport. Linear wave theory for onshore progressive waves is used to estimate S_{xx} and F

$$S_{xx} = \rho g \sigma_\eta^2 \left(\frac{2C_g}{C_p} - \frac{1}{2} \right) + \rho C_p q_r \qquad ; \qquad F = \rho g C_g \sigma_\eta^2 \tag{4.2}$$

where C_g and C_p are the group velocity and phase velocity in the mean water depth $\overline{h}$ corresponding to the spectral peak period T_p, and q_r is the volume flux due to the roller on the steep front of a breaking wave.

The roller effect has been represented by its area or energy [Svendsen, 1984] but the roller volume flux is used here because the roller effect is the most apparent in the increase of undertow current. Furthermore, irregular plunging waves in test 4.8 did not exhibit identifiable roller areas. The term $\rho C_p q_r$ in S_{xx} is the roller momentum flux due to the roller propagating with the speed of C_p and causes the landward shrift of $\overline{\eta}$ in the breaker zone. The roller effect is not included in F in the Dutch model [e.g., Ruessink et al., 2001] but is included in Svendsen et al. [2003] who related the roller area to the wave height squared. The two different approaches depend on the interpretation of F and D_B in the energy equation where F and D_B in equation (4.1) include the wave-related energy only. The practical reason of the adoption of the Dutch approach is that the energy equation without any roller predicts the cross-shore variations of $H_{rms} = \sqrt{8}\sigma_\eta$ well if the breake ratio parameter γ is calibrated as explained later. In the Dutch approach, the dissipated wave energy is converted to the roller energy which is assumed to be governed by [Stive and DeVriend, 1994]

$$\frac{d}{dx}\left(\rho C_p^2 q_r\right) = D_B - \rho g \beta_r q_r \tag{4.3}$$

where the roller dissipation rate, $\rho g \beta_r q_r$, is assumed to equal the rate of work to maintain the roller on the wave-front slope β_r of the order of 0.1 [Deigaard, 1993].

Linear shallow-water wave theory has been used to find the approximate local relationship between η and U [Guza and Thornton, 1980]. The standard deviation of U is estimated as

$$\sigma_U = \sigma_*(g\overline{h})^{0.5} \qquad ; \qquad \sigma_* = \sigma_\eta/\overline{h} \tag{4.4}$$

The depth-integrated continuity equation of water on the beach, which is assumed impermeable, is expressed as $(\sigma_\eta \sigma_U + \overline{U}\ \overline{h} + q_r) = 0$ where $\sigma_\eta \sigma_U$ is the onshore flux

due to linear shallow-water waves [Kobayashi et al., 1998] and $\overline{U}$ is regarded as the depth-averaged return current. Hence, $\overline{U}$ is estimated as

$$\overline{U} = -\sigma_*^2 (g\overline{h})^{0.5} - q_r/\overline{h} \tag{4.5}$$

The time-averaged bottom shear stress and dissipation rate are expressed as

$$\tau_b = \frac{1}{2}\rho f_b \overline{|U|U} \quad ; \quad D_f = \frac{1}{2}\rho f_b \overline{|U|U^2} \tag{4.6}$$

where f_b is the bottom friction factor. To express τ_b and D_f in terms of $\overline{U}$ and σ_U, the equivalency of the time and probabilistic averaging as well as the Gaussian distribution of U are assumed [Guza and Thornton, 1985; Kobayashi et al., 1998].

$$\tau_b = \frac{1}{2}\rho f_b \sigma_U^2 G_2(U_*) \quad ; \quad D_f = \frac{1}{2}\rho f_b \sigma_U^3 G_3(U_*) \quad ; \quad U_* = \frac{\overline{U}}{\sigma_U} \tag{4.7}$$

with

$$G_2(r) = (1+r^2) erf\left(\frac{r}{\sqrt{2}}\right) + \sqrt{\frac{2}{\pi}} r exp\left(-\frac{r^2}{2}\right) \tag{4.8}$$

$$G_3(r) = (3r+r^3) erf\left(\frac{r}{\sqrt{2}}\right) + \sqrt{\frac{2}{\pi}} (r^2+2) exp\left(-\frac{r^2}{2}\right) \tag{4.9}$$

where erf is the error function and r is an arbitrary variable with $r = U_*$ in equation (4.7). The functions G_2 and G_3 for the range $\mid r \mid < 1$ can be approximated as $G_2 \simeq 1.64r$ and $G_3 \simeq (1.6 + 2.6r^2)$.

Finally, the energy dissipation rate D_B due to wave breaking is estimated using the formula by Battjes and Stive [1985].

$$D_B = \frac{\rho g a Q H_B^2}{4T_p} \quad ; \quad \frac{Q-1}{lnQ} = \left(\frac{H_{rms}}{H_m}\right)^2 \quad ; \quad H_m = \frac{0.88}{k_p} tanh\left(\frac{\gamma k_p \overline{h}}{0.88}\right) \tag{4.10}$$

where a is the empirical coefficient suggested as $a = 1$; Q is the fraction of breaking waves with $Q = 0$ for no wave breaking and $Q = 1$ when all waves break; $H_B =$ wave height used to estimate D_B with $H_B = H_m$ in their formula; H_m is the local depth-limted wave height; and γ is the breaker ratio parameter with $H_m = \gamma\overline{h}$ in shallow water. The wave number k_p is given by $k_p = 2\pi/(C_p T_p)$. The requirement

of $0 \leq Q \leq 1$ implies $H_{rms} \leq H_m$ but H_{rms} becomes larger than H_m in very shallow water. When $H_{rms} > H_m$, use is made of $Q = 1$ and $H_B = H_{rms}$ instead of $H_B = H_m$.

The choice of $a = 1$ in equation (4.10) was based on the assumption of the energy dissipation of a bore distributed uniformly over one wavelength. This assumption may not be reasonable in the region where the energy dissipation is more concentrated locally. The coefficient a is hence taken as the ratio of the wavelength estimated as $T_p(gh)^{0.5}$ to the horizontal length scale $(b\overline{h}/S_b)$ with b being an empirical factor, imposed by the small depth $\overline{h}$ and the local bottom slope $S_b = dz_b/dx$

$$a = b^{-1} S_b T_p (g\overline{h})^{0.5} \geq 1 \tag{4.11}$$

where $a \geq 1$ is imposed so that $a = 1$ in the region of large $\overline{h}$ and small S_b. Use is made of $b = 3$, which was the value calibrated by Kobayashi et al. [2005] to increase D_B due to intense wave breaking on the steep slope of a submerged porous breakwater. The computed value of a increases rapidly from unity to about ten near the shoreline for the computed results presented in the following. It is noted that D_B could also be increased by increasing γ because $H_m = \gamma\overline{h}$ in shallow water where γ is observed to increase with the beach slope [Raubenheimer et al., 1996]. The increase of D_B due to the slope effect results in the increase of q_r in equation (4.3). To offset this increase, use is made of $\beta_\gamma = (0.1 + S_b) \geq 0.1$, which implies that the wave-front slope increases on the upward slope. In short, the slope effects on D_B and β_γ have been examined very little.

In the region of $H_{rms} > H_m$ and $Q = 1, \sigma_* = \sigma_\eta/\overline{h}$ in equation (4.4) and (4.5) becomes large and the computed absolute values of σ_U and U are too large and vary too rapidly with the mean depth $\overline{h}$. To remedy this shortcoming caused by the local use of linear shallow-water wave theory near the shoreline, use is made of $\sigma_* = (\sigma_{*c}\sigma_\eta/\overline{h})^{0.5}$ if $\sigma_* > \sigma_{*c} = \gamma/\sqrt{8}$ which corresponds to $H_{rms} = \gamma\overline{h}$. This empirical

correction reduces the dependency on the mean water depth $\overline{h}$. For example, $\sigma_U = (\sigma_{*c} g \sigma_\eta)^{0.5}$ if $\sigma_* > \sigma_{*c}$.

Equation (4.1) and (4.3) are solved using a finite difference method with constant grid spacing $\triangle x$ of the order of 1 cm here. The measured bottom elevation $z_b(x)$ is specified in the computation domain $x \geq 0$ where $x = 0$ at wave gauge 1. The measured values of $T_p, \overline{\eta}, H_{rms} = \sqrt{8}\sigma_\eta$ in Table 3.1 and $q_r = 0$ at wave gauge 1 located outside the surf zone are specified as the seaward boundary conditions. The landward-marching computation is continued until the computed value of $\overline{h}$ or σ_η becomes negative. This landward limit corresponds to the mean water depth $\overline{h}$ of the order of 0.1 cm in the present computation. No numerical difficulty is encountered near the shoreline after the introduction of the parameter a given by equation (4.11). The computation is made with and without the roller effect, corresponding to IROLL = 1 and 0. For the option of IROLL = 0, the roller volume flux $q_r = 0$ and equation (4.3) is not used. Reflected waves are neglected in the time-averaged model but an attempt is made to estimate the degree of wave reflection. The computed onshore energy flux F decreases landward due to wave breaking and bottom friction. The residual energy flux F_{sws} at the still water shoreline is assumed to be reflected and propagate seaward. This assumption neglects the fact that the landward-marching computation is made with no regard to wave reflection. The root-mean-square wave height $(H_{rms})_r$ due to the reflected wave energy flux is estimated as

$$(H_{rms})_r = [8F_{sws}/(\rho g C_g)]^{0.5} \tag{4.12}$$

where the group velocity C_g is assumed to be the same for the incident and reflected waves.

After the landward-marching computation, the suspended sediment volume $\overline{V}$ per unit area is estimated using the sediment suspension model by Kobayashi and Johnson [2001].

$$\overline{V} = \frac{e_B D_B + e_f D_f}{\rho g (s-1) w_f} \tag{4.13}$$

where s and w_f are the specific gravity and fall velocity of the sediment, and e_B and e_f are the suspension efficiencies for D_B and D_f, respectively. For the present experiment, $s = 2.6$ and $w_f = 2.0$ cm/s. Use is made of $e_B = 0.005$ and $e_f = 0.01$ calibrated by them to predict beach profile changes observed in large-scale laboratory experiments. Equation (4.13) is valid for the equilibrium beach on which the sediment suspension rate equals the sediment settling rate. Kobayashi and Johnson [2001] did not include the roller effect in their model. When the roller effect is included, D_B in equation (4.13) is replaced by $(\rho g \beta_\gamma q_r)$ in view of equation (4.3) because the latter represents the rate of the roller energy dissipation.

4.2 Comparisons with Free Surface Elevation Data

The breaker ratio parameter γ in equation (4.10) and the bottom friction factor f_b in equation (4.7) are varied to examine the sensitivity of the computed results to these parameters. The cross-shore variation of σ_η related to the wave energy equation is used to calibrate γ where $\gamma = 0.6, 0.7$ and 0.8 are tried. The increase of γ shifts the zone of wave breaking landward. The calibrated value is $\gamma = 0.6$ for tests 4.8 and 1.6 and $\gamma = 0.8$ for test 2.6. The value of $f_b = 0.015$ has been calibrated and used in the previous time-dependent computations for wave runup [Raubenheimer et al., 1995] and sand suspension [Kobayashi and Johnson, 2001; Kobayashi and Tega 2002]. The computed results by this time-averaged model are found to be insensitive to f_b and $f_b = 0.015$ is used here as well. Figure 4.1 - 4.3 show the measured and computed cross-shore variations of the mean free surface elevation $\overline{\eta}$ for tests 4.8, 1.6 and 2.6, respectively, where $q_r = 0$ in equations (4.2) and (4.4) for IROLL = 0. The roller represented by $q_r > 0$ delays the rise of $\overline{\eta}$ in the breaker zone and increases $\overline{\eta}$ near the still water shoreline. The computed rapid increase of $\overline{\eta}$ near the shoreline is consistent with the field data of Raubenheimer et al. [2001]. The roller effect does not necessarily improve the agreement for these three tests.

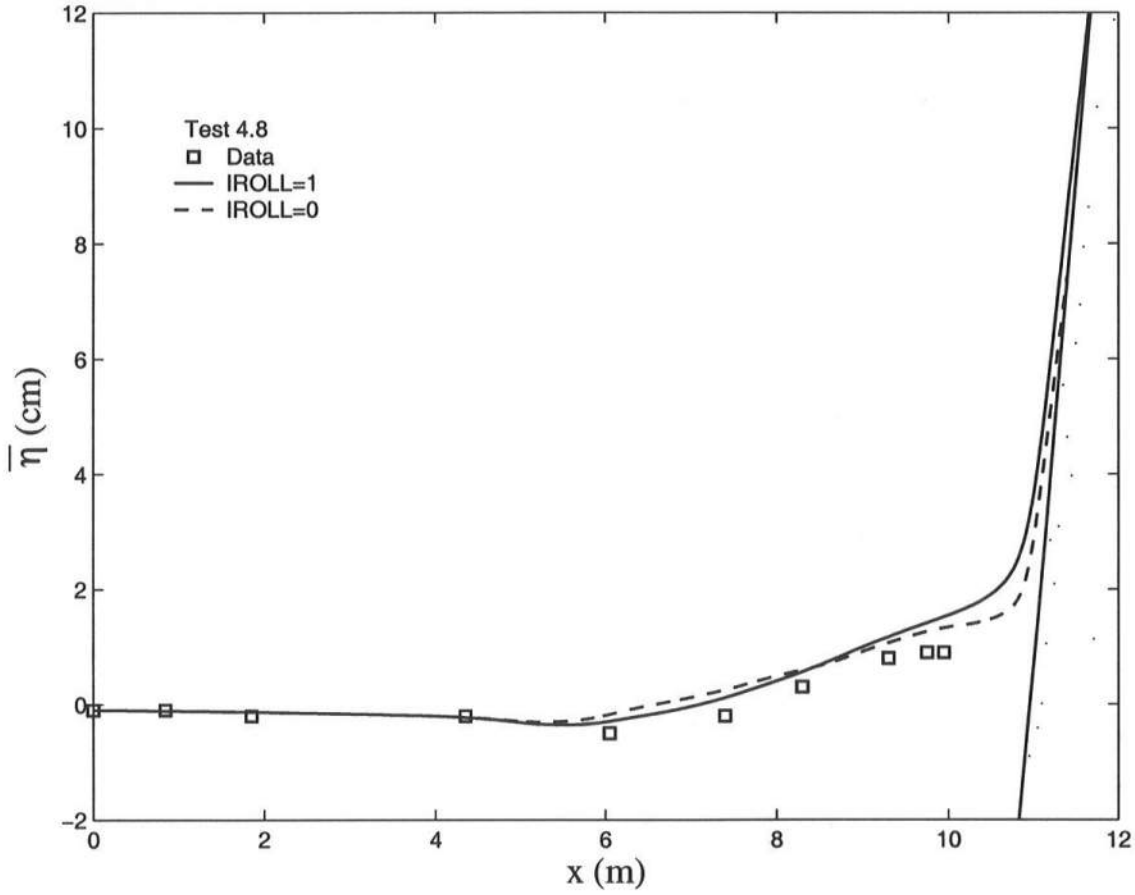

Figure 4.1: Measured and computed mean free surface elevation $\overline{\eta}$ for test 4.8 where IROLL = 1 and 0 indicate the computed results with and without the roller volume flux q_r

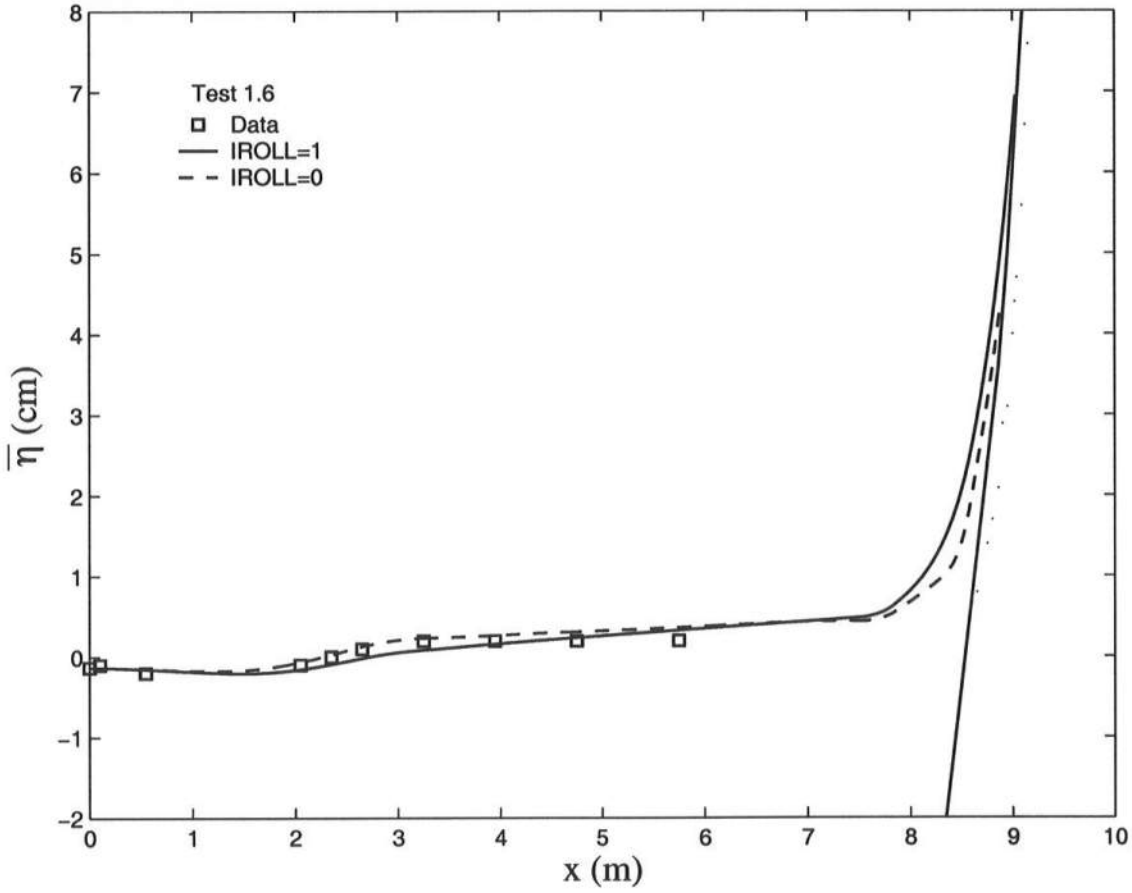

Figure 4.2: Measured and computed mean free surface elevation $\overline{\eta}$ for test 1.6 where IROLL = 1 and 0 indicate the computed results with and without the roller volume flux q_r

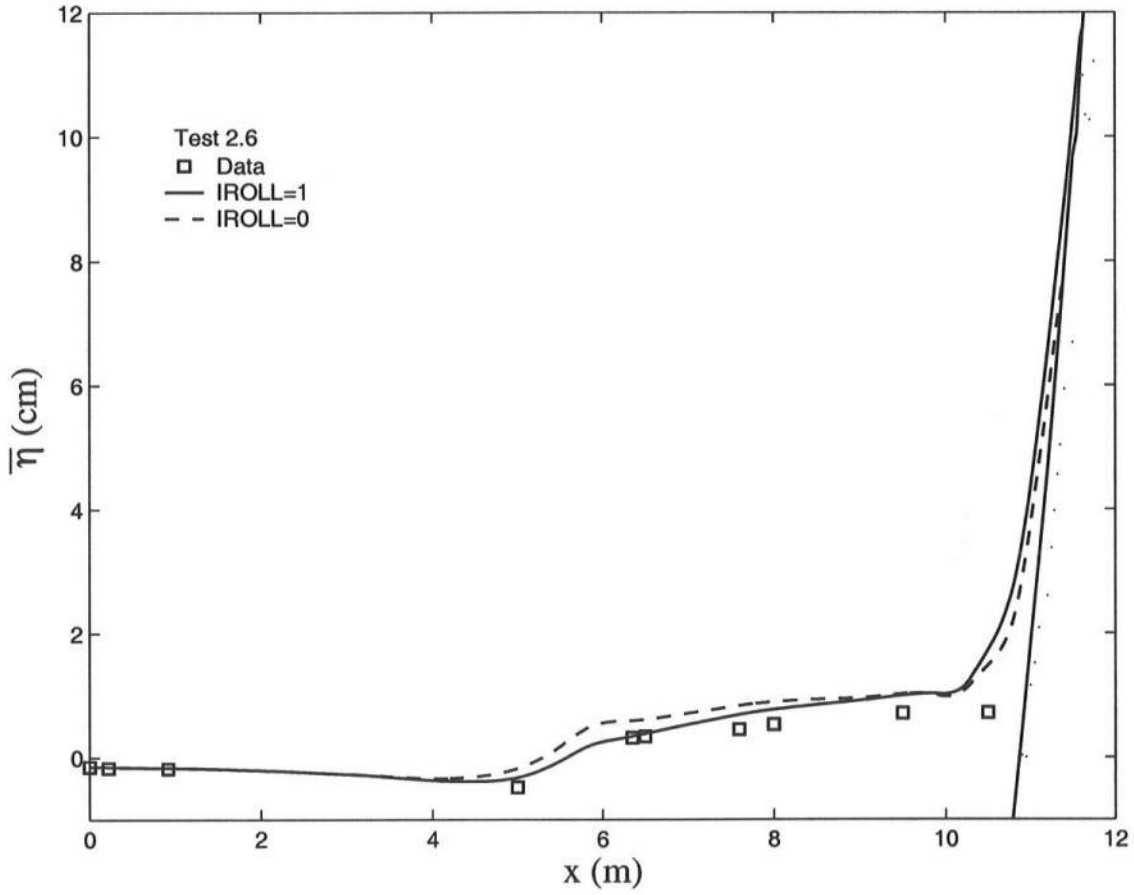

Figure 4.3: Measured and computed mean free surface elevation $\overline{\eta}$ for test 2.6 where IROLL = 1 and 0 indicate the computed results with and without the roller volume flux q_r

Table 4.1: Measured and computed reflection coefficients for tests 4.8, 1.6 and 2.6

Test	Data	IROLL =0	IROLL=1
4.8	0.33	0.21	0.24
1.6	0.14	0.15	0.18
2.6	0.16	0.22	0.24

Figure 4.4 - 4.6 show the measured and computed cross-shore variations of the standard deviation σ_η for tests 4.8, 1.6 and 2.6, respectively. The difference between IROLL = 0 and 1 is essentially limited to the swash zone because of the adopted wave energy equation (4.1) with the wave energy flux $F = \rho g C_g \sigma_\eta^2$ without any effect of q_r. The agreement with the data is better for tests 4.8 and 2.6 because no data point deviates noticeably from the computed σ_η. The good agreement is partially due to the calibration of γ for each test. The reflected wave height is estimated using equation (4.12) where use is made intuitively of the value of F at the still water shoreline. Since σ_η decreases rapidly near the shoreline, the estimated reflected wave height is sensitive to the selected location of wave reflection. The measured and computed reflection coefficients at wave gauge 1 are compared in Table 4.1. This simple and intuitive method appears to be useful in estimating the order of magnitude of wave reflection using the time-averaged model.

4.3 Comparisons with Velocity Data

Figure 4.7 - 4.9 show the measured and computed cross-shore variations of the mean horizontal velocity $\overline{U}$ for the three tests. The measured values of $\overline{U}$ at the different elevations and the average velocity $-\overline{U_0}$ at each line defined in equation (3.7) are compared with the computed depth-averaged $\overline{U}$ given by equation (4.5).

These comparisons are approximate because the numerical model does not predict the vertical variation of $\overline{U}$. For test 4.8 with mostly plunging breakers, the agreement is better for IROLL = 0 with $q_r = 0$. For test 1.6 with mostly

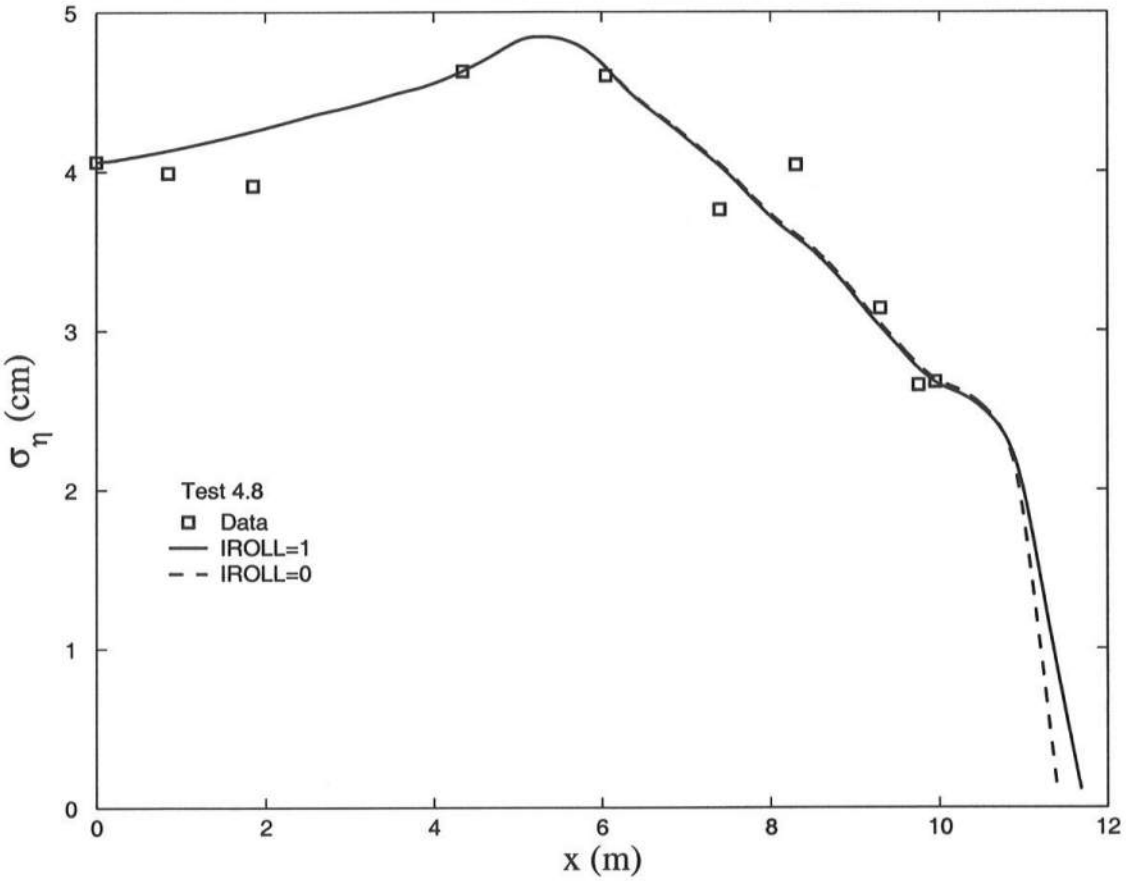

Figure 4.4: Measured and computed standard deviation σ_η of free surface elevation for test 4.8

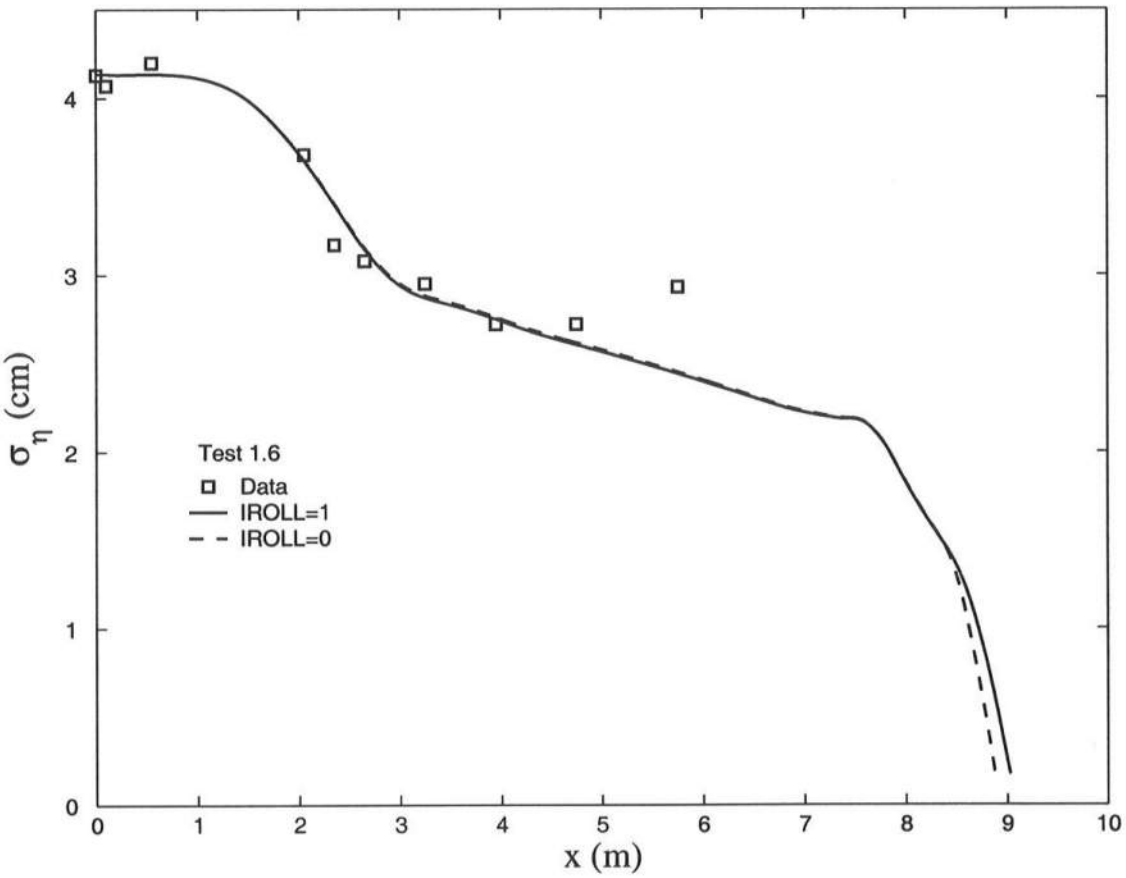

Figure 4.5: Measured and computed standard deviation σ_η of free surface elevation for test 1.6

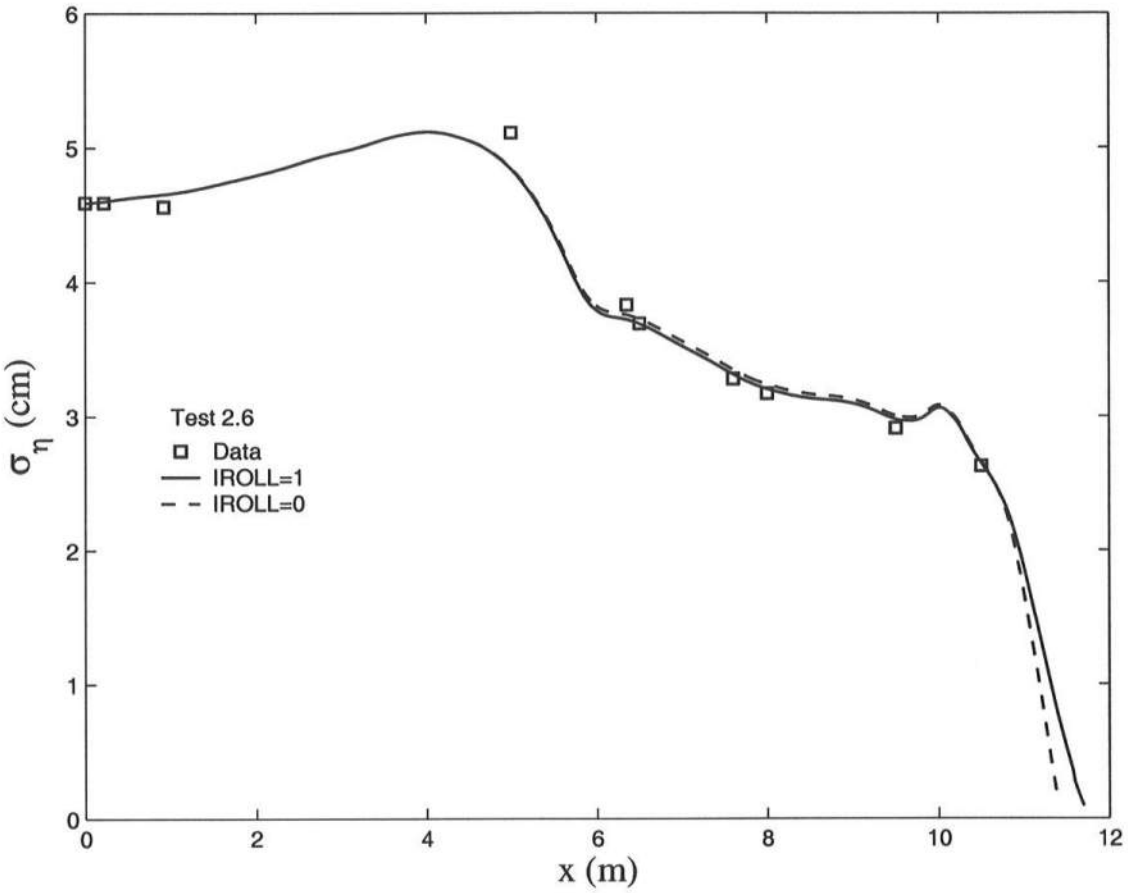

Figure 4.6: Measured and computed standard deviation σ_η of free surface elevation for test 2.6

spilling breakers, the agreement is better for IROLL=1 with the roller volume flux. The largest undertow current on the shoreward side of the bar, which was also observed on a natural barred beach [Garcez Faria et al., 2000], cannot be predicted by the present roller model. Test 2.6 is intermediate between tests 4.8 and 1.6. The computed large offshore mean velocity in the swash zone is qualitatively consistent with the field data of Raubenheimer [2002] and the mean velocities computed by Tega et al. [2004] for tests 4.8 and 1.6 using the time-dependent model by Kobayashi and Wurjanto [1992].

Figure 4.10 - 4.12 show the measured and computed cross-shore variations of the standard deviation σ_U for the three tests where the measured σ_U at the different elevations did not vary much. The computed increase of σ_U near the shoreline before its rapid shoreward decrease is consistent with the field data of Raubenheimer [2002]. The numerical model overpredicts σ_U for test 2.6.

Figure 4.13 - 4.15 show the measured turbulent velocity $k^{0.5}$ at the different elevations at the each line for the three tests together with the extrapolated values of $u_0^{'}$ and $u_0^{'}exp(\overline{h}/\ell_t)$ using equation (3.10) where $\ell_t < 0$ at lines 4.8A, 1.6A, 1.6G and 2.6A. The computed turbulent velocities $u_f^{'} = (D_f/\rho)^{1/3}$ and $u_B^{'} = (D_B/\rho)^{1/3}$ are those associated with the energy dissipation rates due to the bottom friction and wave breaking, respectively, where D_B is replaced by $(\rho g \beta_\gamma q_r)$ for IROLL = 1 as discussed in relation to equation (4.13). The use of D_B to estimate k near the bottom was proposed by Roelvink and Stive [1989]. This procedure does not work at the lines where k decreases upward. The measured $k^{0.5}$ is better represented by $u_f^{'}$ but is smaller than $u_f^{'}$ in the outer breaker zone. Since $u_f^{'}$ is proportional to $f_b^{1/3}$ in view of equation (4.7), the bottom friction factor $f_b = 0.015$ needs to be reduced to the order of 0.0015 in the outer breaker zone. For alongshore currents on a natural beach, Feddersen et al. [1998] estimated their drag coefficients, $c_f = f_b/2$, to be 0.0033 and 0.0010 within and seaward of the surf zone, respectively. The seaward

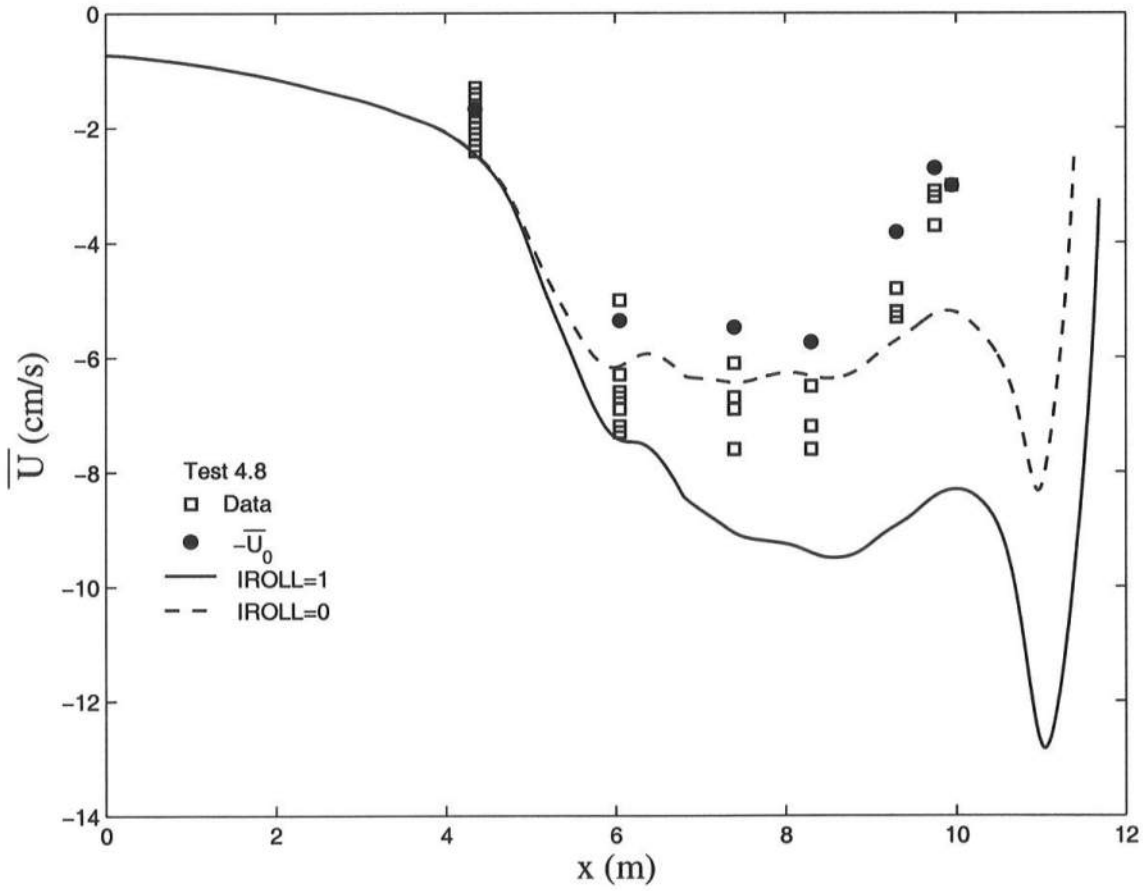

Figure 4.7: Measured and computed mean horizontal velocity $\overline{U}$ for test 4.8 where the square denotes the measured value at each elevation and the dot indicates the value of $-\overline{U_0}$ at each line

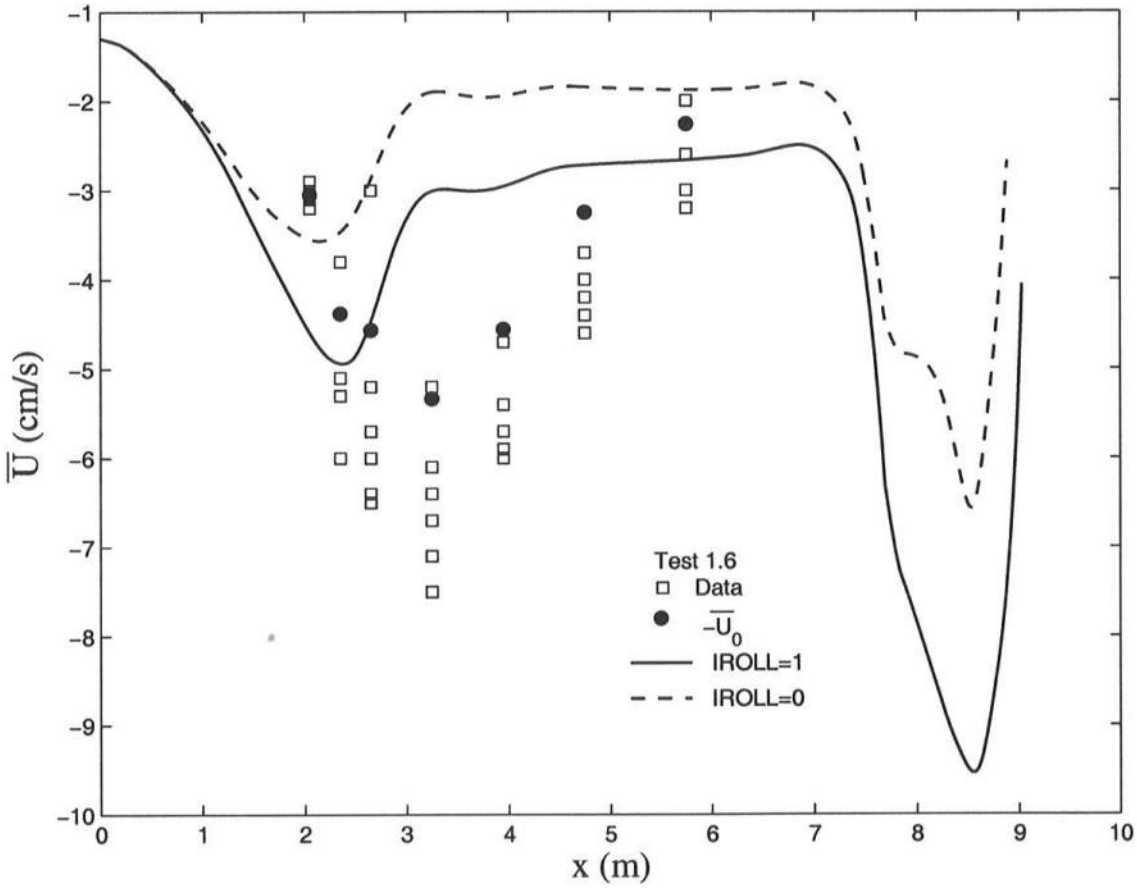

Figure 4.8: Measured and computed mean horizontal velocity $\overline{U}$ for test 1.6 where the square denotes the measured value at each elevation and the dot indicates the value of $-\overline{U_0}$ at each line

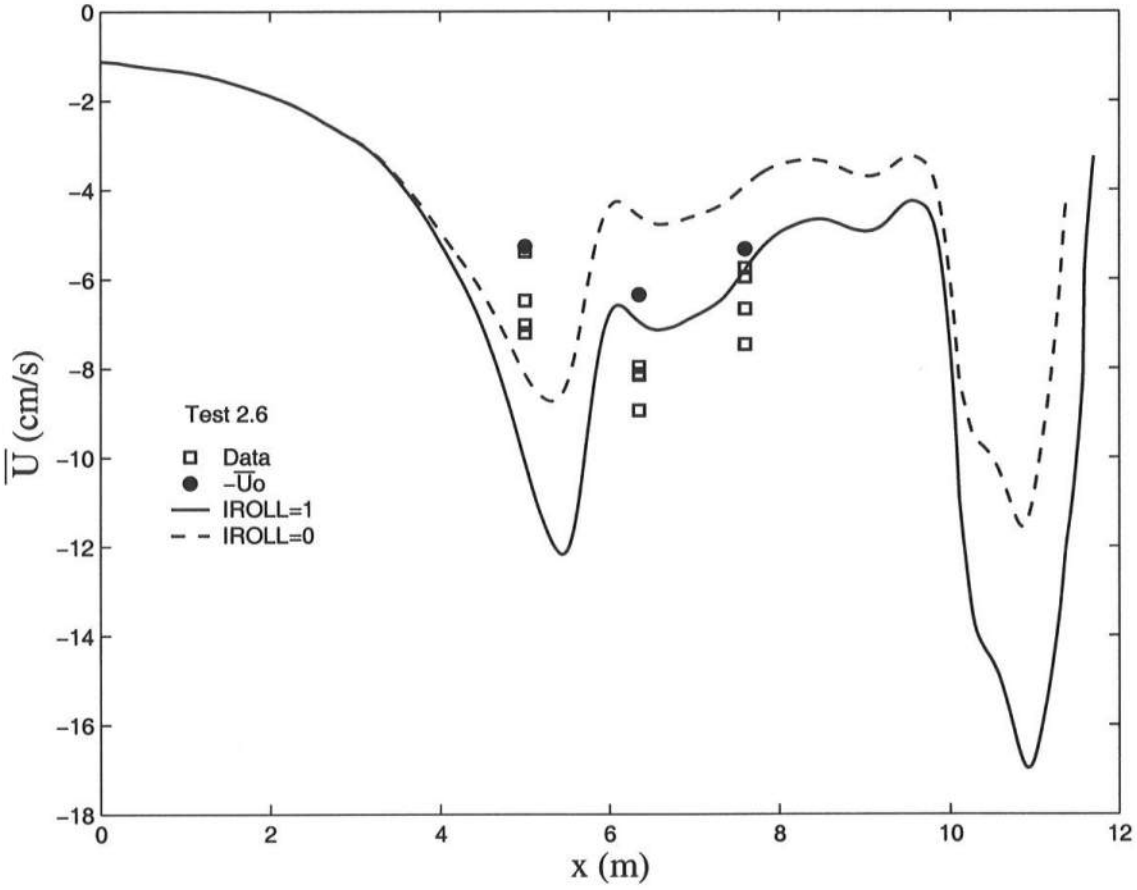

Figure 4.9: Measured and computed mean horizontal velocity $\overline{U}$ for test 2.6 where the square denotes the measured value at each elevation and the dot indicates the value of $-\overline{U_0}$ at each line

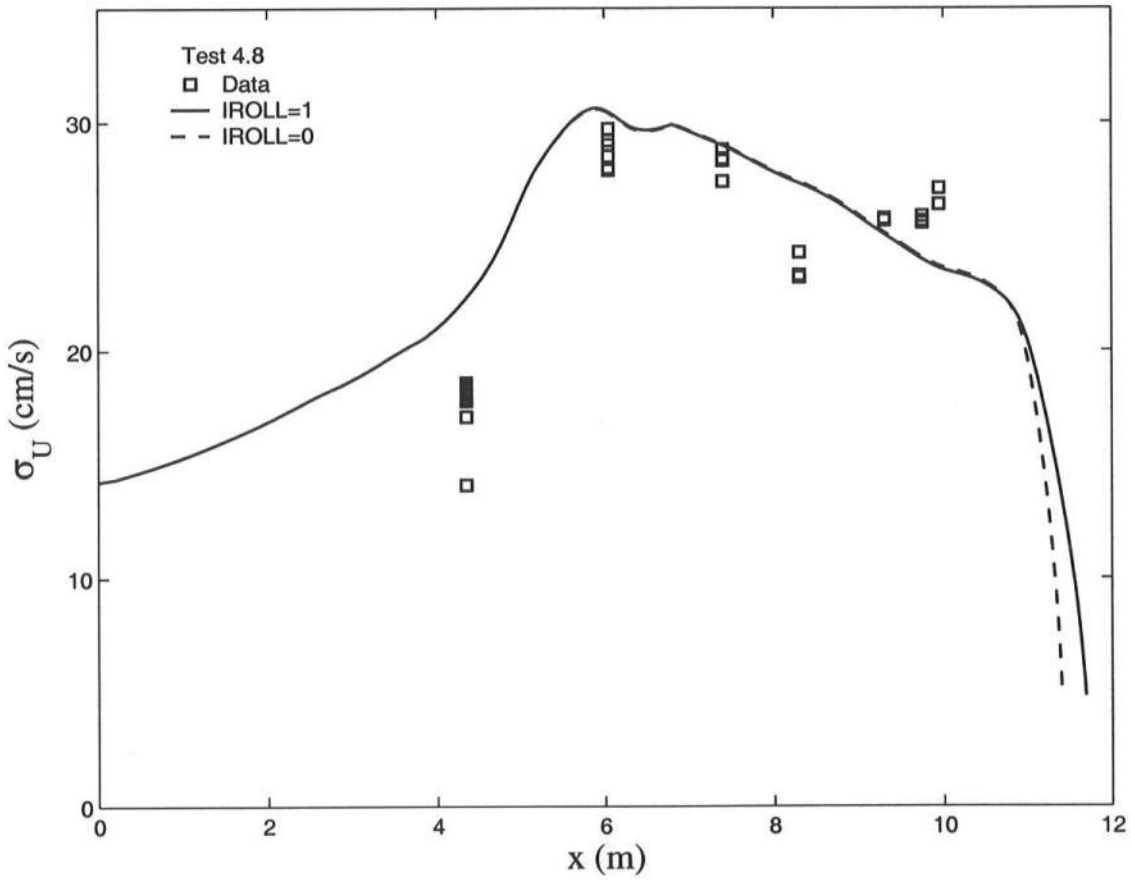

Figure 4.10: Measured and computed standard deviation σ_U of horizontal fluid velocity for test 4.8 where the square denotes the measured value at each elevation

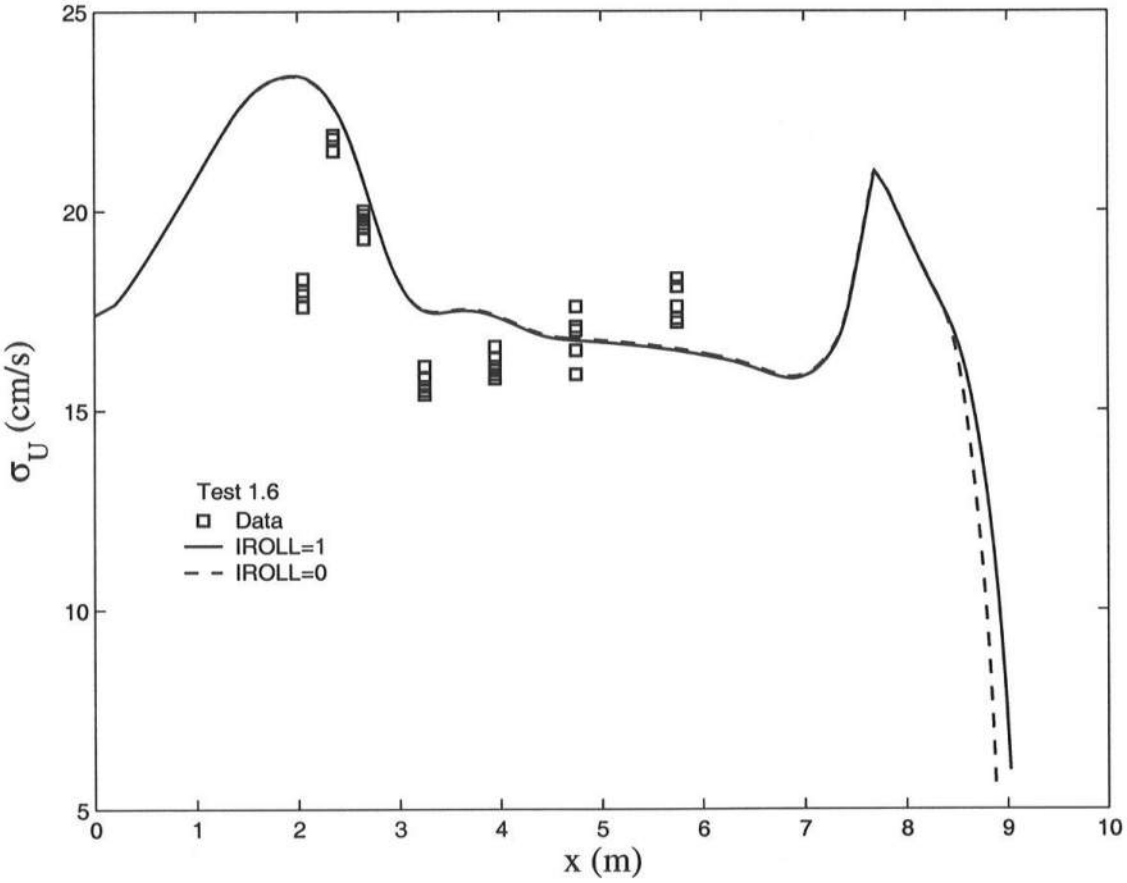

Figure 4.11: Measured and computed standard deviation σ_U of horizontal fluid velocity for test 1.6 where the square denotes the measured value at each elevation

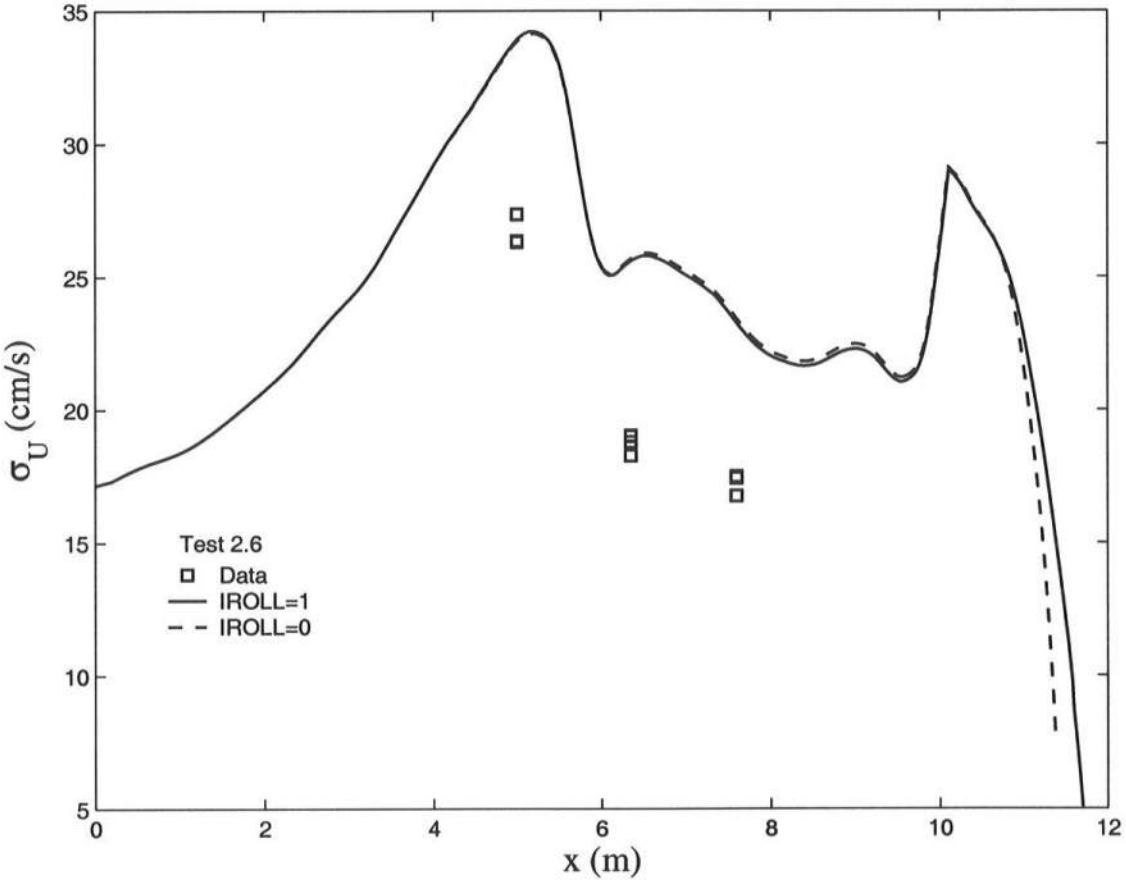

Figure 4.12: Measured and computed standard deviation σ_U of horizontal fluid velocity for test 2.6 where the square denotes the measured value at each elevation

decrease of c_f is qualitatively consistent with the required seaward reduction of f_b to improve the agreement between u_f' and $k^{0.5}$, although the precise value of f_b is uncertain. The roller effect causes the spatial lag between the wave breaking and energy dissipation and shifts u_B' shoreward. The measured and extrapolated turbulent velocities in comparison with u_B' indicate the additional spatial lag which may be related to the downward transfer of eddies generated by wave breaking. Infrequent but intense turbulent events of short durations, which are important for sediment suspension, are not represented well by the time-averaged turbulent velocity $k^{0.5}$ [Cox and Kobayashi, 2000]. Relatedly, the wave friction factor f_w based on the maximum bottom shear stress appears to be much larger than the bottom friction factor f_b associated with the time-averaged bottom shear stress and turbulent velocities [Cox and Kobayashi, 1997]. The formula by Madsen and Salles [1999] together with the ripple height and length measured in this experiment predicts f_w to be of the order of 0.1 in comparison with $f_b = 0.015$ used here. Similarly, Feddersen et al. [2003] found no relationship between the bottom friction factor for alongshore currents and the bottom roughness (bed forms) inside the surf zone on a natural beach. The time averaging masks the intermittent turbulence caused by wave breaking and ripples.

4.4 Comparisons with Suspended Sediment Data

Figure 4.16 - 4.18 show the measured and computed suspended sediment volume $\overline{V}$ per unit area for tests 4.8, 1.6 and 2.6 where use is made of equation (3.19) and (4.13). The exponential and power-form distributions of the mean concentration yield the similar values of $\overline{V}$. Consequently, the disagreement between the measured and computed values of $\overline{V}$ indicates the shortcoming of equation (4.13). The roller effect causes the shoreward shift of $\overline{V}$ but does not necessarily improve the agreement. No measurement was made in the swash zone but visual observations indicated intense sediment suspension due to wave breaking and swash oscillations

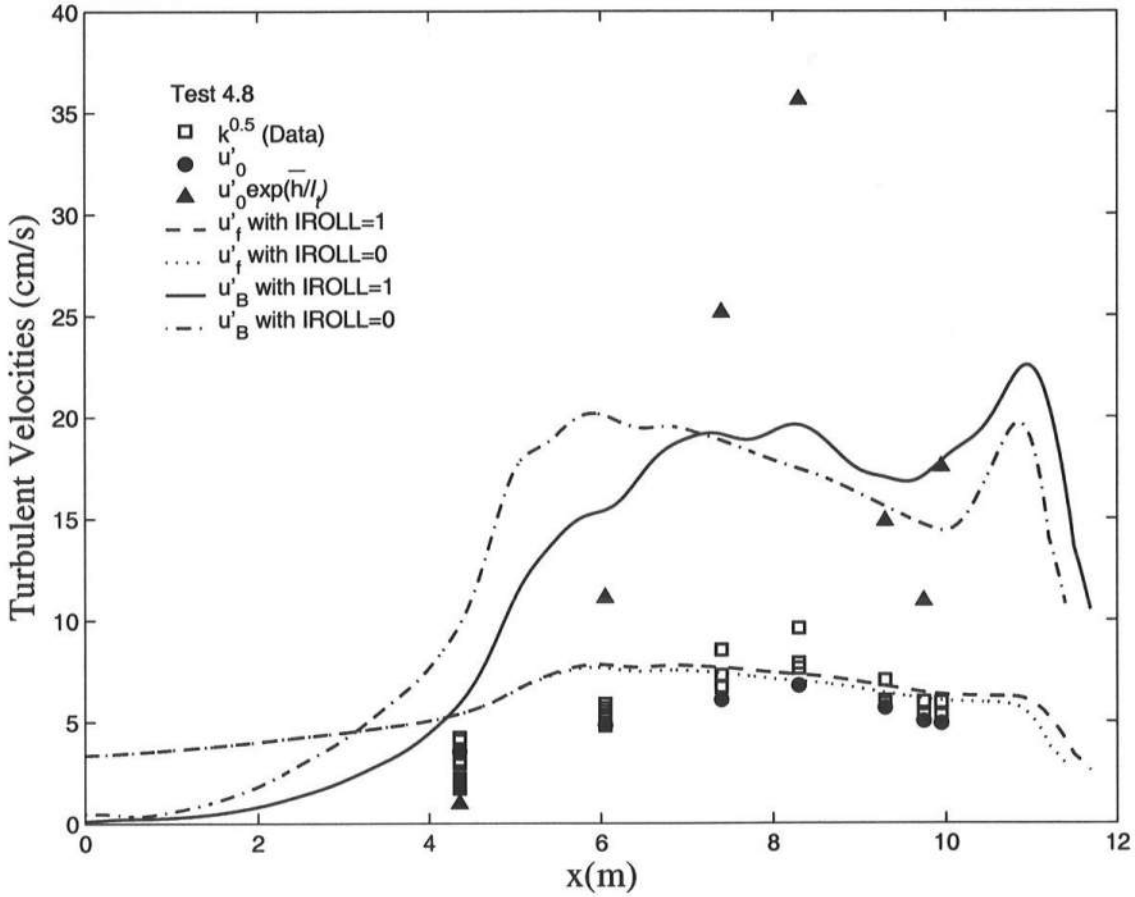

Figure 4.13: Measured turbulent velocity $k^{0.5}$ (square) and fitted $u_0^{'}$ (dot) and $u_0^{'}exp(\overline{h}/\ell_t)$ (solid triangle) at each line in comparison with computed $u_f^{'} = (D_f/\rho)^{1/3}$ and $u_B^{'} = (D_B/\rho)^{1/3}$ for test 4.8

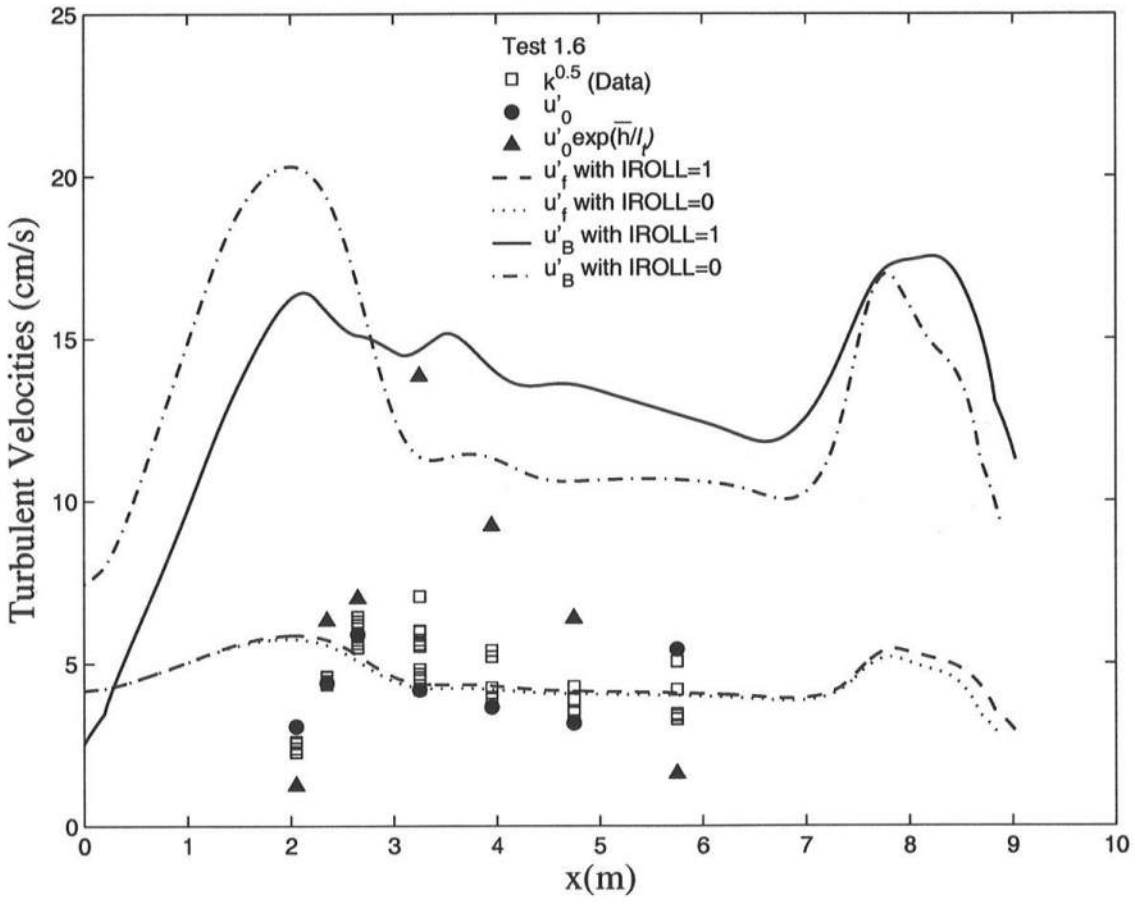

Figure 4.14: Measured turbulent velocity $k^{0.5}$ (square) and fitted u_0' (dot) and $u_0' exp(\overline{h}/\ell_t)$ (solid triangle) at each line in comparison with computed $u_f' = (D_f/\rho)^{1/3}$ and $u_B' = (D_B/\rho)^{1/3}$ for test 1.6

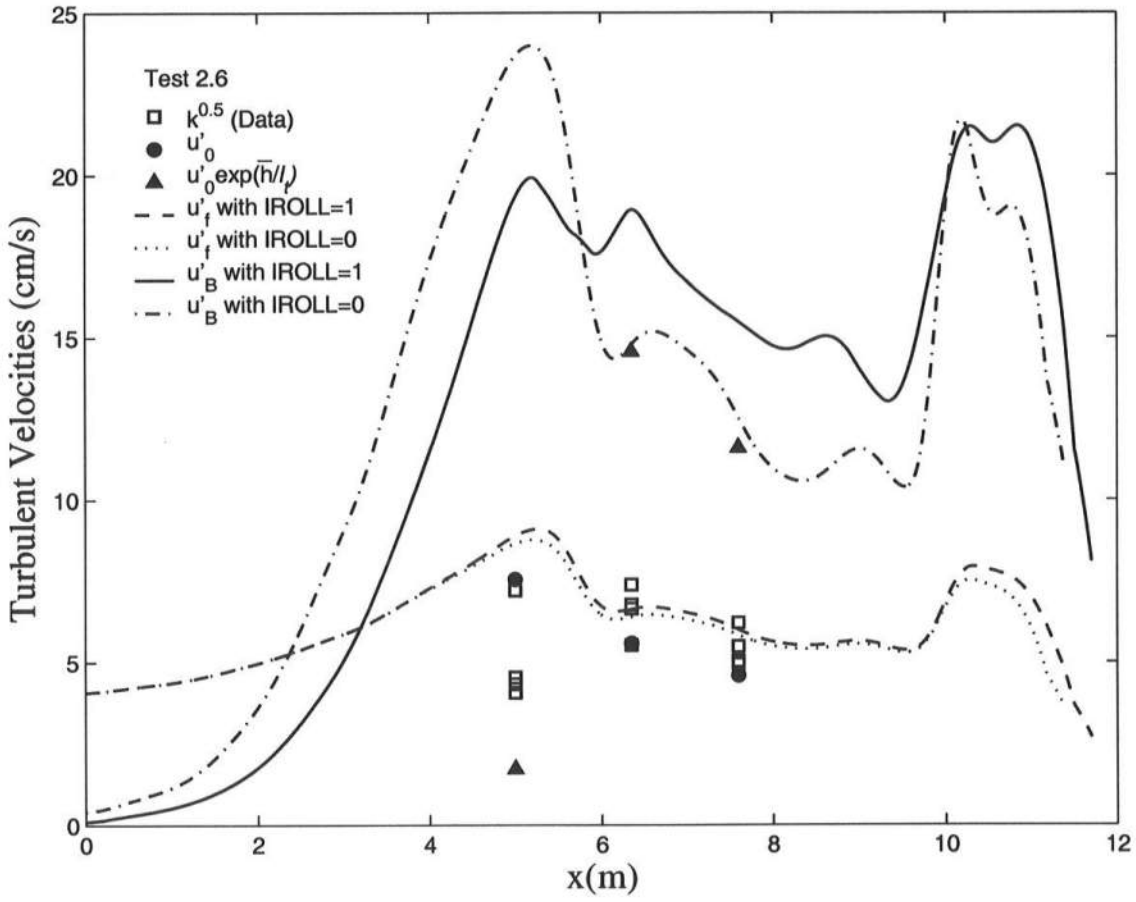

Figure 4.15: Measured turbulent velocity $k^{0.5}$ (square) and fitted $u_0^{'}$ (dot) and $u_0^{'}exp(\overline{h}/\ell_t)$ (solid triangle) at each line in comparison with computed $u_f^{'} = (D_f/\rho)^{1/3}$ and $u_B^{'} = (D_B/\rho)^{1/3}$ for test 2.6

in manners similar to the field measurement by Puleo et al. [2000]. The agreement within a factor of about two is similar to the accuracy of the time-dependent model by Kobayashi and Tega [2002], which requires much more computation time than the present time-averaged model. The offshore and onshore suspended sediment transport rates may be predicted using equation (3.23) at least for equilibrium beaches but it will be necessary to improve the accuracy of the predicted $\overline{V}$. Nevertheless, equation (4.13) for $\overline{V}$ may be better than available formulas for the reference concentrations $\overline{C_b}$ and $\overline{C_a}$ in equations (3.17) and (3.18) and may also be used for the prediction of longshore suspended sediment transport.

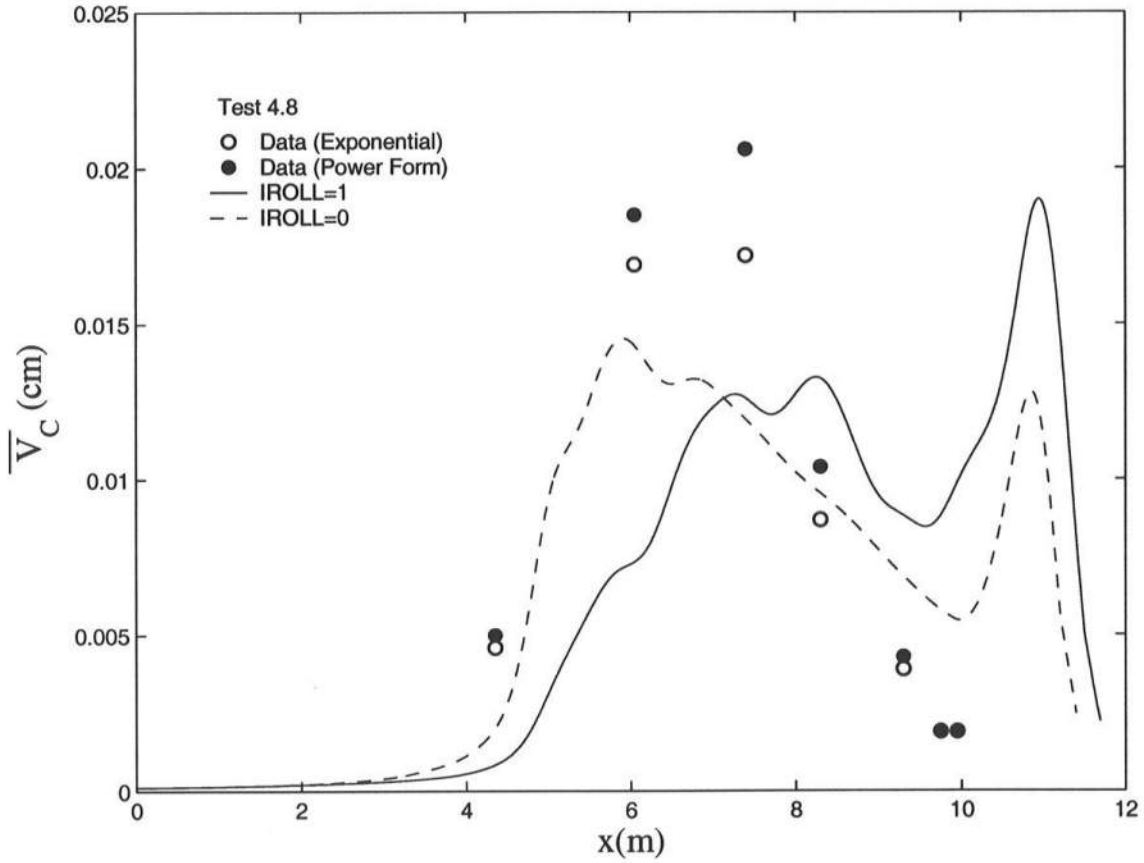

Figure 4.16: Measured and computed suspended sediment volume $\overline{V}$ per unit area for test 4.8 where the circle and dot denote the calculated values of $\overline{V}$ using the fitted exponential and power-form distributions at each line

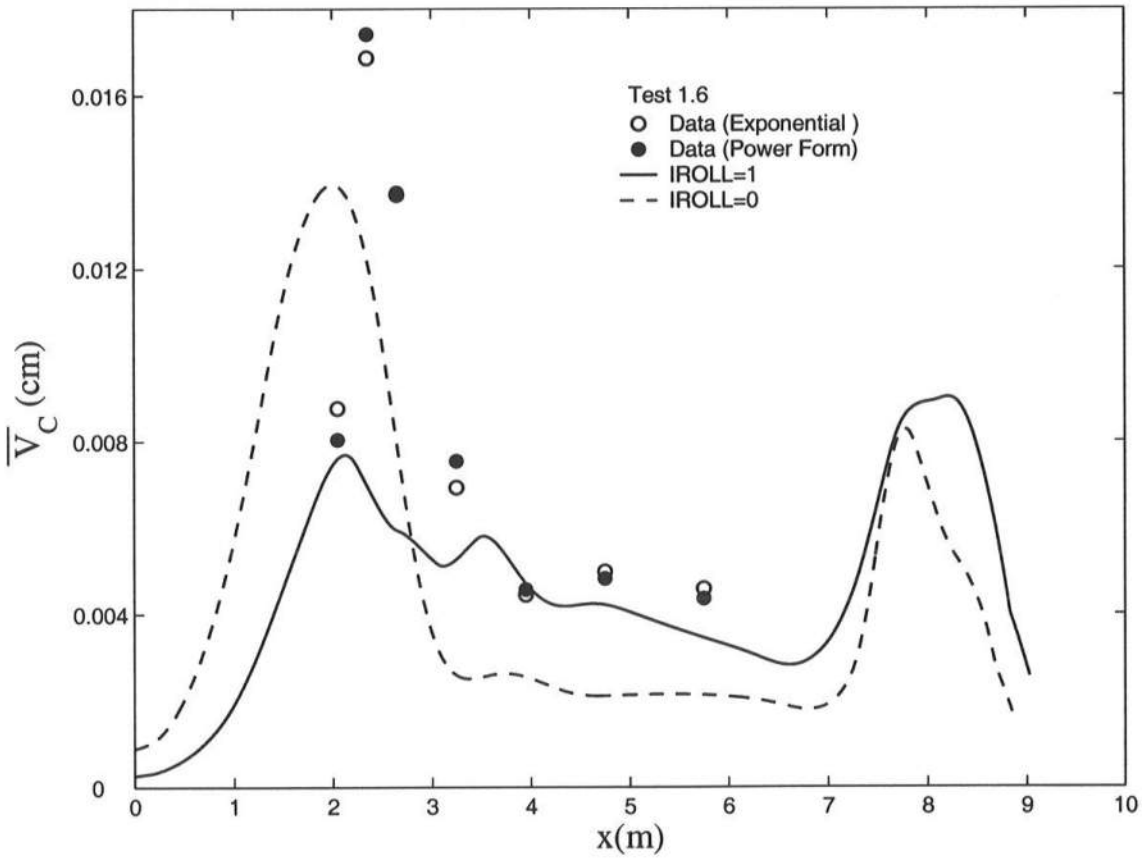

Figure 4.17: Measured and computed suspended sediment volume $\overline{V}$ per unit area for test 1.6 where the circle and dot denote the calculated values of $\overline{V}$ using the fitted exponential and power-form distributions at each line

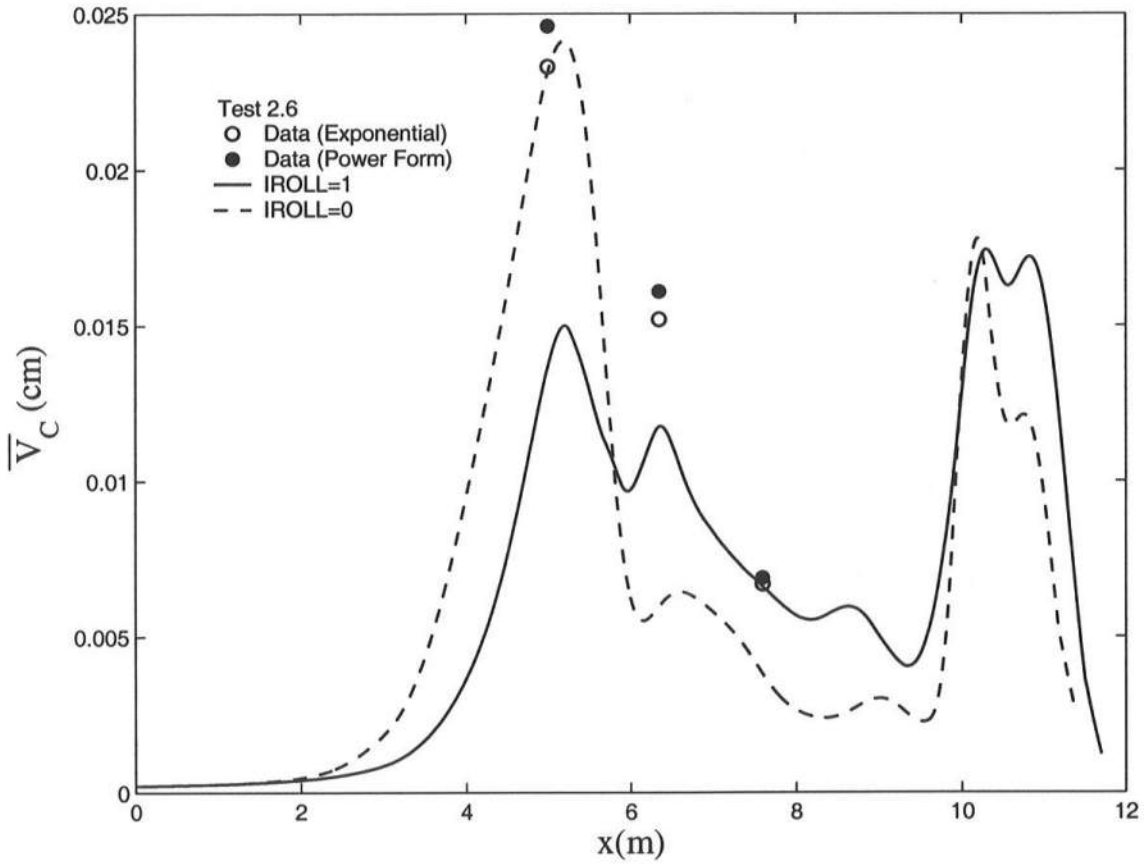

Figure 4.18: Measured and computed suspended sediment volume $\overline{V}$ per unit area for test 2.6 where the circle and dot denote the calculated values of $\overline{V}$ using the fitted exponential and power-form distributions at each line

Chapter 5

CONCLUSIONS

Three tests were conducted in a wave flume to investigate suspended sand transport on equilibrium beaches produced by irregular breaking waves with the spectral peak period $T_p = 4.8$, 1.6 and 2.6 s. Free surface elevations were measured at ten locations for each test to estimate the incident and reflected waves and obtain the cross-shore variation of the mean $\overline{\eta}$ and standard deviation σ_η of the free surface elevation η. Velocities and sand concentrations were measured at 94 elevations along 17 vertical lines in the vicinity of the bottom to obtain the turbulent velocity variances, the mean $\overline{U}$ and standard deviation σ_U of the horizontal velocity U, the mean $\overline{C}$ and the standard deviation σ_C of the concentration C, and the correlation coefficient γ_{UC} between U and C.

The relations among the three turbulent velocity variances are found to be similar to those in the inner region of the boundary layer flow. The time-averaged turbulent velocity $k^{0.5}$, where k is the measured turbulent kinetic energy, is shown to increase or decrease exponentially with the elevation z_m above the local bottom. The vertical decrease of $k^{0.5}$ under infrequent or weak wave breaking indicates the importance of turbulence generated by bottom friction. The vertical profile of the measured $\overline{U}$ is parabolic and the fitted parabolic profile is used to estimate the time-averaged offshore volume flux q_0 and average velocity $\overline{U_0}$. The measured σ_U varies little vertically and $\sigma_U \simeq \sigma_*(g\overline{h})^{0.5}$ based on linear shallow water theory where $\sigma_* = \sigma_\eta/\overline{h}$ and $\overline{h}$ is the mean water depth. The vertical variation of the

measured $\overline{C}$ can be fitted by the exponential and power-form distributions equally well. Instead of the reference concentration, the suspended sediment volume $\overline{V}$ per unit area is predicted by the time-averaged model proposed here. On the other hand, the equation for the standard deviation σ_C is derived to show that the ratio $\alpha = \sigma_C/\overline{C}$ is approximately independent of z_m. The correlation coefficient γ_{UC} is of the order of 0.1 and decreases upward linearly. The offshore suspended sediment transport rate q_{off} due to undertow current is approximately given by $\overline{U_0}\ \overline{V}$. The onshore transport rate q_{on} due to the positive correlation between U and C and the onshore volume flux q_0 near the free surface is approximately estimated as $\sigma_* \sigma_U \overline{V}$. The condition of no net sediment transport rate on the equilibrium beach is used to estimate the bed load transport rate, which is of the same order of q_{off} and q_{on} and is either offshore or onshore.

A time-averaged numerical model is developed to predict the cross-shore variations of $\overline{\eta}$, $\sigma_\eta, \overline{U}, \sigma_U$ and $\overline{V}$. The numerical model is based on the time-averaged continuity, momentum and energy equations together with the local use of linear shallow-water wave theory. The bottom shear stress and the energy dissipation rate D_f due to bottom friction are estimated using the quadratic friction equation together with the Gaussian distribution of U. The energy dissipation rate D_B due to wave breaking is estimated using the formula of Battjes and Stive [1985], which is modified to include the effect of the upward bottom slope on the increase of D_B near the shoreline. This modification permits the landward-marching computation well above the still water shoreline without any numerical difficulty. The wave reflection coefficient is estimated intuitively assuming that the wave energy flux remaining at the still water shoreline is reflected and propagates seaward. The suspended sediment volume $\overline{V}$ is predicted using the computed D_f and D_B. The roller effect expressed in terms of the roller volume flux q_r is included to increase the offshore return current.

The developed model is compared with the three tests. The cross-shore variations of $\overline{\eta}$, σ_η and σ_U can be predicted well as was the case with existing models. The wave reflection coefficient is predicted reasonably well in spite of the intuitive assumption. The computed $\overline{U}$, which does not vary vertically, is compared with the measured $\overline{U}$ and $\overline{U_0}$. The roller effect improves the agreement only for test 1.6 involving mostly spilling breakers on the bar beach. For mostly plunging breakers on the terraced beach in test 4.8, the agreement is better for $q_r = 0$, suggesting that our understanding of the roller and undertow is not adequate for the accurate prediction of q_{off}. The turbulent velocities estimated from the computed D_f and D_B are compared with the measured turbulent velocity $k^{0.5}$. The turbulent velocities measured in the vicinity of the bottom are found to be more related to the energy dissipation due to bottom friction. This finding is consistent with the relations among the turbulent velocity variances, which are similar to those for the boundary layer flow. The suspended sediment volume $\overline{V}$ can be predicted only within a factor of about two. However, the factor of two is of similar accuracy of time-dependent suspended sediment models that require much more computational efforts. The eventual use of this time-averaged model is the prediction of long-term beach profile evolutions. For this purpose, it will be necessary to develop a model for bed load that can predict the estimated bed load transport rates on the three equilibrium beaches in this experiment.

BIBLIOGRAPHY

Bailard, J.A. (1981), An energetics total load sediment transport model for a plane sloping beach, *J.Geophys. Res.,* 86, 10, 938-10,954.

Battjes, J.A., and Stive, M.J.F. (1985), Calibration and verification of a dissipation model for random breaking waves, *J.Geophys. Res.,* 90, 9159-9167

Cox, D.T., and Kobayashi, N. (1996), Undertow profiles in the bottom boundary layer under breaking waves, paper presented at *25th Coastal Engineering Conference*, Am. Soc. of Civ. Eng., Reston, Va.

Cox, D. T., and Kobayashi, N. (1997), A kinetic undertow model with a logarithmic boundary layer, *J. Waterw.Port Coastal and Ocean Eng.,* 123, 354-360.

Cox, D. T., and Kobayashi, N. (2000), Identification of intense, intermittent coherent motions under shoaling and breaking waves, *J.Geophys. Res.,* 105, 14, 223-14,236.

Dalrymple, R.A. (1992), Prediction of storm/normal beach profiles, *J. Waterw.Port Coastal and Ocean Eng.,* 118, 193-200.

Deigaard, R. (1993), A note on the three dimensional shear stress distribution in a surf zone, *Coastal Eng.*, 20, 157-171.

Deigaard, R. and Fredsφe, J. (1989), Shear stress distribution in dissipative water waves, *Coastal Eng.*, 13, 357-378.

Dean, R.G., and Dalrymple, R.A. (1984), Water wave mechanics for engineers and scientists, *World Scientific*, Singapore

Downing, J.P., Sternberg, R.W., and Lister, C.R.B. (1981), New instrumentation for the investigation of sediment suspension processes in the shallow marine environment, *Mar. Geol.* , 42, 19-34, 1981.

Dunkley, E.C., Mocke,G.P., Diedericks,G.P.J., and Tanczos I. (1999), Evaluation of bed shear, vertical mixing and reference concentration formulations, paper presented at *Coastal Sediments'99 Conference*, Am. Soc. of Civ. Eng., Reston, Va.

Freddersen, F., Gallagher, E. L., Guza, R.T., and Elgar, S. (2003), The drag coefficient, bottom roughness and wave-breaking in the nearshore, *Coastal Eng.*, 48, 189-195.

Freddersen, F., Guza,R. T., Elgar, S., and Herbers, T.H. (1998), Alongshore momentum balances in the nearshore, *J.Geophys. Res.,* 103, 15, 667-15,676.

Garcez Faria, A.F., Thornton, E.B, Lippmann, T.C., and Stanton, T.P. (2000), Undertow over a barred beach, *J.Geophys. Res.,* 105, 16,999-17,010.

Gallagher, E.L., Elgar, S., and Guza, R.T. (1998), Observations of sand bar evolution on a natural beach, *J.Geophys. Res.,* 103, 3203-3215.

Giovannozzi, M.A., and Kobayashi, N. (2002), Intermittent high sand concentrations measured under irregular breaking waves, paper presented at *28th Coastal Engineering Conference*, World Scientific, Singapore.

Guza, R.T., and Thornton, E.B. (1980), Local and shoaled comparisons of sea surface elevations, pressure and velocities, *J.Geophys. Res.,* 85, 1524-1530.

Guza, R.T., and Thornton, E.B. (1985), Velocity moments in nearshore, *J. Waterw.Port Coastal and Ocean Eng.,* 111, 235-256

Henderson, S.M., Allen J.S., and Newberger ,P.A. (2004), Nearshore sandbar migration predicted by an eddy-diffusive boundary layer model, *J.Geophys. Res.,* 109, C06024, doi:10.1029/2003JC002137.

Hoefel, F., and Elgar, S. (2003), Wave-induced sediment transport and sandbar migration, *Science*, 299, 1885-1887.

Hsu, T.J., and Liu, P.L.F. (2004), Toward modeling turbulent suspension of sand in the nearshore, *J.Geophys. Res.*,109, C06018, doi:10.1029/2003JC002240.

Karambas, T.V., and Koutitas, C. (2002), Surf and swash zone morphology evolution induced by nonlinear waves, *J. Waterw.Port Coastal and Ocean Eng.,* 128, 103-113.

Kobayashi, N., and Johnson, B.D. (2001), Sand suspension, storage, advection, and settling in surf and swash zones, *J.Geophys. Res.,* 106, 9363-9376.

Kobayashi, N., and Lawrence, A.R. (2004), Cross-shore sediment transport under breaking solitary waves, *J.Geophys. Res.,* 109, C03047, doi:10.1029/2003 JC002084.

Kobayashi, N., and Tega, Y. (2002), Sand suspension and transport on equilibrium beach, *J. Waterw.Port Coastal and Ocean Eng.,* 128, 238-248.

Kobayashi, N., and Wurjanto, A. (1992), Irregular wave setup and run-up on beaches, *J. Waterw.Port Coastal and Ocean Eng.,* 118, 368-386.

Kobayashi, N., Cox, D.T., and Wurjanto, A. (1990), Irregular wave reflection and run-up on rough impermeable slopes, *J. Waterw.Port Coastal and Ocean Eng.,* 118, 708-726.

Kobayashi, N., Herrman, M.N., Johnson, B.D., and Orzech, M.D. (1998), Probabilistic distribution of surface elevation in surf and swash zones, *J. Waterw.Port Coastal and Ocean Eng.,* 124, 99-107.

Kobayashi, N., Meigs, L.E., Ota, T., and Melby, J.A. (2005), Irregular wave transmission over submerged porous breakwaters, *J. Waterw.Port Coastal and Ocean Eng.,* 131 (submitted).

Kobayashi, N., Zhao H., and Tega, Y. (2005), Suspended sand transport in surf zones, *J. Geophys. Res.,* (submitted)

Lawrence, A.R., and Kobayashi, N. (2003), Experiments on cross-shore sediment transport under positive and negative solitary waves, *Research Report No. CACR-03-03*, Center for Applied Coastal Research, Univ. of Delaware, Newark, Del.

Lee, G.-H., Dade, W.B., Friedricks, C.T., and Vincent, C.E. (2004), Examination of reference concentration under waves and currents on the inner shelf, *J.Geophys. Res.,* 109, C02021, doi:10.1029/2002JC001707.

Madsen, O.S., and Salles, P. (1999), Eddy viscosity models for wave boundary layers, paper presented at *26th Coastal Engineering Conference*, Am. Soc. of Civ. Eng., Reston, Va.

Nielsen, P. (1992), Coastal bottom boundary layers and sediment transport, *World Scientific*, Singapore.

Peters, K., and Dette, H.H. (1999), Sediment suspension in the surf zone, paper presented at *Coastal Sediment'99 Conference*, Am. Soc. of Civ. Eng., Reston, Va.

Plant, N.G., Ruessink, B.G., and Wijnberg, K.M. (2001), Morphologic properties derived from a simple cross-shore sediment transport model, *J.Geophys. Res.*, 106, 945-958.

Puleo, J.A., Beach, R.A., Holman, R.A., and Allen, J.S. (2000), Swash zone sediment suspension and transport and the importance of bore- generated turbulence, *J.Geophys. Res.*, 105, 17, 021-17,044.

Ribberink, J.S. (1998), Bed-load transport for steady flows and unsteady oscillatory flows, *Coastal Eng.*, 34, 59-82.

Ribberink, J.S. and Al-Salem, A.A. (1994), Sediment transport in oscillatory boundary layers in cases of rippled beds and sheet flow, *J.Geophys. Res.*, 99, 12, 707-12,727.

Raubenheimer, B. (2002), Observations and predictions of fluid velocities in the surf and swash zones, *J.Geophys. Res.*, 107, 1-7.

Raubenheimer, B., Guza, R.T., and Elgar, S. (1996), Wave transformation across the inner surf zone, *J.Geophys. Res.*, 101, 25,589-25,597.

Raubenheimer, B., Guza, R.T.,and Elgar, S. (2001), Field observations of wave-driven setdown and setup, *J.Geophys. Res.*, 106, 4629-4638.

Raubenheimer, B.,Guza, R.T., Elgar, S., and Kobayashi, N. (1995), Swash on a gently sloping beach *J.Geophys. Res.*, 100, 8751-8760.

Roelvink, J.A., and Stive, M.J.F. (1989), Bar-generating cross-shore flow mechanisms on a beach, *J.Geophys. Res.*, 94, 4785-4800.

Ruessink, B.G., Miles, J.R., Feddersen, F., Guza, R.T., and Elgar, S. (2001) Modeling the alongshore current on a barred beaches, *J.Geophys. Res.*, 106, 22,451-22,463.

Stive, M.J.F., and DeVriend, H. J. (1994), Shear stresses and mean flow in shoaling and breaking waves, paper presented at *24th Coastal Engineering Conference*, Am. Soc. of Civ. Eng., Reston, Va.

Svendsen, I.A. (1984), Mass flux and undertow in a surf zone, *Coastal Eng.*, 8, 347-365.

Svendsen, I.A. (1987), Analysis of surf zone turbulence, *J. Geophys. Res.*, 92, 5115-5124.

Svendsen, I.A., Qin, W., and Ebersole, B.A. (2003), Modeling waves and currents at the LSTF and other laboratory facilities, *Coastal Eng.*, 20, 19-45.

Tega, Y., Kobayashi, N., Giovannozzi, M.A., and Johnson, B.D. (2004), Suspended sand concentrations in surf zones, paper presented at 29th Coastal Engineering Conference, *World Scientific*, Singapore.

Thornton, E.B., Humiston, R.T., and Birkemeier, W. (1996), Bar/trough generation on a natural beach, *J. Geophys. Res.*, 101, 12,097-12,110.

Trowbridge, J.H. (1998), On a technique for measurement of turbulent shear stress in the presence of surface waves, *J. Atmos. Oceanic Technol.*, 15, 290-298.

Trowbridge, J.H. and Young D. (1989), Sand transport by unbroken water waves under sheet flow conditions, *J. Geophys. Res.*, 94, 10,971-10,991.

6 ACKNOWLEDGEMENTS

This study was supported by the NOAA Office of Sea Grant, Department of Commerce, under Grant No. NA85AA-D-SG033 (Project SG R/OE-33) and by the National Science Foundation under Grant OCE-9901471.